The Role of Vortices in the Formation of the Solar System

by

Anand Vivek Mehta

S.B., Massachusetts Institute of Technology (1988)

Submitted to the Department of Physics
in partial fulfillment of the requirements for the degree of

Doctor of Philosophy

at the

MASSACHUSETTS INSTITUTE OF TECHNOLOGY

September 1998

Author ....
Department of Physics
August 14, 1998

Certified by ....
Glenn R. Flierl
Professor of Physical Oceanography
Thesis Supervisor

Certified by ....
Edmund W. Bertschinger
Professor of Physics
Thesis Co-Supervisor

Accepted by ....
Thomas J. Greytak
Associate Department Head for Education

The Role of Vortices in the Formation of the Solar System

by

Anand Vivek Mehta

Submitted to the Department of Physics
on August 14, 1998, in partial fulfillment of the
requirements for the degree of
Doctor of Philosophy

Abstract

An important part of explaining planet formation is understanding how small particles accumulate into larger bodies. Gas vortices are suggested as a mechanism to enhance the coagulation of dust particles in the solar nebula. An inviscid, barotropic, two-dimensional form of the vorticity equation is derived to study the gas flow. A pseudospectral numerical model uses this equation to calculate the evolution of the vorticity field. The calculations show that locally prograde elliptical vortices with the major axis parallel to the angular axis can persist for at least 10^3 years with less than 1% change in peak vorticity.

The shape of the vortex depends on the strength, similar to analytical expressions for elliptical vortices in a linear shear. Stronger vortices are rounder while weaker vortices are elongated; With ratios of the peak vorticity to the background vorticity of 1.0 and 0.2, the aspect ratios are approximately 0.5 and 0.25. The vortex area is mostly constant, and the linear dimensions change as the shape changes. Two negative vortices within the same radial band tend to merge, forming a larger, stronger vortex in a few orbit periods. A random viscosity field tends to have a few strong vortices form, although not as efficiently as with merging vortices.

Dust particles interact with the gas through the Stokes drag force, with the relaxation time specifying how quickly the particle velocity approaches the gas velocity. The particles tend to converge in high pressure vortices and drift out of low pressure systems. The convergence time is dependent on the vortex strength and the particle relaxation time. If the relaxation time is short compared to the period, the particles do not have an appreciable differential velocity compared to the gas, and the Stokes drag force is small. If the relaxation time is long, then the Stokes drag force is not large enough to have a significant effect. If, however, the relaxation time is of the same order as the period, so the dynamical and frictional timescales are similar, then the particles will have the shortest convergence times. This result can be seen analytically in the simple case of an axisymmetric pressure band and numerically in calculations involving the robust vortex. With a robust vortex, the convergence times are approximately 3–4 yr for relaxation times of 0.1–0.2 yr. For typical values of properties of the solar nebula, this relaxation time applies for particles with diameters of around 20 cm. Other particles, both smaller and larger, converge more slowly, but the different times result in more collisions, enhancing the coagulation of larger bodies.

Thesis Supervisor: Glenn R. Flierl
Title: Professor of Physical Oceanography

Thesis Co-Supervisor: Edmund W. Bertschinger
Title: Professor of Physics

Acknowledgments

I would like to thank my family, friends, and teachers, who have influenced and supported me during my time as a graduate student. While I cannot list the many people I have gotten to know, I am definitely appreciative of their friendship.

A few people must be mentioned specifically. Dora Paolucci has been extremely encouraging, helping me finish even as she was finishing her own thesis. Prof. Wisdom taught me the importance of being thorough in research, not cutting corners, or at least knowing which are being cut.

Prof. Glenn Flierl took a chance on me, supporting me in a project unrelated to most of the work he had previously done. He gave me valuable guidance which was crucial to the success of this work, given its interdisciplinary nature. His insight into a wide range of problems is amazing, as any student who has interacted with him knows. I feel very fortunate to have had Prof. Flierl as an advisor.

Contents

List of Figures

List of Tables

Chapter 1

Standard Model of Solar System Formation

Since its inception, physics has sought to understand how solar systems form. Observational information contributing to this comes primarily from our present-day solar system. Until recently, there was very little observational evidence of the existence of other solar systems, although recent observations of young stars have revealed evidence of planets. All of this information, combined with physically realistic processes, is used to develop models for solar system formation. While there is considerable uncertainty about the dynamics and details of the processes, there is widespread agreement on much of what the models include, resulting in a "standard model" for solar system formation. As more information becomes available, both observational and computational, the models can be refined.

Since the information and models are changing rapidly, the best source of general information on solar system formation is from review articles which are presented at dedicated conferences and published with the conference proceedings. These include the *Protostars & Planets III* (1993) [21] and *From Stardust to Planetesimals* (1996) [31]. The next such conference, *Protostars & Planets IV* (1998), should have the associated book available in 1999.

One of the parts of the standard model which is not well understood is how small dust particles, of sizes between $1\,\mu\text{m}$ and $1\,\text{cm}$, aggregate into larger particles, of sizes between $1\,\text{m}$ and $1\,\text{km}$, while suspended in the flow of gas around the sun. The solution discussed in this thesis is that dust particles are pulled into robust gas vortices, enhancing the aggregation process. In order to verify this, three questions need to be answered: ***how stable are the vortices, what are their characteristics, and how can they affect the flow and coagulation of dust?***

The remainder of this chapter covers the standard model for solar system formation, as well as the relevant notation to be used. Chapter 2 discusses the physical quantities relevant for particles suspended in the gas flow. Chapter 3 develops equations for the gas flow, which are then integrated numerically, as discussed in Chapter 4. In Chapter 5, the equations governing the particle motions are developed, with numerical experiments presented in Chapter 6. Finally, Chapter 7 proposes further work in this field.

1.1 The Standard Model

The standard model of planet formation includes a number of steps which are distinguished by different characteristics and processes. These include

- Collapse of a molecular cloud,
- Formation of a protostar and the solar nebula,
- Settling of gas and dust into a circumstellar disk,
- Coagulation of dust into grains,
- Clumping of grains to form planetesimals,
- Accretion of planetesimals into protoplanets,
- Gas capture by the giant planets, and
- Core differentiation.

A region of a large molecular cloud undergoes gravitational collapse to begin the formation of a solar system. While the mechanisms initiating and controlling collapse are not entirely understood, there is significant observational evidence indicating that this does happen [39]. As the region collapses, a portion forms a central protostar, which has most of the mass of the eventual star but has not yet begun nuclear fusion.

Around the protostar, a cloud of gas and dust is the precursor of the solar nebula. The nebula is originally spherical, but rotates about an axis defined as the vertical axis of the solar system. As the central star collects mass, the solar nebula forms a circumstellar disk due to the vertical component of the star's gravity, while conservation of angular momentum prevents a radial inflow. The disk lies in the plane perpendicular to the rotation axis. The settling continues until the vertical component of gravity is balanced by gas pressure. The hydrostatic equilibrium equation can be used to calculate the scale height of the nebula as a function of radius.

As the nebula settles into a disk, the dust particles settle into a flatter disk than the gas, since they are not supported by gas pressure. The characteristics of the particle disk will primarily be governed by the interaction with the gas due to the Stokes drag force and by particle-particle collisions. These particles, as found in the galactic interstellar medium and the molecular clouds, have typical sizes in the range of microns to centimeters [5].

The particles must form larger objects, of order one meter in size, which then form planetesimals with 1–100 km diameters. This inference is based on the existence of planets, asteriods, and comets, and thermal evidence of how they may have formed [44]. The two steps are separated because the interaction between the dust and the gas changes. Particles smaller than about 1 cm are coupled to the gas, and react quickly to gas flow perturbations through the Stokes drag force. For larger particles, the timescale of the drag interaction is longer than the dynamical timescale, so the particles are uncoupled from the gas. Both sizes of particles aggregate into larger bodies through collisions, which result in sticking. Fragmentation also occurs during some collisions, and different collisional models address these issues [7].

The planetesimals reach asteroid or comet sizes: 1-100 km. In dynamically favorable regimes, they may aggregate into protoplanets, approaching planetary masses for the terrestrial planets and the rocky cores of the giant planets. For sufficiently large masses, gas accretion may take place, resulting in the accumulation of most of the mass of the giant planets. At some point after the gas accretion, a T-Tauri wind dissipates much of the gaseous material around the star. This provides a significant constraint on the timescale for the total formation process. Observations of pre-main sequence stars shows that this tends to happen in approximately 1–10 Myr after the star forms, providing an upper limit to the time allowed for planet formation. It is likely that the earliest planets, such as Jupiter, formed more quickly, in about 10^5 yr, and then influenced the formation of the other planets [41].

Finally, for sufficiently large objects, over 100 km, core differentiation takes place where the interior of the body reprocesses and settles, resulting in the solar system bodies mostly as we see them today.

1.2 The Particle Aggregation Step

There has been considerable discussion about how dust particles aggregate into the rocky bodies which decouple from the gas. Early studies developed models of gravitational instabilities which resulted in increases in particle number densities [16]. Subsequent work showed that the turbulence in the nebula disk would inhibit the gravitational collapse [43, 44].

A solution to this problem might be that vortices, which are an integral part of turbulent flows, can enhance the process by which dust coagulates into grains and larger bodies.

The existence of vortices in the solar nebula has been a topic of discussion for decades. Analytical, linearized calculations on the disk implied that vortices were not likely to have formed [33]. Recent studies, however, have indicated that vortices may in fact have formed, supported by evidence in other astronomical contexts such as Jupiter's Great Red Spot [23]. Recent work by Adams and Watkins [1] examined the existence of point vorticies in the solar nebula, but left the question of larger vortices open.

The aggregation of dust particles has also been discussed for several decades, with early work done by Safronov [34] and Goldreich and Ward [16]. These studies assumed a steady dust disk with sufficient mass that self-gravity led to instabilities resulting in particle clumps. The likely gas turbulence, however, may have prevented the dust self-gravity instability from being relevent [42]. Another mechanism was necessary, and since turbulence was inhibiting the gravitational instability, it may have provided an alternative, in the form of vortices. Work supporting this hypothesis includes Barge and Sommeria [2] who examined the trajectories of particles within a simple circular vortex.

1.3 Explanation of Notation

The physical quantities which are important in this thesis are shown in Table 1.1. The relevant physical constants are listed in Table 1.2.

Vector quantities are indicated in boldface. The subscripts x, y, t indicate differentiation,

$$f_x \equiv \frac{df}{dx}.$$

Other subscripts are used to distinguish between different quantities, so v_k is the Keplerian velocity and g_r is the gravitational acceleration in the radial direction.

The units used are either CGS units or solar units, with mass, length, and time in units of the solar mass ($\mathrm{M}_\odot$), astronomical unit (AU), and the year (yr). The time may alternatively be defined using

$$\tau_0 \equiv \frac{1}{2\pi}\,\mathrm{yr}, \tag{1.1}$$

so that the velocity and angular velocity of the Keplerian disk are normalized to unity at the Earth's radius. The value of the gravitational coefficient,

$$k_k \equiv \sqrt{GM_\odot}, \tag{1.2}$$

Table 1.1: Variables

variables	dimension	description
m	[g]	mass
Σ	[g cm^{-2}]	surface density
ρ	[g cm^{-3}]	density
n	[cm^{-3}]	number density
$\boldsymbol{v}$	[cm s^{-1}]	velocity
Ω	[s^{-1}]	angular velocity
q	[s^{-1}]	vorticity
ψ	[cm^2 s^{-1}]	streamfunction
$\boldsymbol{g}$	[cm s^{-2}]	gravitational acceleration
Φ	[cm^2 s^{-2}]	gravitational potential
T	[K]	temperature
p	[g cm^{-1} s^{-2}]	pressure
c_s	[cm s^{-1}]	sound speed
λ	[cm]	mean free path
η	[g cm s^{-1}]	molecular viscosity
ν	[cm^{-2} s^{-1}]	kinematic viscosity
Δ_g, Δ_d	[cm]	particle size (gas, dust)

Table 1.2: Physical Constants

Description	Constant	Value
astronomical unit (AU)	$r_\oplus$	1.50×10^{13} cm
year	$\tau_\oplus$	3.16×10^{7} s
gravitational constant	G	6.67×10^{-8} cm^3 g^{-1} s^{-2}
solar mass	$M_\odot$	2.00×10^{33} g
hydrogen atomic weight	m_H	1.66×10^{-24} g
hydrogren atomic size	a_B	5.29×10^{-9} cm
Boltzmann constant	k_B	1.38×10^{-16} erg K^{-1}

in the three sets of units are

$$k_k = \begin{cases} 1.15 \times 10^{13}\,\mathrm{cm}^{3/2}\,\mathrm{s}^{-1} & \mathrm{CGS} \\ 2\pi\,\mathrm{AU}^{3/2}\,\mathrm{yr}^{-1} & \tau_0 = 1\,\mathrm{yr} \\ 1\,\mathrm{AU}^{3/2}\,\mathrm{yr}^{-1} & \tau_0 = \frac{1}{2\pi}\,\mathrm{yr} \end{cases} . \tag{1.3}$$

The primary coordinate systems used are cylindrical coordinates, (r, θ, Z), and a modified version, referred to as annular coordinates, (x, y, z). Cartesian coordinates centered at the Sun are used only rarely, primarily when displaying flow fields, so the coordinates (ξ, η, ζ) are used in that case.

Chapter 2

Physical Characteristics of the Solar Nebula

A number of physical parameters which are important for various formation processes are described in this chapter. The dynamical variables describe the bulk motions of the gas and dust. These include the gas velocity, vorticity, and streamfunction, as well as the angular velocity and gravitational acceleration. The thermodynamic variables govern the microscopic and the smaller scale macroscopic characteristics of the fluid. These include temperature, pressure, density, sound speed, and viscosity.

A number of parameters need to be specified to obtain values for these variables. These include

- Bulk properties such as the mass and radial size of the disk;
- The temperature at the Earth's radius;
- Compositional properties of the gas including the mean molecular weight and the ratio of gas specific heats;
- Dust properties such as size, density, and packing density;
- Indices which give the radial power of basic variables such as the temperature and the surface density.

One advantage of starting with these variables is that they are likely to be the first values obtained from observational data of nearby forming solar systems.

2.1 Fundamental Physical Relationships

The fundamental physical relationships governing the processes in the solar nebula are either dynamical or thermodynamic. The dynamical properties fall into two categories: Gravitational properties affect the large scale motions and fluid characteristics help describe the smaller scale motions.

2.1.1 Dynamical Functions

To obtain the gravitational values, first the density functions must be determined. The density, surface density, and total disk mass are related by the pair of integrals,

$$\Sigma(r,\theta) \quad = \quad \int_{-\infty}^{\infty} \rho(r,\theta,z)dz, \tag{2.1.a}$$

$$M_D = \int_0^{r_D} r dr \int_0^{2\pi} d\theta \, \Sigma(r,\theta). \tag{2.1.b}$$

If the density is assumed to be axisymmetric, then the surface density is also axisymmetric, and the mass is

$$M_D = 2\pi \int_0^{r_D} \Sigma(r) r dr. \tag{2.2}$$

The gravitational acceleration is related to the gravitational potential and the density by the two relations,

$$\boldsymbol{g} = -\boldsymbol{\nabla}\Phi, \tag{2.3.a}$$

$$\boldsymbol{\nabla}\cdot\boldsymbol{g} = -4\pi G\rho. \tag{2.3.b}$$

Given the gravitational potential of the star, Eq. 2.3.a is used to determine the gravitational acceleration. If the density of the disk can be determined, then Gauss's Law, Eq. 2.3.b, can be used to calculate the self-gravity of the disk. This equation can also be written in an integral form. When the radial component of gravity is the dominant force on an object, the angular component of the velocity vector and the angular velocity are related by

$$g_r = -\frac{v_k^2}{r} = -\Omega_k^2 r, \tag{2.4}$$

where the Keplerian velocity and angular velocity are related by

$$v_k = \Omega_k r. \tag{2.5}$$

These values are the "background" values to which perturbations are added.

The fluid variables are the streamfunction, velocity, and vorticity, and velocity potential. The velocity is defined here as the negative curl of the streamfunction, and the vorticity is the curl of the velocity,

$$\boldsymbol{v} = -\boldsymbol{\nabla}\times\boldsymbol{\psi} - \boldsymbol{\nabla}\phi, \tag{2.6.a}$$

$$\boldsymbol{q} = \boldsymbol{\nabla}\times\boldsymbol{v} \tag{2.6.b}$$

$$= \boldsymbol{\nabla}^2\boldsymbol{\psi} - \boldsymbol{\nabla}(\boldsymbol{\nabla}\cdot\boldsymbol{\psi}). \tag{2.6.c}$$

For a two-dimensional flow in the horizontal plane, the streamfunction and vorticity have only z components, and the velocity has only planar (r, θ) components. In addition, all the fluid properties are independent of z.

The contours of the streamfunction are the streamlines, which show the path of the flow, and the vorticity is a measure of the rotation within the flow. The velocity potential, ϕ, is zero if the divergence of the velocity field is zero.

2.1.2 Thermodynamic Functions

The thermodynamic quantities describe the microscopic variables and how they relate to macroscopic quantities [25], starting with the temperature, density, and composition. For different molecular species, i, the molecular weight is $\mu_i m_H$, where m_H is the atomic weight of hydrogen. With the number fraction, f_i, the mean molecular weight of the fluid is

$$\mu \equiv \sum_i f_i \mu_i, \tag{2.7}$$

which gives the relation between the mass density and the number density,

$$n = \frac{\rho}{\mu m_H}. \tag{2.8}$$

The pressure is related to the density and temperature by the equation of state. The ideal gas law,

$$p = nk_BT = \frac{k_B}{m_H}\frac{\rho T}{\mu}, \tag{2.9}$$

is assumed since the gas has a density which is not too large (not degenerate) and the temperature is not too low (at least a few Kelvin). Using this, the sound speed is the adiabatic derivative of the pressure with respect to density,

$$c_s^2 \equiv \left(\frac{\partial p}{\partial \rho}\right)_{\text{entropy}}. \tag{2.10}$$

The derivative can be changed to a isothermal differentiation by using the ratio of the constant pressure and constant volume specific heats,

$$\gamma \equiv \frac{c_P}{c_V}, \tag{2.11.a}$$

$$c_s^2 = \gamma\left(\frac{\partial p}{\partial \rho}\right)_T = \gamma\left(\frac{k_BT}{\mu m_H}\right), \tag{2.11.b}$$

where γ is approximately 7/5 for a cool diatomic gas such as H_2 or 5/3 for a monatomic gas such as He [25].

For a gas composed of hard spheres with diameter Δ_g, the molecular viscosity is

$$\eta \approx C\frac{(m_Hk_B\mu T)^{1/2}}{\Delta_g^2}, \tag{2.12}$$

where C is a numerical constant which is approximately 1/5 [25],[18]. The kinematic viscosity, which is relevant in the Navier-Stokes equation, is defined as

$$\nu \equiv \frac{\eta}{\rho} \approx \frac{(m_Hk_B\mu T)^{1/2}}{5\rho\Delta_g^2}. \tag{2.13}$$

This is used to calculate the Reynolds number,

$$Re = \frac{LU}{\nu}, \tag{2.14}$$

where L and U are the length and velocity scales. The Reynolds number indicates the importance of the viscous forces on the fluid motion relative to the dynamical forces. If the Reynolds number is large, of order 10^5 or greater, then the fluid is considered to be inviscid over those length and velocity scales [20]. As the length and velocity scales change, however, the fluid viscosity may become relevant. This is important, as the macroscopic fluid flow in the solar nebula is inviscid but the microscopic interaction between the gas and the dust particles is based on viscous forces.

Finally, the equation of hydrostatic equilibruim,

$$\frac{\partial p}{\partial z} = -g_z\rho, \tag{2.15}$$

is appropriate when gas pressure and gravity are the primary forces in a particular direction, and the changes in the gas motions in this direction are small compared to these terms. This provides a link between the dynamics and the thermodynamics in the large scale description of the solar nebula.

2.2 Typical Values for Physical Characteristics of the Solar Nebula

By specifying a number of quantities, including the total size, total mass, surface density, temperature, and composition, the other dynamical and thermodynamic quantities for the solar nebula can be derived.

2.2.1 Specified Values

Only recently has observational data been able to provide reasonable constraints on the physical properties of circumstellar disks in the solar nebula. The evidence now suggests that approximately 50% of solar mass pre-main sequence stars have disks around them [9]. These disks have masses in the range 0.002 to $0.1\,\mathrm{M}_\odot$ and radii of approximately 100 AU. The temperature is assumed to be axisymmetric with no vertical dependence. The spectral energy distribution then gives a power law radial dependence,

$$T(r,\theta,z) \sim T(r) = T_0 \left(\frac{r}{r_\oplus}\right)^{-I_T}, \tag{2.16}$$

with the index $I_T \sim 0.5$–0.75, tending to be closer to 0.5 [4], [29]. The normalization temperature, T_0, is in the range 200–400 K.

The surface density is not determined as well as the temperature by the spectral energy distribution. If assumed to be axisymmetric, it also appears to obey a radial power law,

$$\Sigma(r,\theta) \approx \Sigma(r) = \Sigma_0 \left(\frac{r}{r_\oplus}\right)^{-I_\Sigma}, \tag{2.17}$$

which can be normalized by integrating over the whole disk to get the total mass. The index is expected to have a value around 1.0, but the observations of at least one disk fit an index of $I_\Sigma \sim 0.0$–0.5 [29]. This is a significantly larger range than the temperature index for the same disk, which has a range $I_T \sim 0.45$–0.48.

The disk is predominantly H_2 and He gas, with a dust component. If the solar abundances of the helium are assumed, with a relative number abundance of 6%, the mean molecular weight is approximately $\mu = 2.1$ [12, p. 45]. If the gas in the disk and nebula is assumed to be homogeneous, then

$$\mu(r,\theta,z) \approx \mu_0 \approx 2.1. \tag{2.18}$$

With the gas being predominantly hydrogen, the size of the H_2 molecules is

$$\Delta_g \approx 2a_B \approx 10^{-8}\,\mathrm{cm}, \tag{2.19}$$

which is used to calculate the viscosity. The numbers which need to be specified are listed in Table 2.1.

2.2.2 Derived Values

It is useful to define a length coordinate which is scaled to the solar nebula,

$$a \equiv \frac{r}{r_\oplus}. \tag{2.20}$$

Table 2.1: Disk Parameters

parameter	dimension	description	approximate value
M_D	[g]	disk mass	$0.03\,\mathrm{M}_\odot$
r_D	[cm]	disk size	$50\,\mathrm{AU}$
T_0	[K]	temperature ($r = r_\oplus$)	$300\,\mathrm{K}$
μ_0	[–]	molecular mass	2
Δ_g	[cm]	particle size	$10^{-8}\,\mathrm{cm}$
I_T	[–]	temperature radial index	0.5
I_Σ	[–]	surface density radial index	1.0

Table 2.2: Derived Disk Properties

description	property	approximate value
surface density	Σ_0	$8 \times 10^2\,\mathrm{g\,cm^{-2}}$
scale height	h_0	5×10^{-2}
planar density	ρ_{c0}	$6 \times 10^{-10}\,\mathrm{g\,cm^{-3}}$
planar pressure	p_{c0}	$7 \times 10^0\,\mathrm{g\,cm^{-1}\,s^{-2}}$
sound speed	c_s	$1 \times 10^5\,\mathrm{cm\,s^{-1}}$
molecular viscosity	η_0	$7 \times 10^{-6}\,\mathrm{g\,cm^{-1}\,s^{-1}}$
kinematic viscosity	ν_0	$9 \times 10^{11}\,\mathrm{cm^2\,s^{-1}}$
Reynolds number	Re_{c0}	5×10^7

Factors of $r_\oplus$ are retained to permit calculations in CGS units.

The functional form of the surface density, Eq. 2.17, can be integrated using Eq. 2.2 to find the total mass of the disk,

$$M_D = \frac{2\pi r_\oplus^2 \Sigma_0}{2 - I_\Sigma} a_D^{2-I_\Sigma}, \tag{2.21}$$

with $I_\Sigma < 2$. Inverting this result gives an expression for the surface density at $r = 1\,\mathrm{AU}$ as a function of the disk size, mass, and the surface density radial index,

$$\begin{aligned} \Sigma_0 &= \left(\frac{M_\odot}{2\pi r_\oplus^2}\right)(2 - I_\Sigma)\; m_D \; a_D^{-2+I_\Sigma} && \text{(2.22.a)} \\ &= \left(1.4 \times 10^6\,\mathrm{g\,cm^{-2}}\right)(2 - I_\Sigma)\; m_D \; a_D^{-(2-I_\Sigma)} && \text{(2.22.b)} \\ &\approx 8 \times 10^2\,\mathrm{g\,cm^{-2}}, && \text{(2.22.c)} \end{aligned}$$

using the values for the physical properities in Table 2.1. These and other derived numbers are summarized in Table 2.2.

The gravitational force from both the central star and the disk affect the dynamics of the solar nebula. The gravitational potential of the star is

$$\Phi_* = -\frac{GM_\odot}{r}\left(1 + \frac{z^2}{r^2}\right)^{-1/2}, \tag{2.23}$$

and Eq. 2.3.a gives the gravitational acceleration,

$$g_* = -\boldsymbol{r}\,\frac{GM_\odot}{r^3}\left(1+\frac{z^2}{r^2}\right)^{-3/2}, \tag{2.24}$$

where r is the horizontal distance from the z-axis and $\boldsymbol{r}$ is the vector position. The self-gravity of the disk can be estimated by using Gauss's Law, Eq. 2.3.b. To get a rough estimate which can be compared with the star's gravity, assume that the disk is an thin, infinite, uniform density sheet of thickness $2H$. The gravitational acceleration only has a vertical component directed toward the center of the sheet. In cylindrical coordinates, Eq. 2.3.b is

$$\frac{1}{r}\frac{\partial(r g_{D,r})}{\partial r} + \frac{1}{r}\frac{\partial g_{D,\theta}}{\partial \theta} + \frac{\partial g_{D,z}}{\partial z} = -4\pi G\rho, \tag{2.25}$$

and integrating the vertical component gives

$$g_{D,z}(z) = -4\pi G\Sigma\frac{z}{2H}. \tag{2.26}$$

Comparing this with the vertical component of the star's gravity, with the approximation that $z^2/r^2 \ll 1$,

$$\frac{g_{D,z}}{g_{*,z}} = \frac{4\pi r^3\Sigma}{M_\odot 2H}. \tag{2.27}$$

Using Eq. 2.22.a, this gives

$$\frac{g_{D,z}}{g_{*,z}} \approx \left(\frac{a}{a_D}\right)^{2-I_\Sigma}\left(\frac{r_\oplus a}{2H}\right) m_D\, a^{I_\Sigma}. \tag{2.28}$$

For the values expected with the nebula, this ratio is small, so the disk gravity is relatively unimportant for the dynamics.

The Keplerian angular velocity and the tangential velocity due to the star's gravity are

$$\Omega_k = \sqrt{GM_\odot}\, r^{-3/2}\left(1+\frac{z^2}{r^2}\right)^{-3/4}, \tag{2.29.a}$$

$$v_k = \sqrt{GM_\odot}\, r^{-1/2}\left(1+\frac{z^2}{r^2}\right)^{-3/4}. \tag{2.29.b}$$

With

$$\Omega_{ko} = \frac{\sqrt{GM_\odot}}{r_\oplus^{3/2}} = \frac{2\pi}{\tau_\oplus}, \tag{2.30}$$

the planar angular velocity and tangential velocity ($z = 0$) are

$$\Omega_k = \Omega_{ko} a^{-3/2}, \tag{2.31.a}$$

$$v_k = \Omega_{ko} r_\oplus a^{-1/2}. \tag{2.31.b}$$

The streamfunction and vorticity are

$$\psi = 2\Omega_{ko} r_\oplus^{3/2} r^{1/2} = 2\Omega_{ko} r_\oplus^{2} a^{1/2}, \tag{2.32.a}$$

$$q = \frac{3}{2}\Omega_{ko} a^{-3/2}. \tag{2.32.b}$$

Next, the thermodynamic properties will be evaluated. To get the density using Eq. 2.1.a, the vertical form of the density needs to be specified. With the assumption that there is no vertical flow, hydrostatic equilibrium gives

$$\begin{aligned} \frac{\partial p}{\partial z} &= -g_z \rho && (2.33.a) \\ &= \frac{\partial \Phi}{\partial z} \rho. && (2.33.b) \end{aligned}$$

Using the ideal gas law, Eq. 2.9, for the pressure,

$$\frac{\partial p}{\partial z} = \frac{k_B T}{\mu m_H} \frac{\partial \rho}{\partial z}, \tag{2.34}$$

if $\partial T / \partial z = 0$. This gives

$$\frac{\partial \ln \rho}{\partial z} = \frac{1}{\rho} \frac{\partial \rho}{\partial z} = \frac{m_H \mu}{k_B T} \frac{\partial \Phi}{\partial z}. \tag{2.35}$$

Integrating gives

$$\begin{aligned} \ln \left(\frac{\rho}{\rho_c} \right) &= \frac{G M_\odot m_H \mu}{k_B T} \left(r^2 + z^2 \right)^{-1/2} \Big|_0^z && (2.36.a) \\ &= \left(\frac{G M_\odot m_H \mu}{k_B T} \right) \left(\frac{1}{r} \right) \left[\left(1 + \frac{z^2}{r^2} \right)^{-1/2} - 1 \right] && (2.36.b) \\ &\approx -\left(\frac{G M_\odot m_H \mu}{2 k_B T_0 r_\oplus} \right) \left(\frac{T_0}{T} \right) \left(\frac{r_\oplus}{r} \right)^3 \frac{z^2}{r_\oplus^2}. && (2.36.c) \end{aligned}$$

Solving for $\rho(z)$,

$$\begin{aligned} \rho(r, z) &= \rho_c(r) e^{-z^2/H^2}, && (2.37.a) \\ H(r) &= \left(\frac{2 k_B}{G M_\odot m_H} \frac{T r^3}{\mu} \right)^{1/2}, && (2.37.b) \end{aligned}$$

where $H(r)$ is the scale height. Then using Eq. 2.16 for the temperature, the scale height can be simplified with

$$\begin{aligned} h_0 &= \left(\frac{2 k_B r_\oplus}{G M_\odot m_H} \frac{T_0}{\mu_0} \right)^{1/2}, && (2.38.a) \\ I_H &= \tfrac{1}{2}(3 + I_T) \sim \frac{5}{4}, && (2.38.b) \end{aligned}$$

giving

$$H(a) = r_\oplus h_0 a^{I_H}. \tag{2.39}$$

The aspect ratio of the disk is

$$\begin{aligned} \epsilon(a) &= \frac{H(a)}{r} && (2.40.a) \\ &= h_0 a^{(1+I_T)/2}. && (2.40.b) \end{aligned}$$

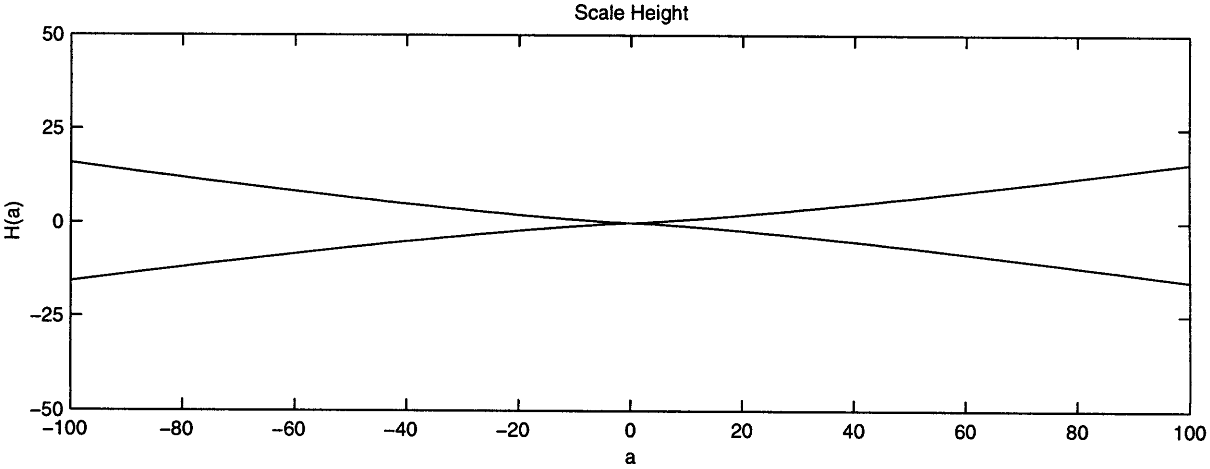

Figure 2-1: Disk scale height

Integrating the density using Eq. 2.1.a gives

$$\Sigma(r) = \sqrt{\pi}\ \rho_c(r)\ H(r). \tag{2.41}$$

Combining this with Eq. 2.17 to solve for $\rho_c(r)$,

$$\rho_c(r) \;=\; \frac{1}{\sqrt{\pi} r_\oplus}\frac{\Sigma_0}{h_0}a^{I_\rho}, \tag{2.42.a}$$

$$I_\rho \;=\; I_\Sigma - \tfrac{1}{2}I_T - \tfrac{3}{2} \sim -\frac{9}{4}. \tag{2.42.b}$$

The number density is

$$n_c(r) = \frac{\rho_c(r)}{\mu_0 m_H}. \tag{2.43}$$

The pressure in the disk is

$$p(r,z) = \frac{k_B T}{m_H \mu_0}\rho_c(r)e^{-z^2/H^2}. \tag{2.44}$$

Substituting for T, ρ_c, and h_0,

$$p(r,z) \;=\; \left(\frac{GM_\odot k_B}{2\pi r_\oplus^3 m_H}\frac{T_0\Sigma_0^2}{\mu_0}\right)^{1/2} a^{I_P}\ e^{-z^2/H^2}, \tag{2.45.a}$$

$$I_P \;=\; \tfrac{1}{2}(2I_\Sigma + I_T - 3) \sim -\frac{11}{4}. \tag{2.45.b}$$

The sound speed, mean free path, molecular viscosity, and kinematic viscosity are

$$c_s^2 \;=\; \gamma\left(\frac{k_B T}{m_H \mu_0}\right) = \left(\frac{\gamma k_B T_0}{m_H \mu_0}\right)\ a^{I_T}, \tag{2.46.a}$$

$$\lambda \;=\; \frac{\sqrt{\pi}\ m_H r_\oplus\ \mu_0 h_0}{5\Delta_g^2\Sigma_0}\ a^{-I_\Sigma - I_H}\ e^{-z^2/H^2}, \tag{2.46.b}$$

$$\eta = \frac{1}{4\Delta_g^2}\left(\tfrac{1}{2}m_H k_B \ \mu_0 T_0\right)^{1/2} \ a^{I_T/2}, \tag{2.46.c}$$

$$\nu = \left(\frac{\pi r_\oplus^3 k_B^2}{16GM_\odot}\right)^{1/2} \frac{T_0}{\Delta_g^2\Sigma_0} \ a^{(3/2-I_\Sigma)} \ e^{+z^2/H^2}. \tag{2.46.d}$$

2.3 Dust Characteristics

The size, density, mass, packing number, and distribution of dust particles needs to be estimated to understand how the gas affects the dust particles.

Studies of pre-solar grains shows that particle sizes appear to fall in the range of 10 nm–10 μm [5]. While the intertellar medium does not appear to have grains larger than this, some processing may have occurred as the dust settled into the circumstellar disk, although observational evidence of this is not available from our present-day solar system.

As dust particles collide a combination of aggregation and fragmentation occurs, but the conditions for selecting between these processes are not fully understood [6]. In addition, the results of the aggregation can vary, especially the particle packing density, which is the radial power of the mass,

$$m \propto r^\delta. \tag{2.47}$$

Solid particles have packing density $\delta = 3$, while fluffy particles tend to have values closer to $\delta \approx 2.2$ [7].

For this work, the particles are assumed to be solid, with mass density of a single particle,

$$\rho_p \approx 2\,\mathrm{g\,cm^{-3}}, \tag{2.48}$$

so the mass is

$$m = \frac{1}{6}\pi\rho_p\Delta_d^3, \tag{2.49}$$

where Δ_d is the size of a dust particle.

Chapter 3

The Gas Flow in the Solar Nebula

To enhance the accumulation of dust grains into larger bodies, a vortex in the solar nebula gas must persist for a significant fraction of the time required for planet formation. With Keplerian velocity distribution of the gas in the disk, the stability of a vortex cannot be determined analytically. Therefore, a numerical representation of the vortex is developed, and the vorticity equation is used to determine the robustness of the vortex.

The vorticity equation is derived from the fundamental conservation equations of fluid flow, the continuity equation and the Navier-Stokes equation. A rotating coordinate system is used, and the equations are non-dimensionalized to isolate the relevant parameters, such as the Reynolds number. The vorticity equation is written in annular coordinates, and the quantities related to the Keplerian flow can be separated from those due to the vortex perturbation. Applying boundary conditions to the perturbation further simplifies the vorticity equation, resulting in an equation of motion which can be numerically integrated to study the evolution of a vortex.

3.1 Fluid Equations in a Rotating Coordinate System

3.1.1 Basic Fluid Equations

Starting with the continuity equation and the Navier-Stokes equation (NSE), as described in textbooks such as Landau & Lifschitz and Batchelor ([20], [3]), the NSE can be expressed in a rotating frame. The NSE can then be non-dimensionalized, and the curl taken to give the vorticity equation.

The continuity equation, expressing conservation of mass for a flow with no sources or sinks, is

$$\frac{\partial \rho}{\partial t} + \boldsymbol{\nabla}\cdot(\rho \boldsymbol{v}) = 0. \tag{3.1}$$

The material derivative,

$$\frac{D}{Dt} f(\boldsymbol{r},t) \equiv \left(\frac{\partial}{\partial t} + \boldsymbol{v}\cdot\boldsymbol{\nabla}\right) f(\boldsymbol{r},t), \tag{3.2}$$

can be used to write the continuity equation as

$$\frac{D\rho}{Dt} + \rho \boldsymbol{\nabla}\cdot\boldsymbol{v} = 0. \tag{3.3}$$

The NSE, based on conservation of momentum, is

$$\frac{D\boldsymbol{v}}{Dt} = \frac{\partial \boldsymbol{v}}{\partial t} + (\boldsymbol{v} \cdot \boldsymbol{\nabla})\boldsymbol{v} = -\frac{1}{\rho}\boldsymbol{\nabla} p + \boldsymbol{g} + \frac{1}{\rho}\boldsymbol{F}_{\text{visc}}, \tag{3.4}$$

with the viscosity term

$$\boldsymbol{F}_{\text{visc}} \equiv \boldsymbol{\nabla}\cdot \left(\eta \left[(\boldsymbol{\nabla v}) + (\boldsymbol{\nabla v})^T - \frac{2}{3}\mathbf{I}(\boldsymbol{\nabla}\cdot\boldsymbol{v})\right]\right) + \boldsymbol{\nabla}[\zeta(\boldsymbol{\nabla}\cdot\boldsymbol{v})], \tag{3.5}$$

where **I** is the identity matrix, η is the molecular viscosity, and ζ is the bulk viscosity, which is assumed to be negligible. Since the molecular viscosity, η, depends only weakly on distance ($\eta \sim r^{-1/4}$), assuming η constant gives

$$\boldsymbol{F}_{\text{visc}} \to \boldsymbol{F}_{\eta} = \eta \left[\nabla^2 \boldsymbol{v} + \frac{1}{3}\boldsymbol{\nabla}(\boldsymbol{\nabla}\cdot\boldsymbol{v})\right]. \tag{3.6}$$

The advection term in Eq. 3.4 can be rewritten using a vector relation from § A.5, Eq. A.86, as

$$(\boldsymbol{v} \cdot \boldsymbol{\nabla})\boldsymbol{v} = \boldsymbol{\nabla}\left(\tfrac{1}{2}\boldsymbol{v}\cdot\boldsymbol{v}\right) - \boldsymbol{v} \times (\boldsymbol{\nabla}\times\boldsymbol{v}), \tag{3.7}$$

and the gravitation term can be written as the gradient of the gravitational potential,

$$\boldsymbol{g} = -\boldsymbol{\nabla}\Phi. \tag{3.8}$$

It is convenient to transform to a rotating coordinate system with a constant angular velocity, as described in §A.2.3.

$$\boldsymbol{\Omega} = \hat{\boldsymbol{z}}\Omega_c. \tag{3.9}$$

The velocity and acceleration are

$$\begin{aligned} \boldsymbol{v}' &= \boldsymbol{v} + \boldsymbol{\Omega} \times \boldsymbol{r}, && \text{(3.10.a)} \\ \frac{d\boldsymbol{v}'}{dt'} &= \frac{d\boldsymbol{v}}{dt} + 2\boldsymbol{\Omega} \times \boldsymbol{v} - \boldsymbol{\nabla}\left(\tfrac{1}{2}|\boldsymbol{\Omega} \times \boldsymbol{r}|^2\right). && \text{(3.10.b)} \end{aligned}$$

The viscosity term is unchanged by the transformation. The Navier-Stokes equation can then be written as

$$\begin{aligned} &\frac{\partial \boldsymbol{v}}{\partial t} + (2\boldsymbol{\Omega} + \boldsymbol{\nabla}\times\boldsymbol{v}) \times \boldsymbol{v} \\ &\quad = -\frac{1}{\rho}\boldsymbol{\nabla} p + \boldsymbol{\nabla}\left(\tfrac{1}{2}|\boldsymbol{\Omega} \times \boldsymbol{r}|^2 - \tfrac{1}{2}|\boldsymbol{v}|^2 - \Phi\right) + \nu\left(\nabla^2\boldsymbol{v} + \frac{1}{3}\boldsymbol{\nabla}(\boldsymbol{\nabla}\cdot\boldsymbol{v})\right), \end{aligned} \tag{3.11}$$

where $\nu \equiv \eta/\rho$ is the kinematic viscosity. The only assumptions made in deriving this equation are that the molecular viscosity is constant and the bulk viscosity is zero.

If the fluid is assumed to be incompressible, the material derivative of the density is zero, so the continuity equation requires that the velocity field be divergenceless,

$$\boldsymbol{\nabla}\cdot\boldsymbol{v} = 0. \tag{3.12}$$

3.1.2 Non-Dimensional Navier-Stokes Equation

The non-dimensional NSE can be derived by using the following units,

$$\begin{aligned} L &= r_\oplus \,[\mathrm{cm}], && (3.13.a) \\ \tau_\oplus &= k_k \sqrt{\frac{GM_\odot}{r_\oplus^3}} \,[\mathrm{s}], && (3.13.b) \\ U &= \frac{L}{\tau_\oplus} \,[\mathrm{cm\,s^{-1}}], && (3.13.c) \end{aligned}$$

so the nondimensional quantities (primed) are

$$\begin{aligned} t &\to \tau_\oplus t', && (3.14.a) \\ \frac{\partial}{\partial t} &\to \frac{1}{\tau_\oplus}\frac{\partial}{\partial t'}, && (3.14.b) \\ x &\to L x', && (3.14.c) \\ \boldsymbol{\nabla} &\to \frac{1}{L}\boldsymbol{\nabla}', && (3.14.d) \\ \boldsymbol{v} &\to U\boldsymbol{v}', && (3.14.e) \\ q &\to \frac{1}{\tau_\oplus} q'. && (3.14.f) \end{aligned}$$

The pressure term in Eq. 3.11 includes a factor of pressure divided by density. For the ideal gas, this multiplied by γ has the value of the square of the sound speed,

$$c_s^2 = \gamma \frac{p}{\rho}. \tag{3.15}$$

The Mach number, the gas speed divided by the sound speed,

$$M_s \equiv \frac{U}{c_s}, \tag{3.16}$$

is the parameter which governs the importance of the pressure term. The viscosity term in Eq. 3.11 can be non-dimensionalized by using the Reynolds number,

$$Re \equiv \frac{LU}{\nu}. \tag{3.17}$$

The non-dimensional NSE is then

$$\begin{aligned} &\frac{\partial \boldsymbol{v}}{\partial t} + (2\boldsymbol{\Omega} + \boldsymbol{\nabla}\times\boldsymbol{v}) \times \boldsymbol{v} \\ &\quad = -\frac{1}{\gamma M_s^2}\frac{1}{\rho}\boldsymbol{\nabla}p + \boldsymbol{\nabla}\left(\tfrac{1}{2}|\boldsymbol{\Omega}\times\boldsymbol{r}|^2 - \tfrac{1}{2}|\boldsymbol{v}|^2 - \Phi\right) + \frac{1}{Re}\left(\nabla^2\boldsymbol{v} + \frac{1}{3}\boldsymbol{\nabla}(\boldsymbol{\nabla}\cdot\boldsymbol{v})\right). \end{aligned} \tag{3.18}$$

This is the general, three-dimensional, non-dimensionalized Navier-Stokes equation, independent of the coordinate system.

3.1.3 The Vorticity Equation

The vorticity equation is obtained by taking the curl of the NSE, Eq. 3.18. Then, by making use of several assumptions, a conservation equation can be derived for the vorticity.

The curl of the non-dimensional NSE, Eq. 3.18, gives

$$\frac{\partial \boldsymbol{q}}{\partial t} + \boldsymbol{\nabla}\times[(2\boldsymbol{\Omega} + \boldsymbol{\nabla}\times\boldsymbol{v}) \times \boldsymbol{v}] = +\frac{1}{\gamma M_s^2}\frac{1}{\rho^2}\boldsymbol{\nabla}\rho\times\boldsymbol{\nabla}p + \frac{1}{Re}\nabla^2\boldsymbol{q}, \tag{3.19}$$

where the curl of the gradient of scalars are zero and $\boldsymbol{q} \equiv \boldsymbol{\nabla}\times\boldsymbol{v}$ is the vector vorticity. The second term on the left-hand side of Eq. 3.19 gives

$$\boldsymbol{\nabla}\times[(2\boldsymbol{\Omega} + \boldsymbol{\nabla}\times\boldsymbol{v}) \times \boldsymbol{v}] = (\boldsymbol{v}\cdot\boldsymbol{\nabla})\boldsymbol{q} - (\boldsymbol{q}\cdot\boldsymbol{\nabla})\boldsymbol{v}, \tag{3.20}$$

assuming the velocity is divergenceless. The pressure term can be eliminated if the pressure gradient is parallel to the density gradient. This would be the case, for example, if the entropy of the gas were uniform so that the density (which varies with entropy and pressure, in general) becomes a function only of pressure. For the gas flow in the solar nebula, the Reynolds number can be estimated to be of order 10^8. This implies that the viscous terms in the fluid flow equations are not significant compared to the dynamical terms, so they are also dropped from the vorticity equation. A two-dimensional flow will be assumed; this may not be completely realistic, but this simplification allows the development of a basic picture of vortex and dust dynamics in the solar nebula.

The two-dimensional approximation implies that the vertical velocity is zero and the horizontal components of the vorticity vanish. The second term on the right-hand side of Eq. 3.20, the stretching term, vanishes. The z-component of the vorticity equation then simplifies to

$$D_t q = \frac{\partial q}{\partial t} + (\boldsymbol{v} \cdot \boldsymbol{\nabla})q = 0. \tag{3.21}$$

The derivation of this equation has required the assumptions that

- the flow is incompressible, $\frac{D\rho}{Dt} = 0$,
- the flow is two dimensional, $w = 0$ and $\frac{\partial\cdot}{\partial z} = 0$,
- the fluid is barotropic, $\boldsymbol{\nabla}\rho \times \boldsymbol{\nabla}p = 0$, and
- the flow is inviscid.

Also, for two-dimensional flow, the vector streamfunction has only a vertical component,

$$\boldsymbol{\psi} = \hat{\boldsymbol{z}}\psi, \tag{3.22}$$

and the velocity and vorticity are related to ψ by

$$\begin{aligned} \boldsymbol{v} &= -\boldsymbol{\nabla}\times(\hat{\boldsymbol{z}}\psi) = \hat{\boldsymbol{z}}\times\boldsymbol{\nabla}\psi, && (3.23.a) \\ q &= \nabla^2\psi. && (3.23.b) \end{aligned}$$

3.1.4 Annular Coordinates

The standard approach to solving the vorticity equation would start by writing it in either cylindrical (r, θ, Z) or local cartesian coordinates. Since the goal here is to study a small portion of the disk, but not take a local approximation, an alternative coordinate system, "annular

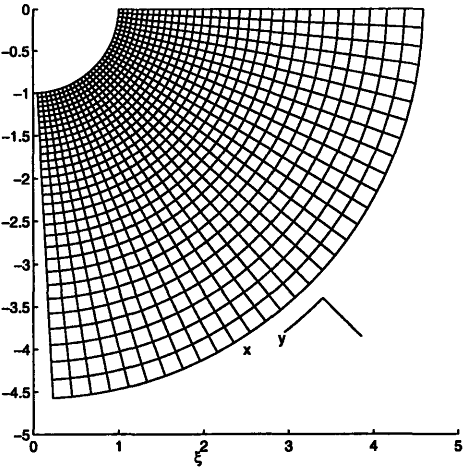

Figure 3-1: Annular coordinate grid, with $r_0 = 1.0$, $x = [0, 2\pi]$, $y = [0, 2\pi]$; (a) $M = 4$

coordinates," is used, with coordinates (x, y, z). Annular coordinates are related to cylindrical coordinates with two parameters, r_0 and M, and the coordinate transformation equations

$$\begin{array}{rclcrclcrcl} x &=& -M\theta & & r &=& r_0\, e^{y/M} & & \hat{x} &=& -\hat{\theta} \\ y &=& M \ln\left(\frac{r}{r_0}\right), & & \theta &=& -\frac{1}{M}x, & & \hat{y} &=& \hat{r} \\ z &=& Z & & Z &=& z & & \hat{z} &=& \hat{Z} \end{array} . \tag{3.24}$$

Cartesian coordinates, with the origin at the sun, are seldom used, and when they are, the coordinate labelss (ξ, η, ζ) are used. The annular coordinate grid mapped into cartesian coordinates is shown in Fig. 3-1. Further details about annular coordinates are discussed in §A.3.

3.1.5 The Background Values in the Rotating Coordinates System

The total vorticity and streamfunction in the vorticity equation can be separated into the Keplerian term and a perturbation term. The Keplerian term describes the flow of the steady disk, while the perturbation represents the quantities related to the vortices or vorticity anomalies to be studied.

The velocity of the Keplerian flow in rotating coordinates is

$$\bar{v} = \hat{\theta}\left[k_k r^{-1/2} - r\Omega_c\right] \tag{3.25.a}$$

$$= \hat{\theta} k_k \left[r^{-1/2} - r r_c^{-3/2}\right], \tag{3.25.b}$$

in cylindrical coordinates, with $k_k = 2\pi$ in units of $\mathrm{AU}^{3/2}\,\mathrm{yr}^{-1}$. The streamfunction and vorticity can be determined using Eq. 2.6, giving

$$\bar{\psi} = k_k \left[2r^{1/2} - \tfrac{1}{2}r^2 r_c^{-3/2}\right], \tag{3.26.a}$$

$$\bar{q} = k_k \left[\tfrac{1}{2}r^{-3/2} - 2r_c^{-3/2}\right]. \tag{3.26.b}$$

In annular coordinates, the velocity, streamfunction, and vorticity have the values

$$\begin{aligned}
\bar{\boldsymbol{v}} &= -\hat{\boldsymbol{x}} k_k r_0^{-1/2} \left[e^{-y/2M} - e^{y/M} e^{-3y_c/2M} \right], && \text{(3.27.a)} \\
\bar{\psi} &= k_k r_0^{1/2} \left[2e^{y/2M} - \tfrac{1}{2} e^{2y/M} e^{-3y_c/2M} \right], && \text{(3.27.b)} \\
\bar{q} &= k_k r_0^{-3/2} \left[\tfrac{1}{2} e^{-3y/2M} - 2e^{-3y_c/2M} \right]. && \text{(3.27.c)}
\end{aligned}$$

Plots of the velocity, streamfunction, and vorticity are shown in Fig. 3-2.

3.1.6 The Vorticity Equation in Annular Coordinates

The vorticity equation can be written in annular coordinates. The annular coordinate forms for the streamfunction and vorticity, as defined by Eq. 2.6, are

$$\begin{aligned}
\boldsymbol{v} &= \left(\frac{M}{r}\right)\left(-\hat{\boldsymbol{x}}\frac{\partial \psi}{\partial y} + \hat{\boldsymbol{y}}\frac{\partial \psi}{\partial x}\right), && \text{(3.28.a)} \\
q &= \left(\frac{M}{r}\right)^2 \left(\frac{\partial^2}{\partial x^2} + \frac{\partial^2}{\partial y^2}\right)\psi. && \text{(3.28.b)}
\end{aligned}$$

The second term of the vorticity equation gives

$$\begin{aligned}
(\boldsymbol{v}\cdot\boldsymbol{\nabla})q &= \left(\frac{M}{r}\right)^2 (\psi_x q_y - \psi_y q_x) && \text{(3.29.a)} \\
&= -\left(\frac{M}{r}\right)^2 J(q,\psi), && \text{(3.29.b)}
\end{aligned}$$

where the subscript notation indicates differentiation and $J(q,\psi)$ is the Jacobian determinant.

The total flow can be separated into the Keplerian flow and the vortex anomaly flow by

$$\begin{aligned}
q &= \bar{q} + q', && \text{(3.30.a)} \\
\psi &= \bar{\psi} + \psi'. && \text{(3.30.b)}
\end{aligned}$$

The derivatives are

$$\begin{array}{rclcrcl}
\psi_x &=& \psi'_x & & \psi_y &=& \bar{\psi}_y + \psi'_y \\
q_x &=& q'_x \;, & & q_y &=& \bar{q}_y + q'_y \;, \\
q_{xx} &=& q'_{xx} & & q_{yy} &=& \bar{q}_{yy} + q'_{yy}
\end{array} \qquad \text{(3.31)}$$

since the background vorticity and streamfunction are axisymmetric and therefore only depend on y. The Jacobian becomes

$$\begin{aligned}
J(q,\psi) &= q_x\psi_y - q_y\psi_x && \text{(3.32.a)} \\
&= (\bar{\psi}_y + \psi'_y)q'_x - (\bar{q}_y + q'_y)\psi'_x, && \text{(3.32.b)}
\end{aligned}$$

which is nonlinear. The conservation properties of the numerical approximation of the Jacobian are improved by expressing it as the divergence of a flux. This can be done by taking the products of q' with $\psi'_{x,y}$ and then differentiating, rather than taking the product of $q'_{x,y}$ and $\psi'_{x,y}$. This can be accomplished by adding and subtracting the term $\psi'_{xy}q'$ to the two terms of the Jacobian, giving

$$J(q,\psi) = [(\bar{\psi}_y + \psi'_y)q']_x - (\bar{q}_y\psi'_x) - (\psi'_x q')_y. \qquad \text{(3.33)}$$

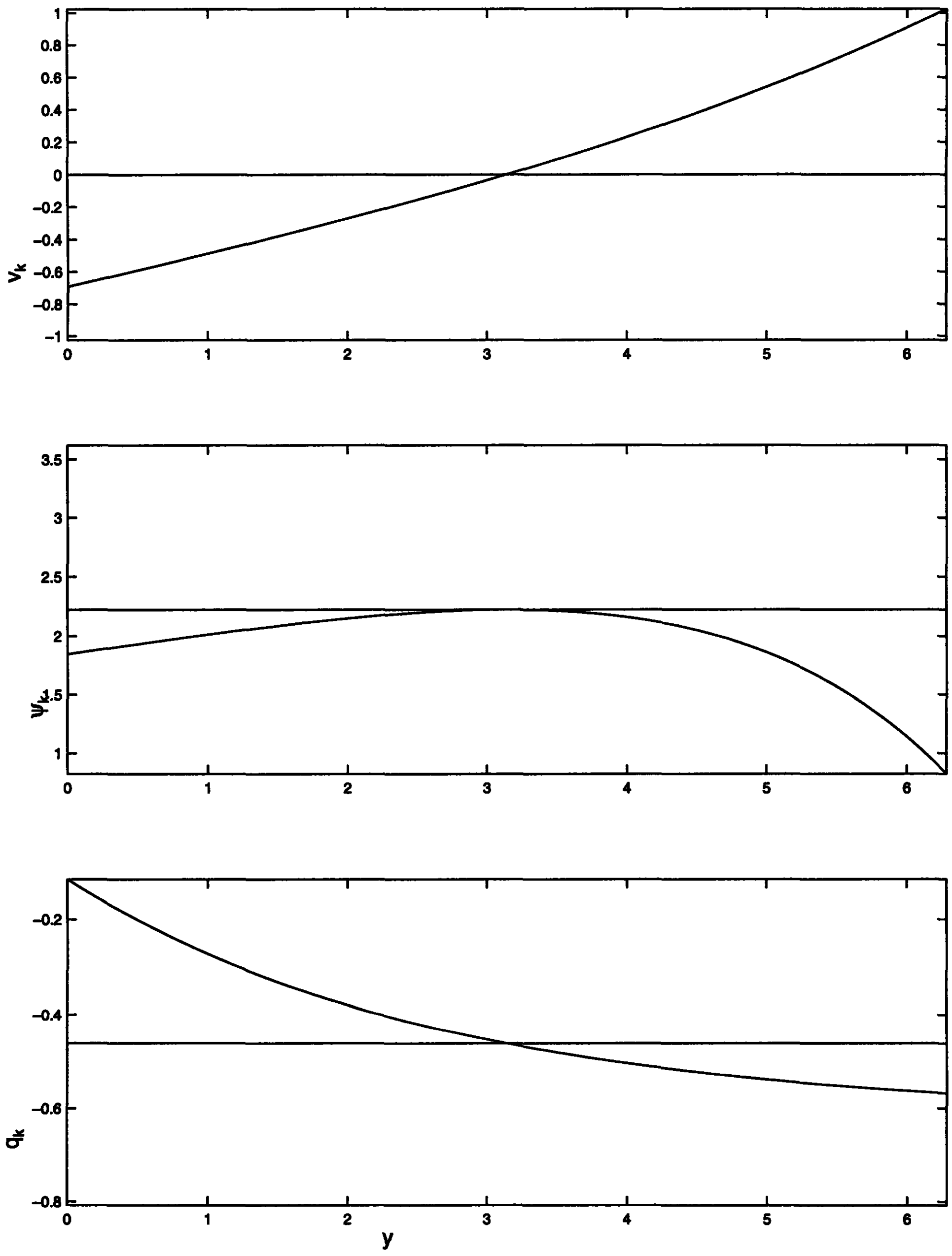

Figure 3-2: Background fluid values in rotating annular coordinates, centered on the fluid value at the center of the band; $M = 4$, $y = [0, 2\pi]$, $k_k = 1$.

This simplification also reduces the data storage requirement in the numerical model. The vorticity equation can then be written as

$$\left(\frac{r^2}{M^2}q'\right)_t = J(q,\psi) + \frac{1}{Re}(q'_{xx} + q'_{yy} + \bar{q}_{yy}). \tag{3.34}$$

3.2 Elliptical Vortex

3.2.1 Elliptical Gas Vortex in Cartesian Coordinates: Discussion

The elliptical vortex can be modelled as an elliptical region with uniform, constant vorticity inside and zero vorticity outside. This vorticity anomaly is added to the background vorticity of the rotating Keplerian flow, approximated as a linear shear flow in the Cartesian coordinate approximation, to get the total vorticity. The streamfunction then needs to be specified such that Poisson's equation is satisfied; the boundary of the patch is a streamline; and the streamfunction and the velocity are continuous across the boundary.

Inside the vortex, the streamfunctions for the vortex, background, and total flows are all related to the respective vorticity values by Poisson's equation. Since the functional forms of the background and the total streamfunction are different, a constraint is placed on the relationship between the aspect ratio of the vortex and ratio of the vortex to background vorticities. This relationship can then be used to derive the functional form of the vortex streamfunction.

The vortex streamfunction is not constant on the elliptical boundary, so the requirement that the streamfunction and the velocity be continuous across the boundary cannot simply be satisfied by adding a constant to the streamfunction outside the vortex. Since the boundary is elliptical, it is useful to solve for the matching external perturbation streamfunction in elliptical coordinates as described in §A.4. This streamfunction is physically important, as it represents the perturbation of the flow around the vortex, resulting in the deviation around the vortex in what would otherwise be a straight flow. The perturbation streamfunction must satisfy four constraints:

- the Laplacian is zero, so no vorticity is added to the flow;
- the value and gradient equal the value and gradient of the vortex streamfunction along the boundary;
- the gradient approaches zero far from the vortex; and
- the value is proportional to $\ln(r)$ far from the vortex, as for a point vortex.

Once the external perturbation streamfunction is fully specified, the derivatives of the internal and external total streamfunction give the gas velocity components. These derivatives are used in the dust particle equations of motion to calculate the particle trajectories.

3.2.2 Elliptical Gas Vortex in Cartesian Coordinates: Equations

The vorticities are constant and related by

$$q_{in} = \bar{q} + q', \tag{3.35.a}$$

$$q_{out} = \bar{q}. \tag{3.35.b}$$

The background vorticity, representing a negative, constant shear, is given by Eq. 5.30 as $\bar{q} = -\frac{3}{2}\Omega_c$. The streamfunction and velocity of the background flow are

$$\begin{aligned} \bar{v} &= -\hat{x}\bar{q}y, && (3.36.a) \\ \bar{\psi} &= \tfrac{1}{2}\bar{q}y^2, && (3.36.b) \end{aligned}$$

where the origin of the coordinate frame is located at the center of the vortex, so $y_c = 0$.

The total streamfunction inside the vortex is

$$\psi_{in} = \bar{\psi} + \psi'. \tag{3.37}$$

A streamfunction solution which satisfies Poisson's equation,

$$q = \nabla^2\psi, \tag{3.38}$$

the boundary condition,

$$\psi_{in}|_E = \text{const}, \tag{3.39}$$

and the elliptical boundary condition specified by Eq. A.73, is

$$\psi_{in} = \tfrac{1}{2}(\bar{q} + q')\left(\frac{\lambda}{1+\lambda^2}\right)\left[\lambda x^2 + \frac{1}{\lambda}y^2 - s^2\right]. \tag{3.40}$$

The vortex streamfunction, which must also satisfy Poisson's equation, but not the boundary condition, has the form

$$\psi' = \tfrac{1}{2}q'\left(\frac{1}{a+b}\right)\left[ax^2 + by^2 - s^2\right]. \tag{3.41}$$

By combining the x^2, y^2, and s^2 terms of the three streamfunction equations, the vortex streamfunction has a solution of $a = \lambda$ and $b = 1$, with the relationship

$$Q \equiv \frac{q'}{\bar{q}} = \lambda\left(\frac{1+\lambda}{1-\lambda}\right). \tag{3.42}$$

This shows that an aspect ratio of unity is not possible, but the circular vortex can only be approached if the vortex vorticity is much stronger than the background. If the vortex is weaker than the background, then the aspect ratio will be small, and the vortex will be stretched. Equation 3.42 has the limit that the aspect ratio approaches the ratio of the vorticities when both are small. Since the aspect ratio actually depends on the vortex strength, instead of the other way around, it is useful to invert Eq. 3.42, giving

$$\lambda = -\tfrac{1}{2}(1+Q) + \sqrt{\tfrac{1}{4}(1+Q)^2 + Q}, \tag{3.43}$$

where the positive root of the quadratic equation is taken since the aspect ratio cannot be negative. The relationship between the vortex strength and the aspect ratio is shown in Fig. 3-3.

Defining the parameter,

$$A = \frac{1}{2}\frac{1}{1+\lambda}q', \tag{3.44}$$

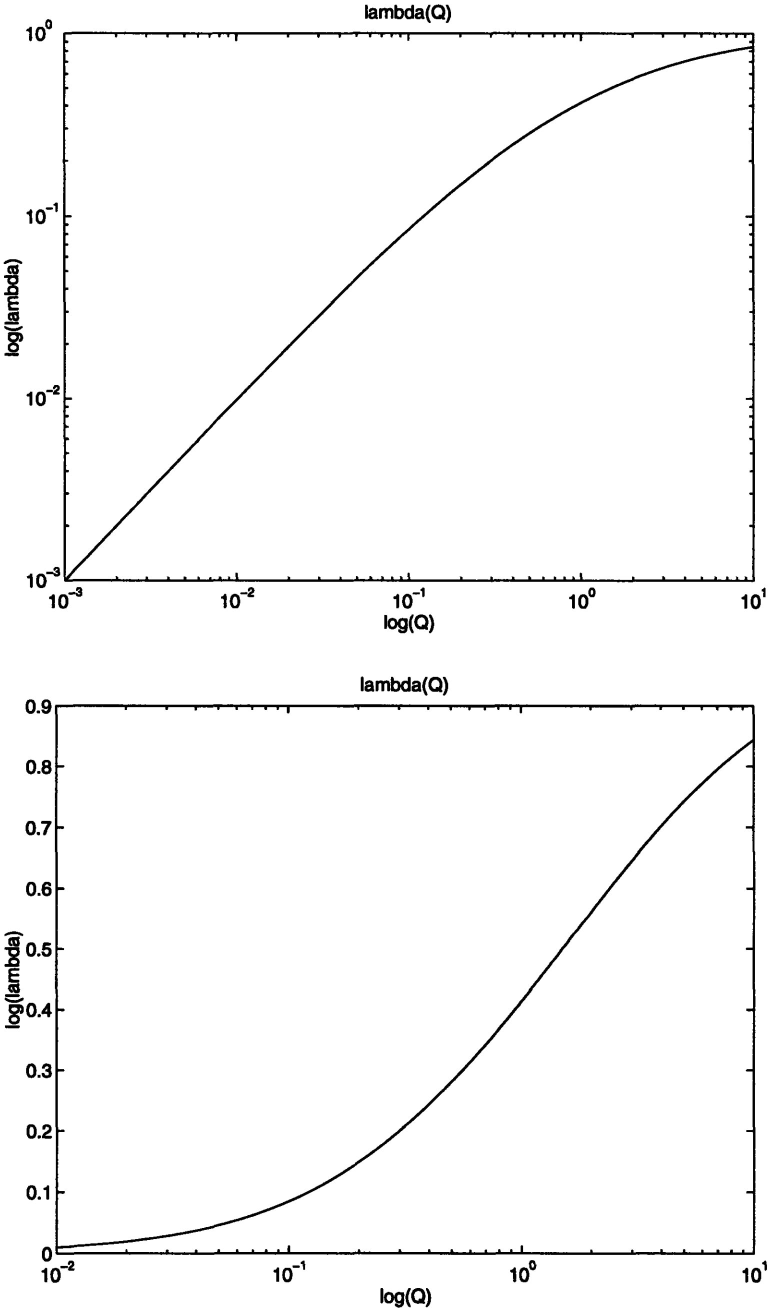

Figure 3-3: Aspect ratio as a function of vortex strength

the vortex, background, and total internal streamfunction are

$$\psi' = A\left[\lambda x^2 + y^2 - s^2\right], \tag{3.45.a}$$

$$\bar{\psi} = A\left(\frac{1-\lambda}{\lambda}\right) y^2, \tag{3.45.b}$$

$$\psi_{in} = A\left[\lambda x^2 + \frac{1}{\lambda} y^2 - s^2\right]. \tag{3.45.c}$$

Using elliptical coordinates, the background and vortex streamfunction are

$$\bar{\psi} = A\left(\frac{1-\lambda}{\lambda}\right) c^2 \sinh^2\mu \sin^2\phi, \tag{3.46.a}$$

$$\psi' = Ac^2\left[\lambda \cosh^2\mu \cos^2\phi + \sinh^2\mu \sin^2\phi - \frac{s^2}{c^2}\right]. \tag{3.46.b}$$

The streamfunction outside the vortex is

$$\psi_{out} = \bar{\psi} + \tilde{\psi}, \tag{3.47}$$

where $\tilde{\psi}$ is the external perturbation streamfunction. With the constraints

$$\nabla^2 \tilde{\psi} = 0, \tag{3.48.a}$$

$$\tilde{\psi}|_E = \psi'|_E, \tag{3.48.b}$$

$$\boldsymbol{\nabla}\tilde{\psi}|_E = \boldsymbol{\nabla}\psi'|_E, \tag{3.48.c}$$

$$\lim_{r\to\infty} \tilde{\psi} \propto \ln(r), \tag{3.48.d}$$

$$\lim_{r\to\infty} \boldsymbol{\nabla}\tilde{\psi} = 0, \tag{3.48.e}$$

a solution to Laplace's equation,

$$\nabla^2 \tilde{\psi} = 0, \tag{3.49}$$

is

$$\tilde{\psi} = As^2\left[(1+\lambda)(\mu-\mu_0) + \tfrac{1}{2}(1-\lambda)\left(e^{-2(\mu-\mu_0)}\cos 2\phi - 1\right)\right]. \tag{3.50}$$

In elliptical coordinates, Eq. 3.49 is

$$\left(\frac{\partial^2}{\partial\mu^2} + \frac{\partial^2}{\partial\phi^2}\right)\tilde{\psi} = 0, \tag{3.51}$$

which is satisfied by Eq. 3.50. To check the value and gradient of $\tilde{\psi}$ on the boundary use

$$a = c\,\cosh\mu_0, \tag{3.52.a}$$

$$b = c\,\sinh\mu_0, \tag{3.52.b}$$

$$s^2 = ab = \lambda a^2 = \frac{1}{\lambda} b^2, \tag{3.52.c}$$

as described in §A.4. The values of both the perturbation and the vortex streamfunction are zero, satisfying the second constraint. The elliptical derivatives for the vortex streamfunction are

$$\psi'_\mu = 2Ac^2 \sinh\mu \cosh\mu \left[\lambda + (1-\lambda)\sin^2\phi\right], \tag{3.53.a}$$

$$\psi'_\phi = 2Ac^2 \sin\phi\cos\phi \left[\sinh^2\mu - \lambda\cosh^2\mu\right], \tag{3.53.b}$$

for the background streamfunction,

$$\bar{\psi}_\mu = 2A\left(\frac{1-\lambda}{\lambda}\right)c^2 \sinh\mu \cosh\mu \ \sin^2\phi, \tag{3.54.a}$$

$$\bar{\psi}_\phi = 2A\left(\frac{1-\lambda}{\lambda}\right)c^2 \sinh^2\mu \ \sin\phi\cos\phi, \tag{3.54.b}$$

and for the external perturbation streamfunction,

$$\tilde{\psi}_\mu = As^2\left[(1+\lambda) - (1-\lambda)e^{-2(\mu-\mu_0)}\cos 2\phi\right], \tag{3.55.a}$$

$$\tilde{\psi}_\phi = As^2\left[-(1-\lambda)e^{-2(\mu-\mu_0)}\sin 2\phi\right]. \tag{3.55.b}$$

The derivatives of the total internal and external streamfunctions on the elliptical boundary are equal, satisfying the third constraint. The angular derivatives are zero, which confirms that the boundary is a streamline. The μ derivatives are non-zero on the boundary, so the boundary is not an extremum of the streamlines. The velocity components are related to the streamfunction by

$$u = -\psi_y = \begin{cases} -(\psi_{in})_y & \text{inside the vortex} \\ -(\bar{\psi})_y - (\tilde{\psi})_y & \text{outside the vortex} \end{cases}, \tag{3.56.a}$$

$$v = +\psi_x = \begin{cases} +(\psi_{in})_x & \text{inside the vortex} \\ +(\bar{\psi})_x + (\tilde{\psi})_x & \text{outside the vortex} \end{cases}. \tag{3.56.b}$$

The Cartesian derivatives of the total internal streamfunction are

$$(\psi_{in})_x = 2A\lambda x, \tag{3.57.a}$$

$$(\psi_{in})_y = 2A\frac{1}{\lambda}y, \tag{3.57.b}$$

and of the background streamfunction are

$$(\bar{\psi})_x = 0, \tag{3.58.a}$$

$$(\bar{\psi})_y = 2A\left(\frac{1-\lambda}{\lambda}\right)y. \tag{3.58.b}$$

To calculate the derivatives of the external perturbation streamfunction, use Eq. A.84 to get

$$(\tilde{\psi})_x = \frac{\tilde{\psi}_\mu d_1 - \tilde{\psi}_\phi d_2}{d_1^2 + d_2^2}, \tag{3.59.a}$$

$$(\tilde{\psi})_y = \frac{\tilde{\psi}_\mu d_2 + \tilde{\psi}_\phi d_1}{d_1^2 + d_2^2}, \tag{3.59.b}$$

with

$$d_1 = c \ \sinh\mu \ \cos\phi, \tag{3.60.a}$$

$$d_2 = c \ \cosh\mu \ \sin\phi, \tag{3.60.b}$$

and the elliptical derivatives of the streamfunction given by Eq. 3.55.

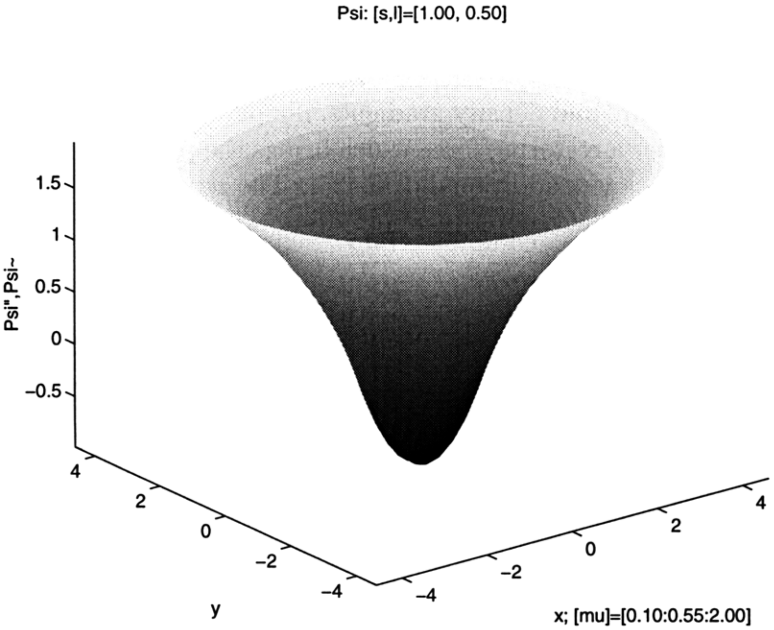

Figure 3-4: Elliptical vortex total streamfunction

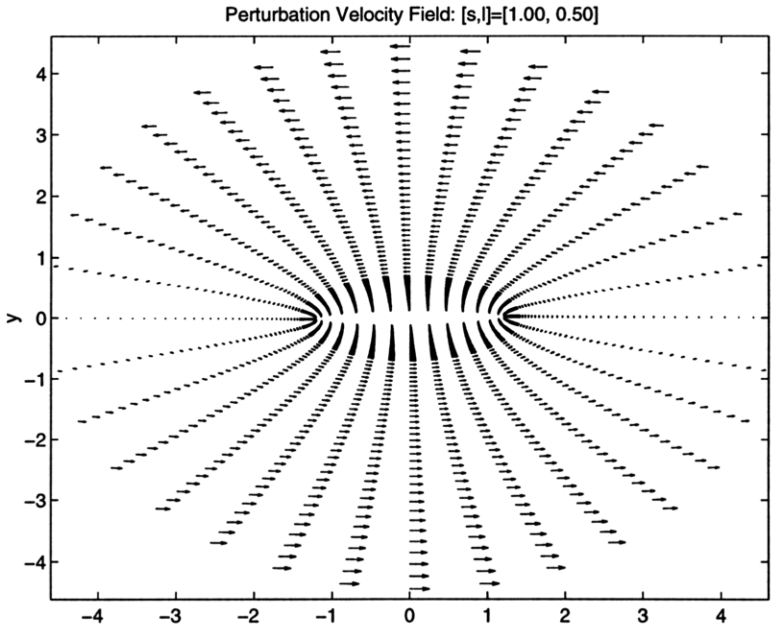

Figure 3-5: Elliptical vortex velocity field

3.3 Stability Analysis

3.3.1 Schwarzschild Criterion

One stability analysis examines the thermal and mechanical stability of the gas against convection. With both temperature and density gradients, if a parcel of gas moves, the thermodynamic changes can result in either a restoring force which brings the parcel back to its original location, or a buoyant force which causes additional drift [35]. The requirement for stability,

$$-\frac{1}{\gamma}\frac{1}{p}\frac{dp}{dr} < -\frac{1}{\rho}\frac{d\rho}{dr} \qquad \text{(stability)}, \tag{3.61}$$

can be written with temperature and density using the logarithmic derivative of the ideal gas law,

$$\frac{1}{p}\frac{dp}{dr} = \frac{1}{\rho}\frac{d\rho}{dr} + \frac{1}{T}\frac{dT}{dr}, \tag{3.62}$$

giving the stability condition

$$\frac{d(\ln T)}{dr} < (\gamma - 1)\frac{d(\ln \rho)}{dr} \qquad \text{(stability)}, \tag{3.63}$$

which is sensitively dependent on the ratio of the specific heats.

3.3.2 Axisymmetric Perturbations: Rayleigh' Criterion

The stability of an axisymmetric fluid flow is described by Rayleigh's criterion, which examines the angular momentum of a parcel of fluid as it moves radially in or out from an initial position. The flow is rotationally unstable, with a parcel which moves outward pushed further out, if

$$\frac{d}{dr}[(r^2\Omega)^2] < 0 \qquad \text{(instability)}. \tag{3.64}$$

For the Keplerian disk, this gives

$$\frac{d}{dr}[(r^2 k_k r^{-3/2})^2] = k_k^2 > 0, \tag{3.65}$$

so the disk is stable. This criterion indicates that the thin solar nebula disk with a Keplerian velocity profile is a stable representation of the flow. If Rayleigh's criterion had not been satisfied, the mean background flow would be strongly altered. The epicyclic frequency is

$$\kappa^2 = \frac{1}{r^3}\frac{d}{dr}[(r^2 k_k r^{-3/2})^2] = \Omega^2. \tag{3.66}$$

Since the epicyclic frequency is real, a parcel of gas which is displaced from the mean position will oscillate about the original position.

3.3.3 Planar Perturbations: Rayleigh's Inflection Theorem

For a two-dimensional linear or circular flow, the flow is stable if the vorticity gradient does not change sign [11]. For the Keplerian disk, the vorticity gradient,

$$\frac{\partial \bar{q}}{\partial r} = -\tfrac{3}{4} k_k r^{-5/2}, \tag{3.67}$$

is negative everywhere, so that vortices cannot form by drawing energy from the Keplerian shear. Instead, some initial, non-infinitesimal vorticity is required. The three-dimensional flow of the cloud settling into a disk may be one initial source of turbulence. In addition, magnetic fields may significantly change the stability criterion [10].

3.3.4 Steady Vortex Flows

A condition for steady flow is that the fluid characteristics such as the vorticity are constant along the streamlines, since the fluid follows the streamlines. In the case when this condition is not met, the characteristics of the fluid change over time. Since the streamlines are contours of the streamfunction, a quantity such as the vorticity is constant on the streamlines if it is a function of the streamfunction,

$$q = F(\psi) = \nabla^2 \psi. \tag{3.68}$$

The background flow also obeys this relationship, although the functional form may be different,

$$\bar{q} = \tilde{F}(\bar{\psi}) = \nabla^2 \bar{\psi}. \tag{3.69}$$

With the background values given by Eq. 2.32, the function for the background flow is

$$\tilde{F}(\bar{\psi}) = 12\,\Omega_{ko}^4\, r_0^6\, \bar{\psi}^{-3}. \tag{3.70}$$

The perturbation streamfunction,

$$\psi' = \psi - \bar{\psi}, \tag{3.71}$$

obeys

$$\nabla^2 \psi' = F(\bar{\psi} + \psi') - \tilde{F}(\bar{\psi}). \tag{3.72}$$

On streamlines which extend far from the vortex, the functional forms must be the same. With small perturbations, the right hand side is given by the second term of the Taylor series, so

$$\nabla^2 \psi' - \frac{d\tilde{F}}{d\psi}(\bar{\psi})\psi' = 0, \tag{3.73}$$

which is a spatial wave equation. This equation is most accurate far from the vortex, where the flow is only weakly perturbed from the background; the asymptotic form of the vortex is therefore determined by this equation. A negative derivative of $\tilde{F}$ gives sinusoidal solutions to the wave equation, resulting in waves which dissipate characteristics along the streamlines. A positive derivative gives a solution of decaying modes which are not dissipative, and growing modes which are not physically possible since they require the generation of vorticity. In the Keplerian case, the derivative is

$$\frac{d\tilde{F}}{d\psi}(\bar{\psi}) = -[6\Omega_{ko}^2 r_0^3 \bar{\psi}^{-2}]^2, \tag{3.74}$$

so that wavelike solutions result. In the case of a vortex in the solar nebula disk, the goal is therefore not to find stable or completely steady vortices, but rather to find the characteristics of robust vortices, which persist for a significant amount of time compared to other formation timescales, particularly the timescale for the coagulation of dust.

Chapter 4

Numerical Model and Experiments

The evolution of a vortex can be determined by integrating the vorticity equation of the form given by Eq. 3.34. A pseudospectral method can be used to transform the spatial derivatives into wavenumber-space products, while performing the existing products in real-space. This eliminates any explicit derivatives, so the vorticity equation becomes a first-order ordinary differential equation. A number of standard methods are available to solve the ODE, and a fourth-order Runge-Kutta scheme is used. The underlying characteristics of the partial differential equation are not eliminated, including the CFL criterion, which must still be satisfied [8].

The numerical model can then be used to perform a variety of experiments, depending on the initial vorticity field. With a single vortex, the relationship between the strength, aspect ratio, and size can be measured, as well as the degradation of the vortex over a long time relative to the formation timescales. For multiple vortices, the time required for merging can be calculated for vortices which are separated angularly as well as radially. Finally, for a random vorticity field, the accumulation of vorticity into a strong vortex is observed.

The flow will be confined between rigid boundaries at the inner and outer edge of the domain. This is clearly artifical, but it allows avoidance of the singularity at the Sun and difficulties in the far-field. Tests indicate that the results are not being strongly influenced by the boundaries.

4.1 Numerical Model

The numerical model includes a number of features: two-dimensional fast fourier transforms (FFT's), wavenumber-space derivatives, wavenumber-space filtering, a pseudospectral force term, and a fourth-order Runge-Kutta ordinary differential equation integration scheme.

4.1.1 Two-Dimensional Fourier Transforms

A variety of fourier transforms are available to use with the numerical model: sine and cosine transforms, real exponential transforms, and fully complex transforms. The first three are periodic, and the sine and cosine transforms also have boundary conditions. If the value of the function is zero at the boundaries, the sine transforms can be used; if the derivative is zero at the boundaries, the cosine transforms can be used.

The fluid perturbation quantities can be regarded as periodic in the angular coordinate, but the boundary values are unspecified, so the exponential transform is used for the x-transforms. Some variables vanish at the radial boundaries, so sine transforms can be used for the y-transforms of these quantities. Others are the derivatives of the sine transformed quantities, so cosine transforms are used for these.

The sine and cosine forward and inverse transforms have real values as both the inputs and outputs. The forward exponential transform has real inputs and complex outputs, while the inverse exponential transform has complex inputs and real outputs. The two-dimensional forward transform therefore does the sine/cosine y-transform first and then the exponential x-transform. The inverse transform order is reversed: the inverse exponential x-transform is performed, followed by the inverse sine/cosine y-transforms.

These transforms are performed as a sequence of one-dimensional transforms on rows or columns of data, using the functions provided in Numerical Recipes [32, §17.1]. Although the direct two-dimensional transform is more efficient than a sequence of one-dimensional complex transforms, the sequence with sine/cosine and exponential transforms has some advantages. First, there is a factor of eight more space required for the full two-dimensional transform, two from the x-transform and four from the y-transforms. In addition, there is an advantage of the corresponding $8\sqrt{8}$ factor of time for the transforms. Also, the boundary conditions are directly enforced by the transforms.

The transforms are calculated on discretized data, so the x-y data must be sampled on a grid. Both the region size and the number of grid points must be specified to get the values on the grid. With

X, Y	spatial region size
K, L	number of grid points
x, y	spatial coordinates
m, n	grid index for x,y
k, l	wavenumbers in x,y directions

the spatial region is assumed to be in the first quadrant. The spatial coordinates are related to the spatial grid indices by

$$x = m\frac{X}{K}, \tag{4.1.a}$$

$$y = n\frac{Y}{L}, \tag{4.1.b}$$

and the sampled data of the function $f(x, y)$ is

$$f_{mn} = f\left(m\frac{X}{K}, n\frac{Y}{L}\right). \tag{4.2}$$

Since the system is periodic in x and at least semi-periodic in y, the radial and angular boundaries can be specified by $X = 2\pi$, $Y = 2\pi$.

The sine and cosine transforms are

$$\hat{F}_{kl} \equiv \mathcal{F}_s\{f_{mn}\} = \sum_{m=1}^{K-1}\left[\sum_{n=0}^{L-1} f_{mn}\sin\left(\frac{Yln}{L}\right)\right]e^{iXkm/K}, \tag{4.3.a}$$

$$\tilde{F}_{kl} \equiv \mathcal{F}_c\{f_{mn}\} = \sum_{m=1}^{K-1}\left[\sum_{n=0}^{L-1} f_{mn}\cos\left(\frac{Yln}{L}\right)\right]e^{iXkm/K}, \tag{4.3.b}$$

where the hat and tilde indicate the sine and cosine transformed quantities respectively.

The inverse transforms are

$$\begin{aligned} f_{mn} &= \mathcal{F}_s^{-1}\left\{\hat{F}_{kl}\right\} = \frac{4}{KL}\sum_{l=0}^{L-1}\left[\sum_{k=1}^{K-1}\hat{F}_{kl}e^{-iXkm/K}\right]\sin\left(\frac{Yln}{L}\right), & (4.4.a)\\ &= \mathcal{F}_c^{-1}\left\{\tilde{F}_{kl}\right\} = \frac{4}{KL}\sum_{l=0}^{L-1}\left[\sum_{k=1}^{K-1}\tilde{F}_{kl}e^{-iXkm/K}\right]\cos\left(\frac{Yln}{L}\right), & (4.4.b)\end{aligned}$$

or, in terms of x, y,

$$\begin{aligned} f(x,y) &= \frac{4}{KL}\sum_{l=0}^{L-1}\left[\sum_{k=1}^{K-1}\hat{F}_{kl}e^{-ikx}\right]\sin(ly), & (4.5.a)\\ &= \frac{4}{KL}\sum_{l=0}^{L-1}\left[\sum_{k=1}^{K-1}\tilde{F}_{kl}e^{-ikx}\right]\cos(ly). & (4.5.b)\end{aligned}$$

Each direction requires a $2/K$ normalization, resulting in the $4/KL$ factor for the inverse transforms.

4.1.2 Spatial Derivatives

The derivatives of the function $f(x,y)$ can be related to the wavenumber-space function by taking the derivatives of the inverse transform equations, Eq. 4.5. For the y-derivatives, the sine functions give cosines, while the cosines give negative sines, so differentiation switches which transform is appropriate. The transforms of the derivatives are then the wavenumber-space quantities multiplied by factors related to the wavenumbers, where care must be taken to use the correct transformed quantities. With the x and y derivatives of Eq. 4.5,

$$\begin{aligned} \frac{\partial f}{\partial x} &= \frac{4}{KL}\sum_{l=0}^{L-1}\left[\sum_{k=1}^{K-1}(-ik)\hat{F}_{kl}e^{-ikx}\right]\sin(ly), & (4.6.a)\\ \frac{\partial f}{\partial y} &= \frac{4}{KL}\sum_{l=0}^{L-1}\left[\sum_{k=1}^{K-1}(-l)\tilde{F}_{kl}e^{-ikx}\right]\sin(ly), & (4.6.b)\\ &= \frac{4}{KL}\sum_{l=0}^{L-1}\left[\sum_{k=1}^{K-1}(+l)\hat{F}_{kl}e^{-ikx}\right]\cos(ly), & (4.6.c)\end{aligned}$$

the transforms of the derivatives are

$$\begin{aligned} \widehat{\frac{\partial f}{\partial x}} &= -ik\hat{F}_{kl} \\ \widetilde{\frac{\partial f}{\partial x}} &= -ik\tilde{F}_{kl} \end{aligned}\quad , \qquad \begin{aligned} \widehat{\frac{\partial f}{\partial y}} &= -l\tilde{F}_{kl} \\ \widetilde{\frac{\partial f}{\partial y}} &= l\hat{F}_{kl} \end{aligned}\quad . \tag{4.7}$$

The transform of the second derivatives are of the same form as the transform of the function, so the transform of the Laplacian is

$$\mathcal{F}_{s,c}\left\{\left(\frac{\partial^2}{\partial x^2}+\frac{\partial^2}{\partial y^2}\right)f\right\} = -(k^2+l^2)\mathcal{F}_{s,c}\{f\} \tag{4.8}$$

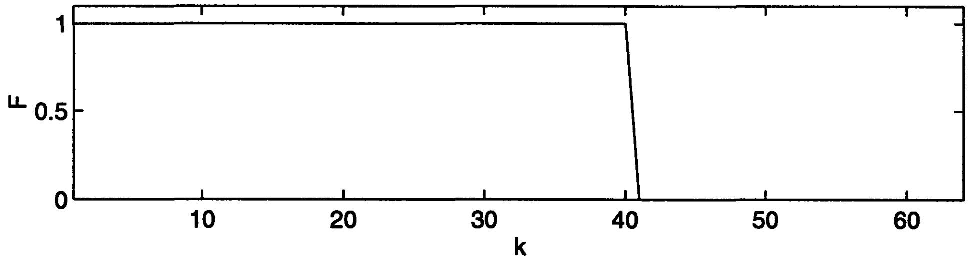

Figure 4-1: One-dimensional filter function

for both transforms. The inverse Laplacian follows as

$$\mathcal{F}_{s,c}\left\{\nabla^{-2}f\right\} = -\frac{1}{k^2+l^2}\mathcal{F}_{s,c}\left\{f\right\}, \tag{4.9}$$

except there are constants of integration for the first two wavenumbers, which must be specified based on other data such as boundary conditions.

4.1.3 High-Wavenumber Filtering

The fourier transforms will introduce some errors in the higher wavenumber modes. This is compounded by the tendency of vorticity to shift towards higher wavenumbers. The energy in the flow, on the other hand, tends to shift to the lower wavenumbers, Therefore, the higher frequency modes can be filtered out with negligible loss of information in the flow. This can be done with a filtering function which is constant for the pass band and then has a rapid drop-off at a cutoff wavenumber, k_c. A filter of the form

$$F(k;k_c,w) = \begin{cases} 1.0 & k < k_c \\ e^{-((k-k_c)/w)^8} & k > k_c \end{cases} \tag{4.10}$$

is used for the pass band edge of width w since the slope is zero at both $(k-k_c) = 0$ and $(k-k_c) \gg w$, and the edge is sharper than for a Gaussian. The filter function is shown in Fig. 4-1.

Since the energy modes, ε_j, are grouped by the value of the square of the total wavenumber,

$$j^2 = k^2 + l^2, \tag{4.11}$$

the two-dimensional filter will have a cutoff wavenumber of

$$(k^2+l^2) < \left(\frac{5}{8}\right)^2 J^2, \tag{4.12}$$

where $J = \min(K, L)$. This gives the pass band in k, l as shown in Fig. 4-2.

4.1.4 Force Term Calculations

The vorticity equation of the form in Eq. 3.34 can be written with the right-hand side given by the force term,

$$g(Q') = [(\bar{\psi}_y + \psi'_y)q']_x - (\psi'_x\bar{q}_y) - (\psi'_x q')_y, \tag{4.13}$$

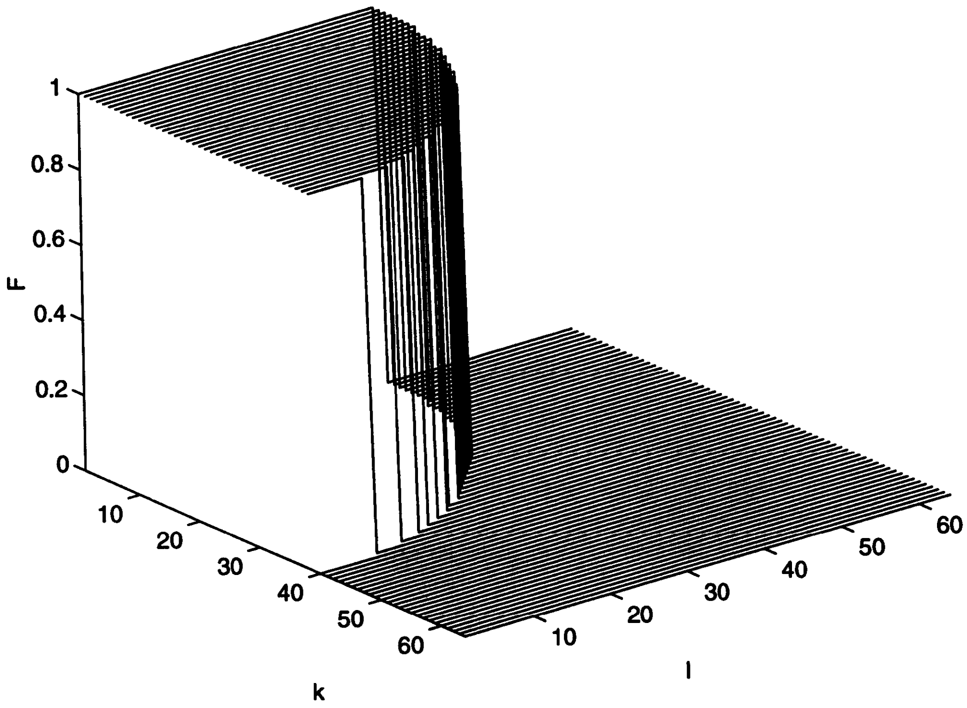

Figure 4-2: Two-dimensional filter function

where

$$Q' \equiv \left(\frac{r}{M}\right)^2 q'. \tag{4.14}$$

The flowchart in Fig. 4-3 shows the steps taken to calculate the force term for each integration step. One pair of transforms are saved by integrating the vorticity equation in wavenumber space instead of in real space.

4.1.5 Runge-Kutta Temporal Integration

The vorticity equation takes the form

$$\frac{d\hat{Q}'}{dt} = g(\hat{Q}'), \tag{4.15}$$

with no explicit spatial derivatives of $\hat{Q}'$ being calculated; this equation then becomes an ordinary differential equation which can be solved by a number of standard methods. The biggest advantage of the ODE solution is that an explicit scheme can be used, while an implicit scheme would be preferred for a hyperbolic PDE [40]. While a simple Euler method could be used, a fourth-order Runge-Kutta scheme offers greater accuracy. The drawback is that four calculations of the force term are required for one time step, but the improved accuracy is more important.

The RK4 scheme involves four calculations of the force term,

$$\begin{aligned} G_1 &= g(Q_0), && (4.16.a)\\ G_2 &= g(Q_0 + \tfrac{1}{2}h\,G_1), && (4.16.b)\\ G_3 &= g(Q_0 + \tfrac{1}{2}h\,G_2), && (4.16.c)\\ G_4 &= g(Q_0 + h\,G_3) && (4.16.d)\\ ,Q_1 &= Q_0 + \tfrac{h}{6}(G_1 + 2G_2 + 2G_3 + G_4) * F(k), && (4.16.e) \end{aligned}$$

where the filter as described by Eq. 4.10 is used to eliminate the high wavenumber errors.

4.1.6 Numerical Integration Parameters

A number of parameters used in performing the calculations are listed in Table 4.1. The shear mode specifies whether the shear is Keplerian, or if zero shear or constant shear test cases are being used. The position of the origin and the periodicity, (r_0, M), specify the region being examined in annular coordinates, as described in §A.3. These coordinate parameters, combined with the region sizes, $(X = 2\pi, Y = \pi)$, also specify the distance to the center of the region, r_c, and the orbit period at that radius, τ_c,

$$\begin{aligned} r_c &= r_0 e^{\pi/M}, && (4.17.a)\\ \tau_c &= \frac{2\pi}{k_k} r_c^{+3/2}. && (4.17.b) \end{aligned}$$

The units of the orbit period are in T, the time unit of the calculations. If $k_k = 2\pi$, the time unit is $T = 1\,\mathrm{yr}$; if, however, $k_k = 1$, then $T = 1/2\pi \approx 0.16\,\mathrm{yr}$. Values used for the integration parameters are shown in Table 4.2.

The number of grid points in the region is a power of two in each direction, to make the FFTs most efficient. Most calculations are performed with 64×64 or 128×128 grids.

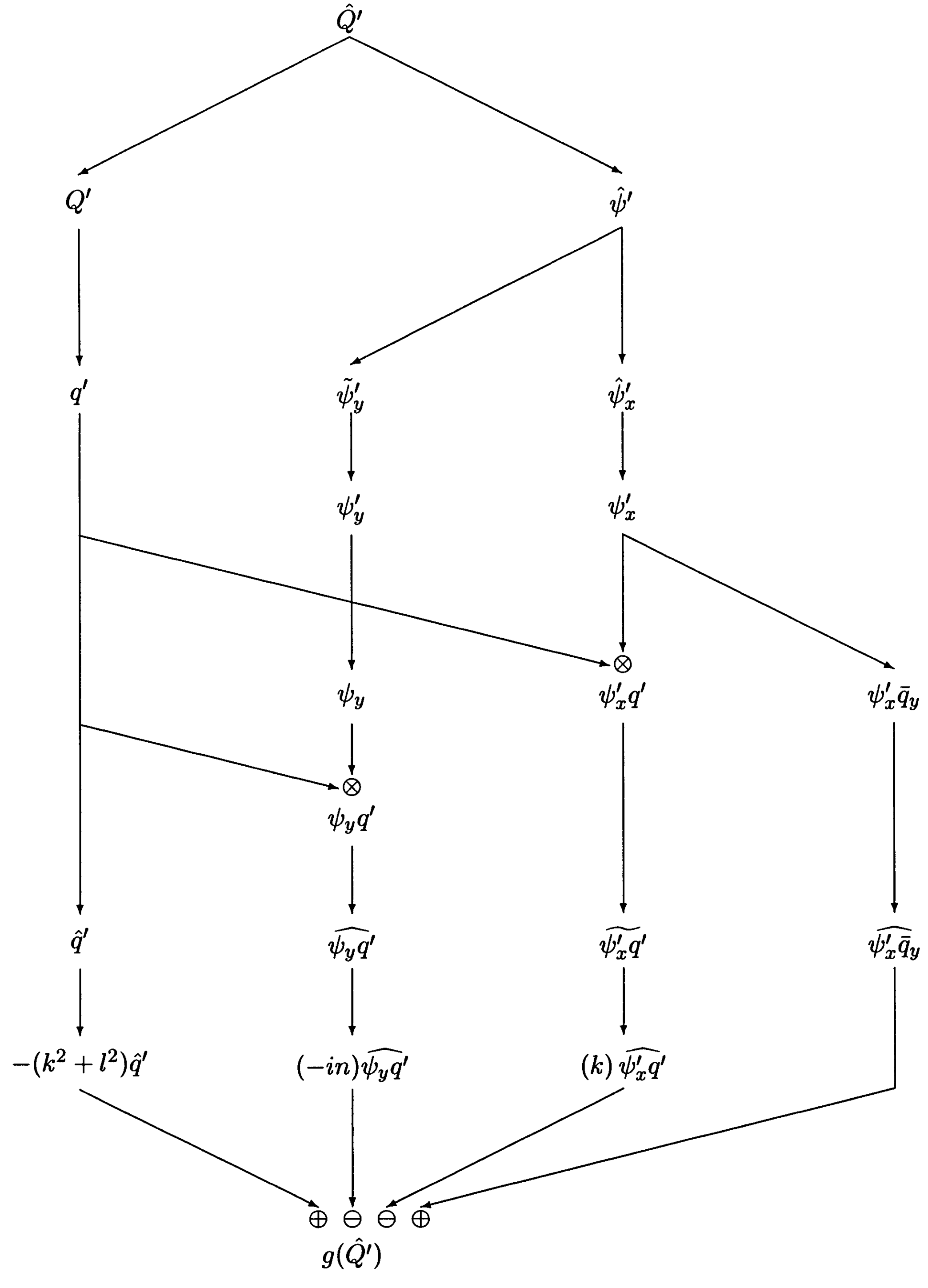

Figure 4-3: Flow of algorithm for force term

Table 4.1: Numerical integration parameters

N_{xy}	grid size (assume equal in x and y)
s_{mode}	shear mode
r_0	position of origin
M	periodicity
h	integration timestep
ns	number of timesteps per output block

Table 4.2: Values for integration parameters

Parameter	Range of Values	Character Code
N_{xy}	2^{i_N}, $i_N = [6:8]$	'a'-1 + i_N
s_{mode}	Keplerian; zero; const ($s = [0.1 : 0.6]$)	k; z; a:f
r_0	$1, 2, 5, 10, 20$	a:e
M	$2, 3, 4, 5, 10$	b:f
h	$[1.0, 0.5, 0.2] * 10^{-(i_h/3)}$, $i_h = [6:13]$	'a'+i_h
n_s	$[1, 2, 5] * 10^{(i_{ns}/3)}$, $i_{ns} = [0:9]$	'a'+i_{ns}

The shear can be one of several types: zero, constant, or Keplerian. The first is used to test the numerical model—the vortex should be steady with zero shear [13]. The constant shear case is used to compare the model with analytical results [26], with a range of values used to see the effects on the vortex shape. The calculations of interest, however, are with the Keplerian shear case, where the region parameters, (r_0, M), will specify the shear strength, du/dy.

The region parameters can both have a wide range of values, although most interesting cases fall within a small group, as specified in Table 4.2. If r_0 is large, it primarily examines the outer solar system. If M is large, a small portion of the annulus is selected, approaching a Cartesian limit as discussed in §A.3.5. Values for r_c for different values of (r_0, M) are shown in Table 4.3. The outer radii of the region are

$$r_1 = r_0 e^{2\pi/M} = r_c e^{\pi/M}, \tag{4.18}$$

which can be calculated from the data in Table 4.3.

The time integration values, (h, n_s), can also have a wide range of values, and are best selected in an approximately exponential manner, as specified in Table 4.2. The value of h is varied when testing the CFL criterion (see §4.4.1), and then only a few values are used. Smaller values for h are used with the finer grids, multiple vortex fields, and random vorticity fields, where finer temporal resolution is important to observe the merging of vortices.

4.2 Initial Vorticity Fields

Studies of vorticity in constant shear have shown that elliptical patches can be stable within certain parameter limits [26], so elliptical vorticity patches are used to study vortices in the Keplerian shear. The sharp cutoffs of a step-function patch, however, will result in significant

Table 4.3: Values of Central Radius, $r_c(r_0, M)$

		r_0				
M	$e^{\pi/M}$	1.0	2.0	5.0	10.0	20.0
10.0	1.4	1.4	2.7	6.8	13.7	27.4
5.0	1.9	1.9	3.7	9.4	18.7	37.5
4.0	2.2	2.2	4.4	11.0	21.9	43.9
3.0	2.8	2.8	5.7	14.2	28.5	57.0
2.0	4.8	4.8	9.6	24.1	48.1	96.2

energy in the higher-wavenumber modes with a pseudospectral method, so smooth functions are preferred. A two-dimensional Gaussian vorticity distribution has no sharp edges and is a better representation of a vortex. The elliptical vortex shape is specified by the widths of the Gaussian in the x and y directions.

Three types of initial vorticity fields are studied: a single vortex, multiple vortices, and a random vorticity field. The first two use Gaussian vortices; the third uses either a random set of Gaussian vortices or a random distribution of the vorticity wavenumber spectrum.

4.2.1 Single Vortex

The Gaussian elliptical vortex has the form

$$q(x, y) = q_c e^{-[(x-x_c)^2+\lambda^2(y-y_c)^2]/\sigma^2}, \tag{4.19}$$

where

q_c	vortex strength
(x_c, y_c)	center of vortex
λ	aspect ratio
σ	vortex size

The area of the vortex is

$$A = \pi\lambda\sigma^2. \tag{4.20}$$

For a single vortex, the center position is initially the center of the region, $x_c = \frac{1}{2}X, y_c = \frac{1}{2}Y$. The size of the vortex can be measured as a fraction of the size of the region. The strength can be specified exponentially, as can the aspect ratio. The orientation can be specified with $\lambda < 1$ for a vortex with the major axis in the x direction and $\lambda > 1$ for a vortex with the major axis in the y direction. It is useful to separate the vortices into four categories, with q_c positive or negative, and the orientation along the x or y direction. Then, the strength, aspect ratio, and size for a $-\hat{x}$ vortex are given by

$$q_c = -10^{-(i_q/3)},\ i_q = [0:9], \tag{4.21.a}$$

$$\sigma = \left(\tfrac{1}{4}N_{xy}\right)2^{-(i_\sigma/4)},\ i_\sigma = [0:8], \tag{4.21.b}$$

$$\lambda = 2^{-(i_\lambda/4)},\ i_\lambda = [0:8], \tag{4.21.c}$$

with character codes used for each ellipse parameter to distinguish the file names. The vorticity, streamfunction, and velocity fields are plotted in Figs. 4-4 and 4-5.

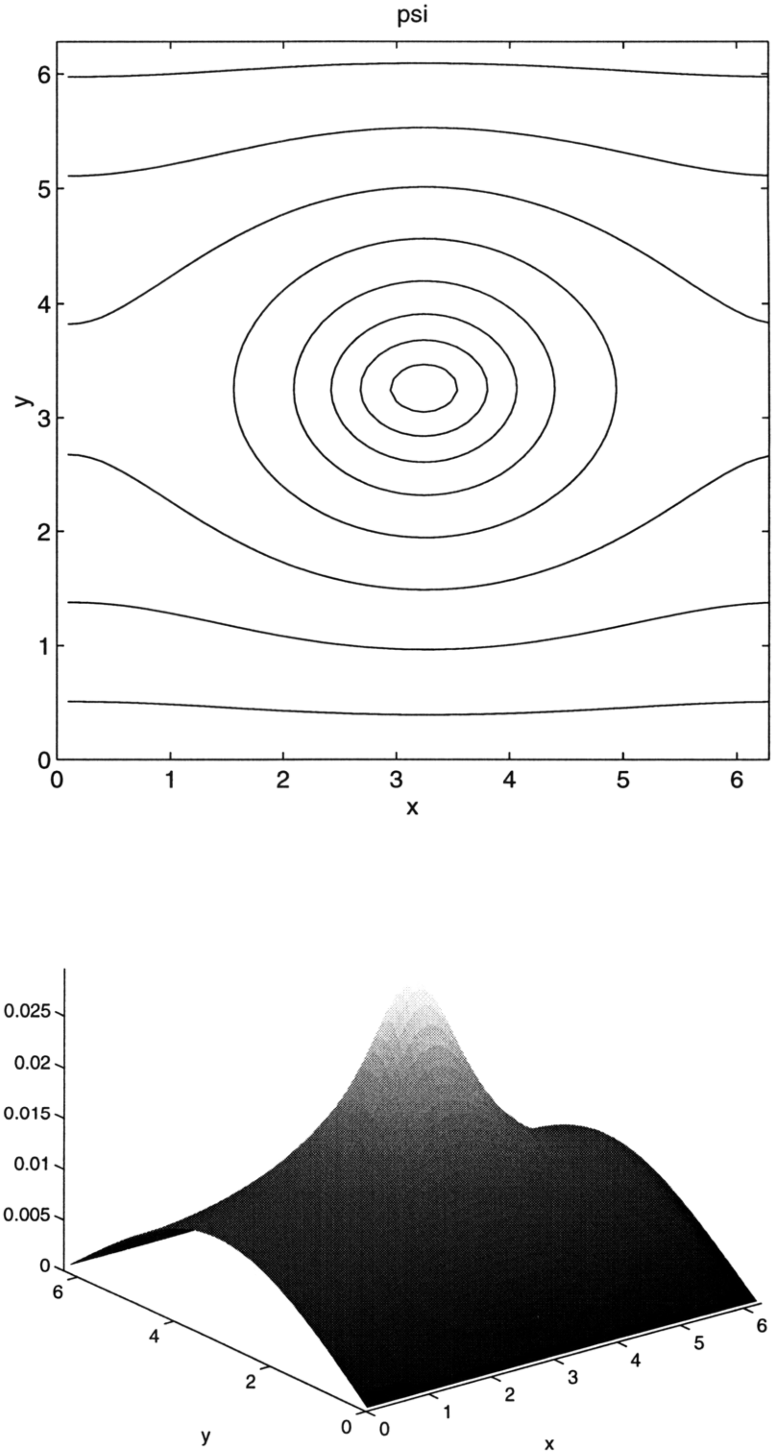

Figure 4-4: Single vortex streamfunction

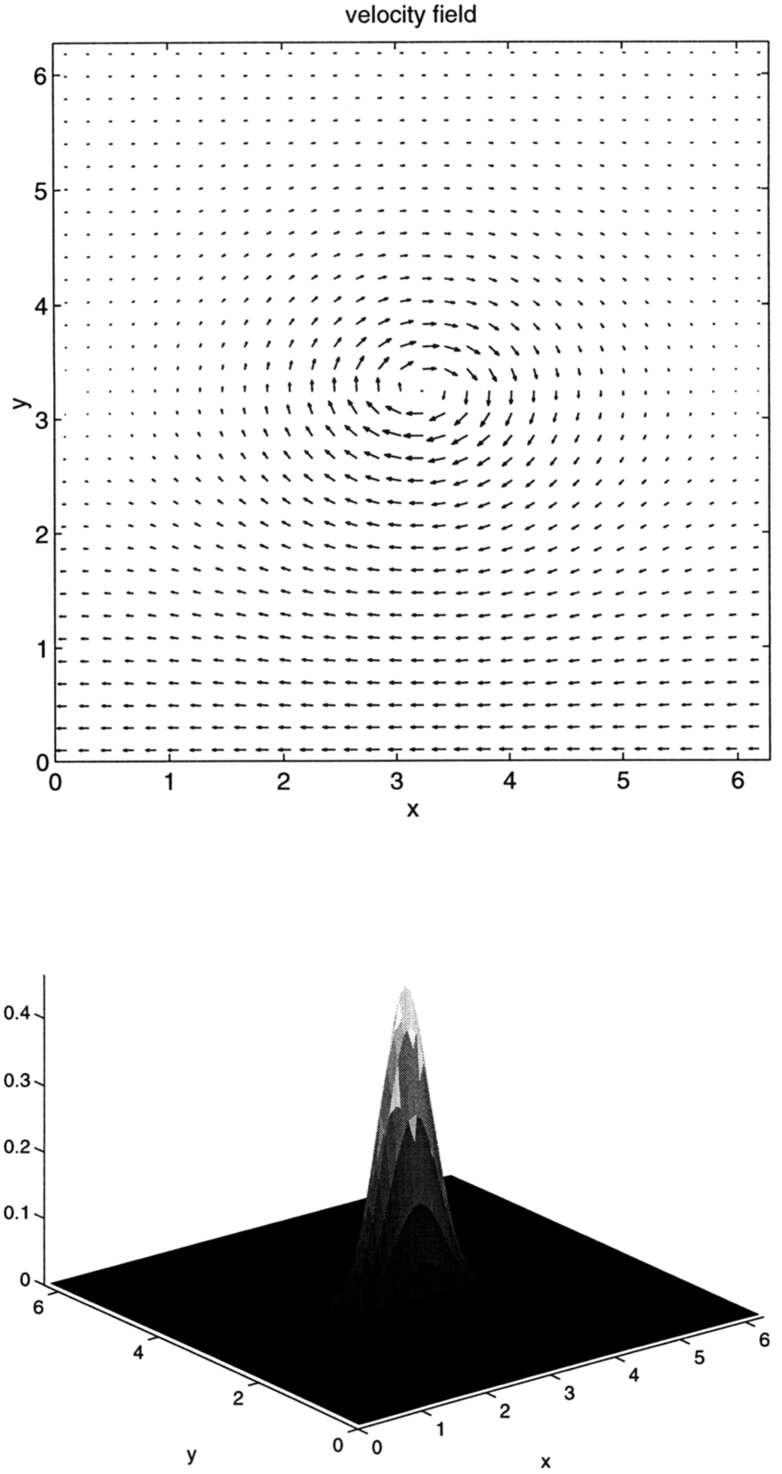

Figure 4-5: Single vortex velocity field and vorticity

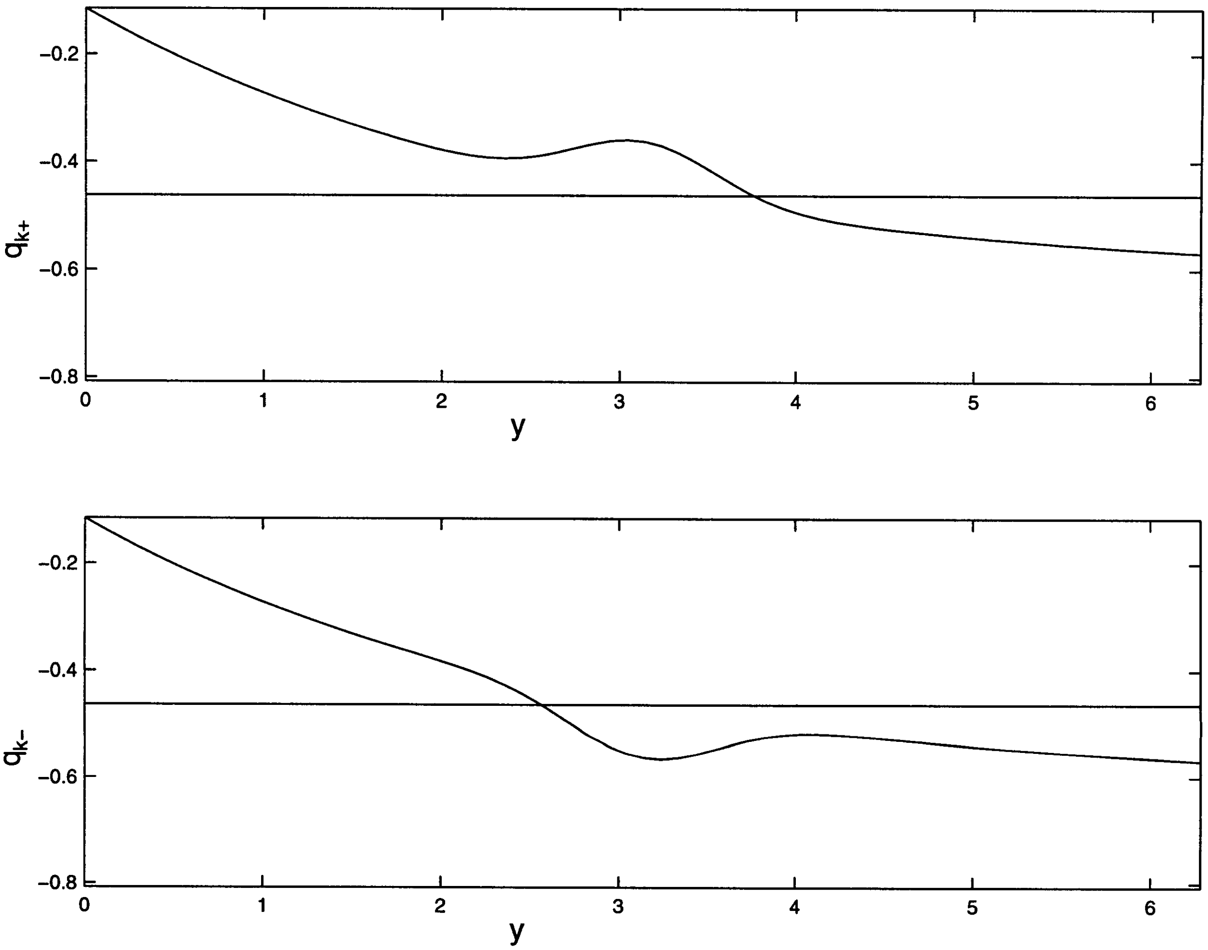

Figure 4-6: Single vortex radial vorticity profile

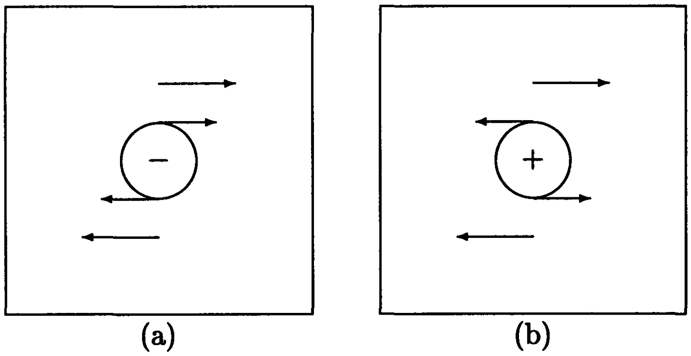

Figure 4-7: Positive and negative vortices in the Keplerian shear

4.2.2 Multiple Vortices

A field with multiple vortices can be generated by using Eq. 4.19 several times. The different vortices can be organized along one or several longitudinal lines, with y_c equal for each vortex. They can also be organized along a single radial line, with x_c fixed. Calculations with vortices of the same size and orientation are performed, as well as different sizes.

4.2.3 Random Vorticity Field

The random vorticity field can be generated in several ways. One option is to use random sizes and strengths for Gaussian vortices as described by Eq. 4.19, and then place them randomly in the field. A second alternative is to use a random power spectrum of vorticity, which then corresponds to a random vorticity field when transformed back to real space.

4.3 Numerical Experiments

4.3.1 Single Vortex: General Results

The first characteristic which distinguishes vortices is the sign of the vorticity: the negative vortex is prograde relative to the *local* flow, meaning the perturbation velocity is in the same direction as the background flow. In contrast, the positive vortex is retrograde with the flow opposing the background flow (Fig. 4-7). The vorticity profile of the total vorticity is seen in Fig. 4-6.

The velocity profile suggests that the negative vortex will be more persistent in the solar nebula. Calculations using the same vortex shape but with different signs are shown in Figs. 4-9, 4-12. The positive vortex has part sheared off, and the remaining vortex drifts radially inward until it encounters the inner boundary and edge effects result in numerical instabilities. The negative vortex remains essentially unchanged over the same period.

The second characteristic of the ellipse is the orientation of the major axis. If the major axis of the vortex is oriented along longitudes, the vortex gas spends more time flowing parallel to the background and less time perpendicular to it, as shown in Fig. 4-8. If the vortex is oriented with the major axis along radial lines, the gas spends more time flowing perpendicularly to the background, and the shear has a stronger effect. As seen in the plots of Fig. 4-11, some of the

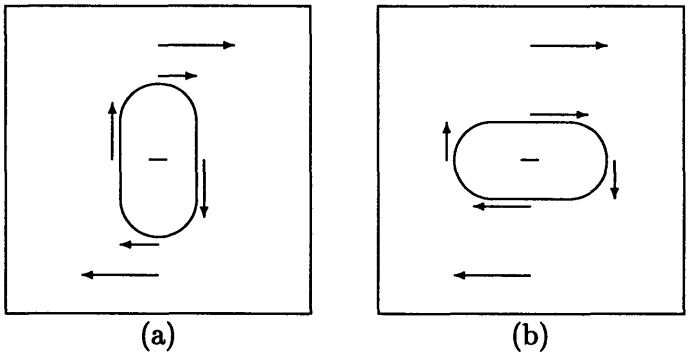

Figure 4-8: Elliptical vortices aligned radially and longitudinally

fringe vorticity is sheared off while the remaining vorticity is rearranged into a vortex with a longitudinal orientation.

4.3.2 Single Vortex: Vortex Parameters

After the orientation, the remaining parameters which describe the elliptical vortex include the amplitude, the length of the semi-major axis, the aspect ratio, and the angle of the major axis with respect to the x-axis. In addition, the area of the vortex is related to the length of the semi-major axis and the aspect ratio,

$$A = s^2\lambda, \tag{4.22}$$

and the position of the vortex center may move.

The vorticity field can be fit to a Gaussian of the form $q(x, y; E_i)$, where E_i are the parameters,

$$E_i = (q_c, x_c, y_c, \sigma, \lambda, \phi), \tag{4.23}$$

and

$$\begin{aligned} a &= (x - x_c)\cos\phi + (y - y_c)\sin\phi, & \text{(4.24.a)} \\ b &= -(x - x_c)\sin\phi + (y - y_c)\cos\phi, & \text{(4.24.b)} \\ q(x, y; E_i) &= q_c e^{-(a^2+b^2\lambda^2)/\sigma^2}. & \text{(4.24.c)} \end{aligned}$$

A least squares fit can be used to determine the parameters by minimizing

$$\delta = \frac{1}{N_{xy}^2} \sum_m \sum_n [q_{mn} - q(x_m, y_n; E_i)]^2. \tag{4.25}$$

It is important to examine both how the parameters are related to each other. Starting with different initial values for the strength and the aspect ratio, the vorticity field evolves for 80 yr. If the strength is insufficient to support the shape, the shear stretches the vortex and the outer regions of the vortex are torn away, leaving a smaller, more elongated vortex. An example is shown in Fig. 4-14.

The mean values of the strength, aspect ratio, size, and area parameters can be calculated for different initial values. In Fig. 4-15–4-17, these parameters are compared to each other, with symbols and grid lines used to show initial values. One initial size is used, $s_0 = 11.3$, with four values for $q_{c,0}$ and λ_0. Different symbols are used to indicate different values of λ_0,

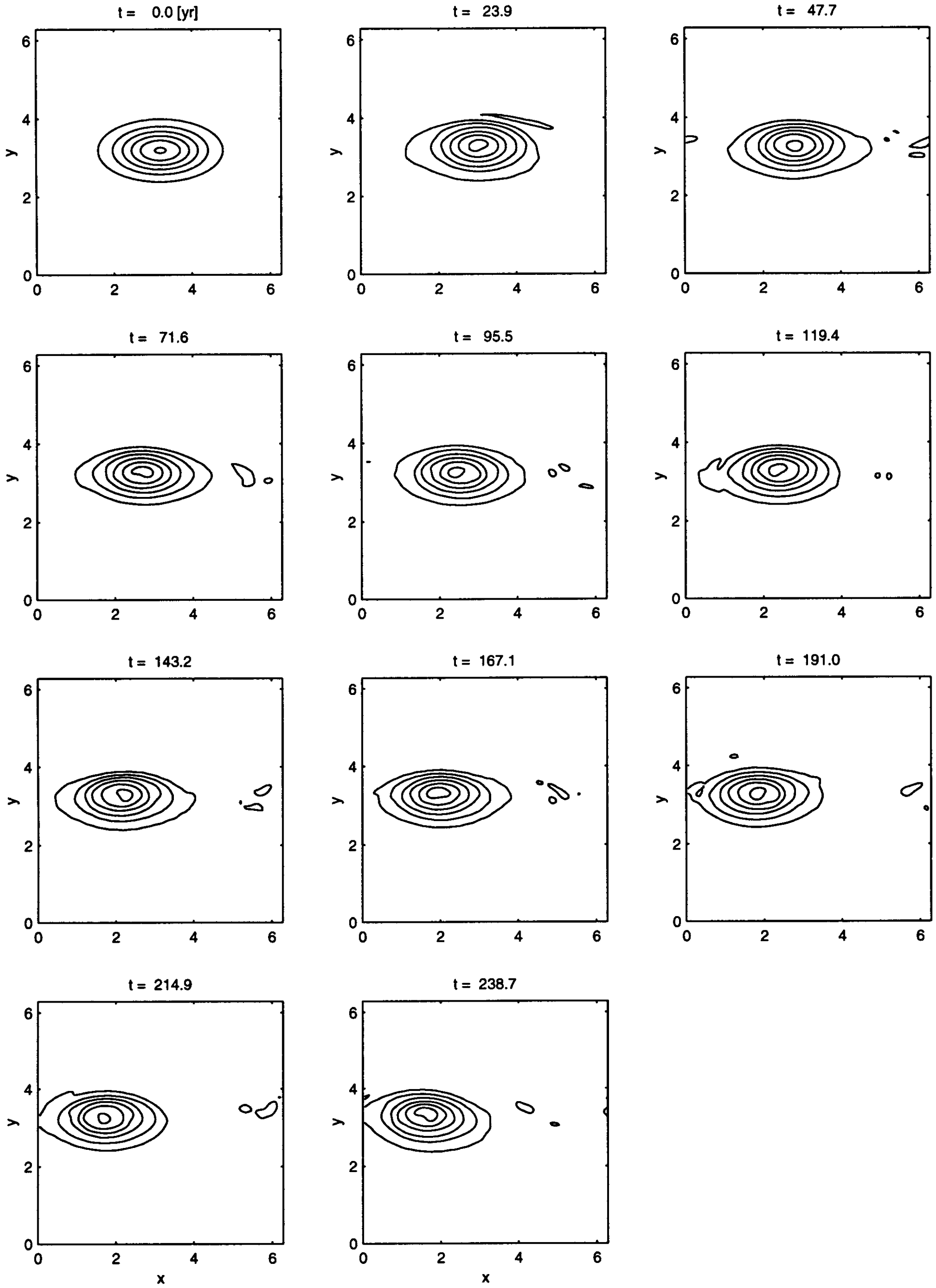

Figure 4-9: Negative vortex aligned with Keplerian shear, $[N_{xy}, O, \sigma, \lambda, q_c] = [64, +\hat{x}, 12, 0.5, -0.5]$; coded 'FACEB'.

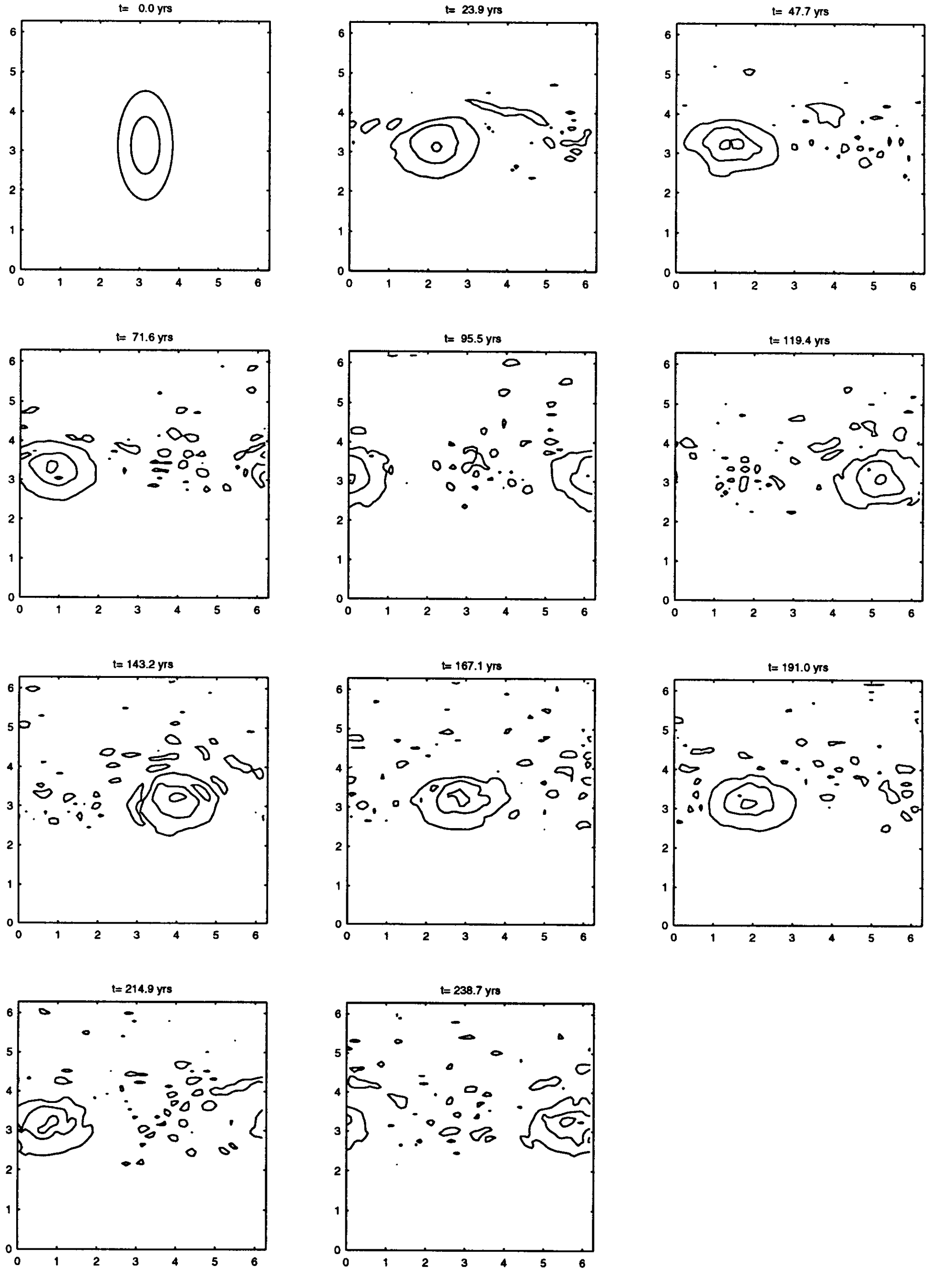

Figure 4-10: Similar to 'FACEB', except aligned perpendicular to the Keplerian shear with twice the strength; coded 'FBCEA'.

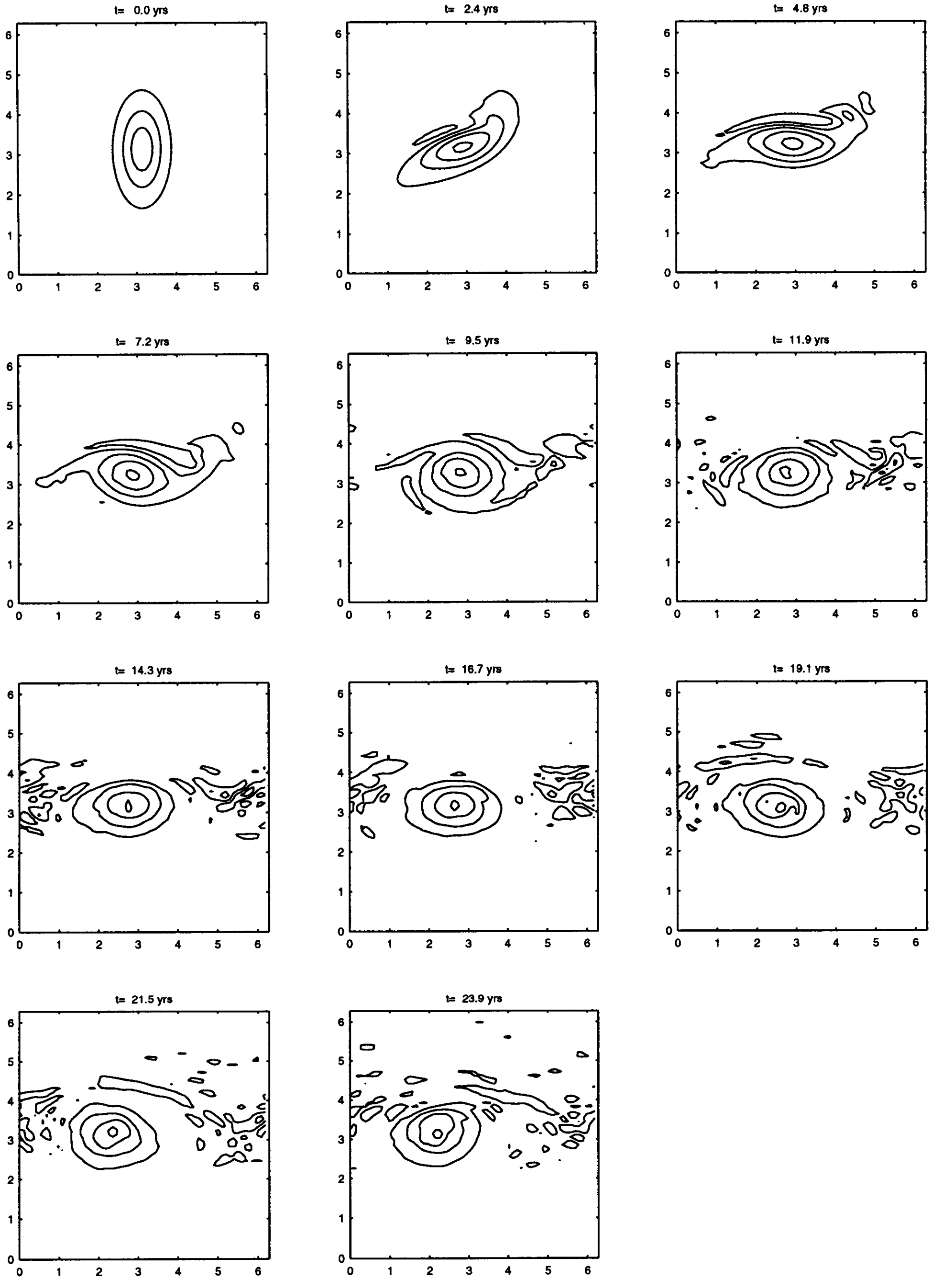

Figure 4-11: First time step of 'FBCEA'.

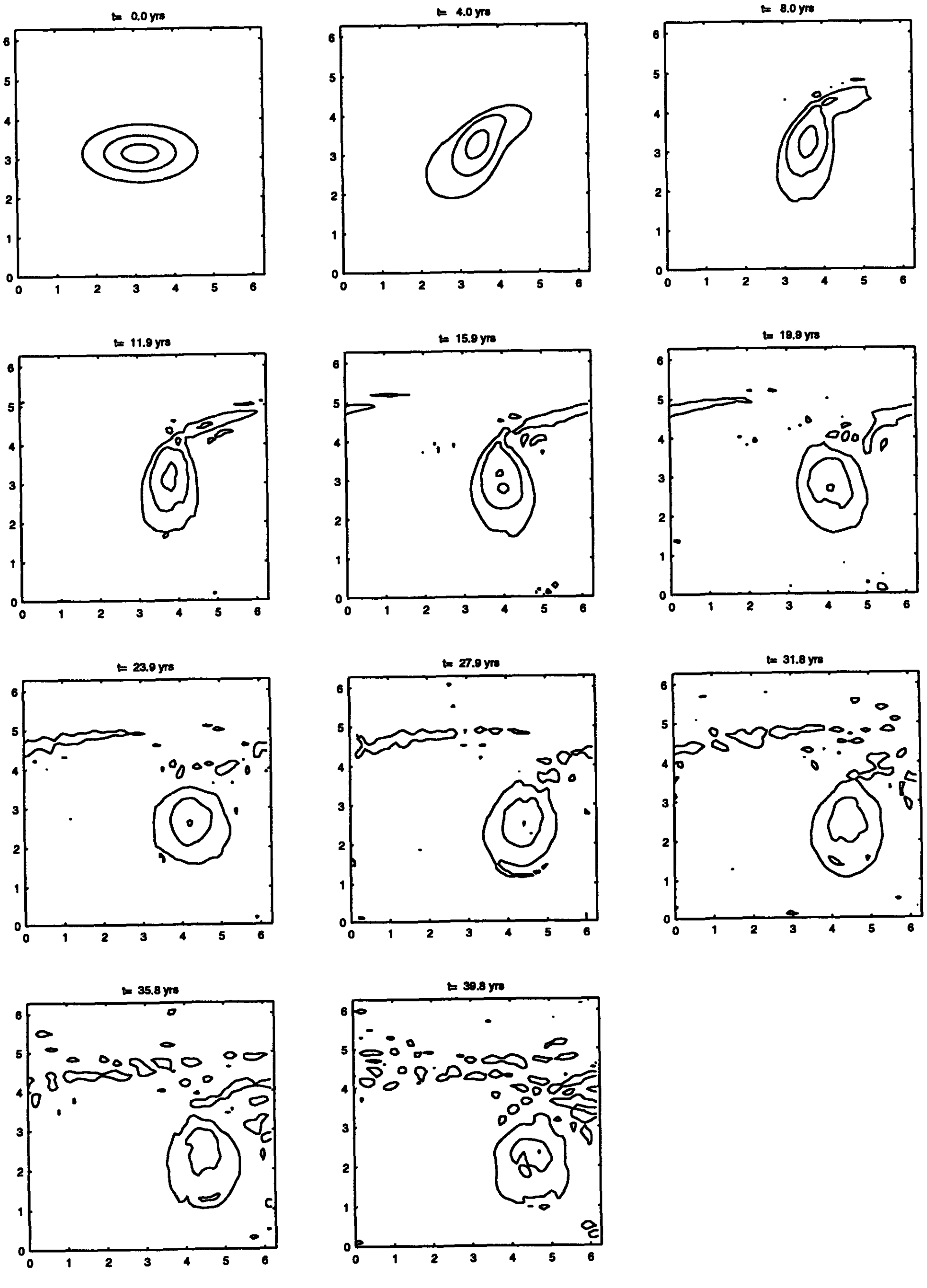

Figure 4-12: Same as 'FACEB', but with a positive vorticity and twice the strength.

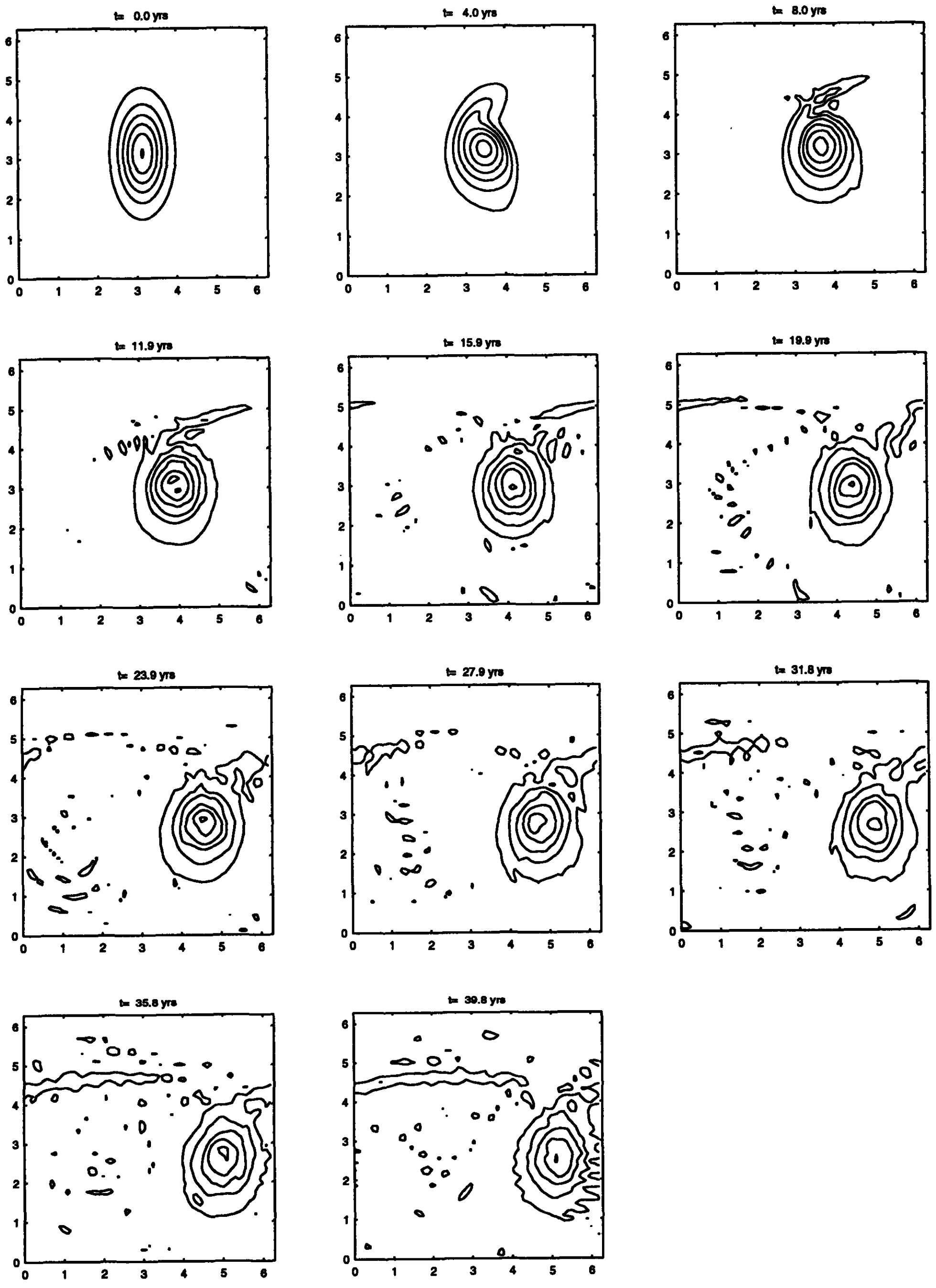
t= 0.0yrs

t= 4.0yrs

t= 8.0yrs

t= 11.9yrs

t= 15.9yrs

t= 19.9yrs

t= 23.9yrs

t= 27.9yrs

t= 31.8yrs

t= 35.8yrs

t= 39.8yrs

Figure 4-13: Same as 'FBCEA', but with a positive vorticity.

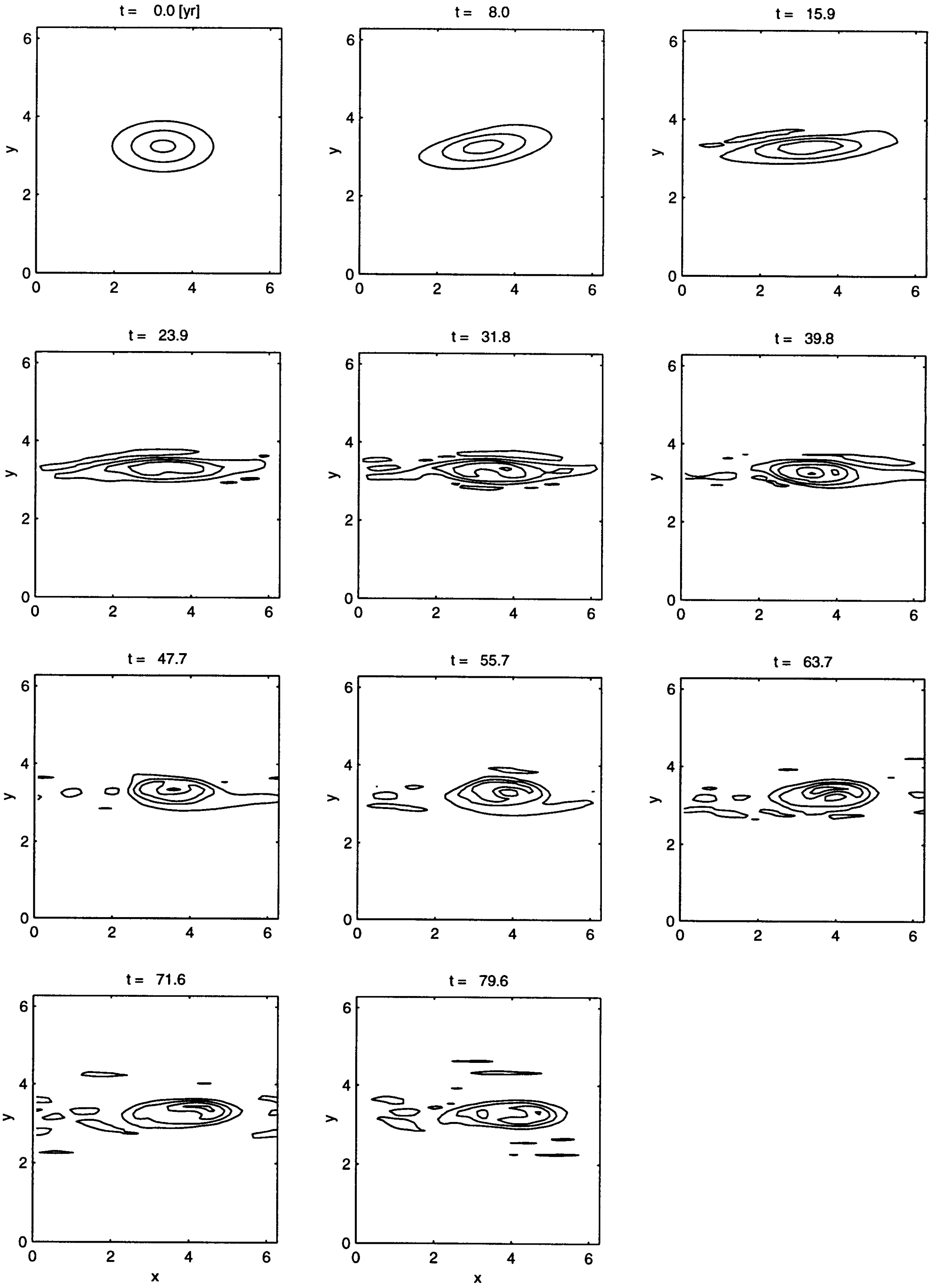

Figure 4-14: A weaker vortex than 'faceb', with a change in aspect ratio.

symbol	λ_0
○	0.71
×	0.50
+	0.35
∗	0.25
●	0.18

since the mean values can vary widely compared to the initial values. The same symbols are used for the initial area, with

$$A_0 = s_0^2\,\lambda_0 = 128\,\lambda_0. \tag{4.26}$$

The horizontal grid lines indicate the initial values for the aspect ratio or area, with one symbol corresponding to one grid line. The initial values for the strength are indicated by vertical grid lines, and since the mean values do not deviate significantly from the initial values, additional symbols are not used in Fig. 4-15–4-16. All vortices start with the same size, as indicated by the single vertical grid line in Fig. 4-17.

In Fig. 4-15, the aspect ratio is plotted as a function of vortex amplitude. This plot shows that the final aspect ratio of the vortex is closely related to the strength of the vortex, independent of the initial aspect ratio. This is consistent with the results for elliptical vortices, as described in §3.2.2, Eq. 3.42, which is also plotted in the figure.

In Fig. 4-16, the area of the vortex is plotted as a function of the vortex amplitude, and here the area is not changed significantly, generally less than ten percent. The area and the strength are fairly constant, which indicates the overall persistence of the vortex, as the area times the amplitude is a measure of the total vorticity contained in the vortex.

Finally, in Fig. 4-17, the aspect ratio is plotted as a function of the vortex size. This shows that the smaller vortices are rounder, with smaller aspect ratios. This is reasonable since the non-uniform shear of the background flow would have a larger effect on larger vortices, and it is the shear which causes the vortex stretching.

4.3.3 Single Robust Vortex

It is important to know how long a vortex may persist in the solar nebula, relative to other formation timescales, since the shear of the Keplerian velocity profile tends to disrupt the vortex. In addition, if the vortices do not remain long enough to affect the dust flow, then they cannot enhance the coagulation of dust particles.

A vortex is evolved over approximately 10^3 years to see the effects over a significant amount of time. This calculation required 5 days on a Pentium 200MHz computer; today, faster machines would allow even longer calculations. Since the time scale for aggregation is thought to be some fraction of 10^5 years, the persistence of vortices on a thousand year time scale is significant.

The vortex initially reshapes to conform to the relation between the strength and the aspect ratio, with some vorticity scattered throughout the field. Over the course of the calculation, there is little change in the subsequent shape, strength (less than 0.4% change in total vorticity), or distribution (less than 0.4% change in vorticity squared) of the vortex, as seen in Fig. 4-18. This particular initial vortex case is shown, rather than the case with the correct initial amplitude to aspect ratio relationship, since that would be preselecting the correct solution.

The calculations demonstrate that the stability of the Keplerian shear is not inconsistent with the persistence robust vortices.

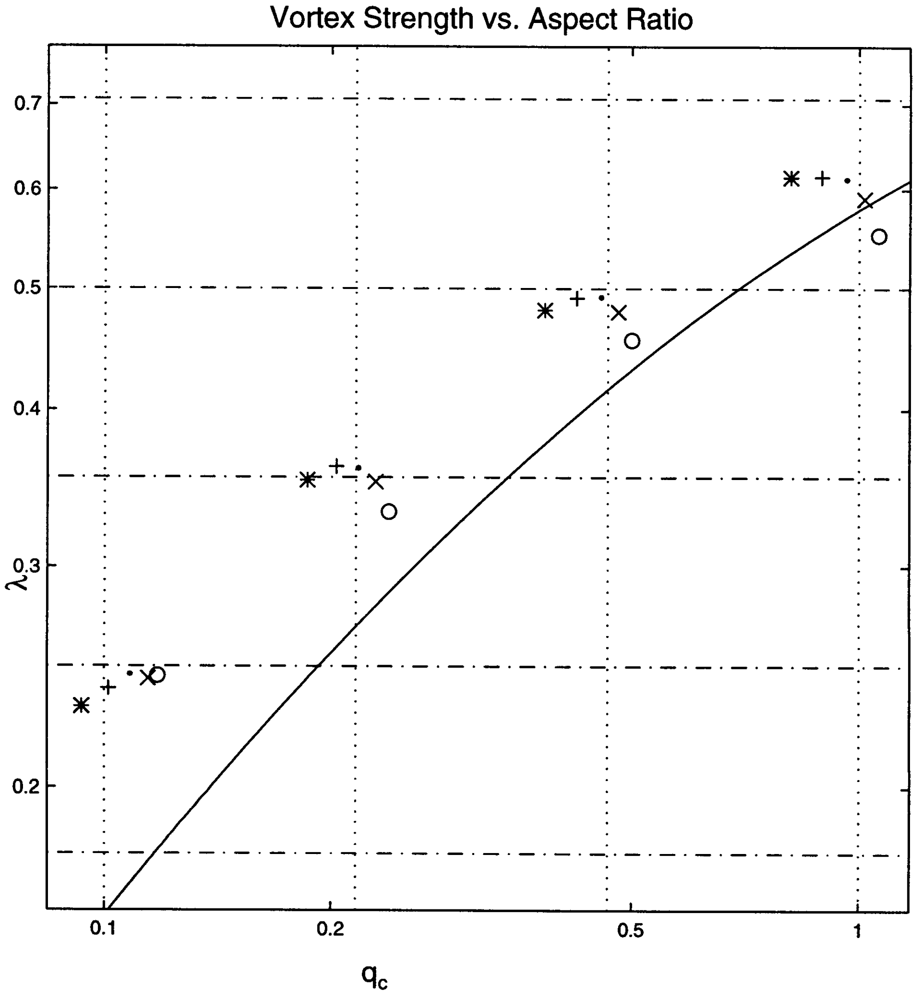

Figure 4-15: Vortex strength vs. aspect ratio; (symbol λ_0) pairs: ($\circ$ 0.71), ($\times$ 0.50), ($+$ 0.35), ($*$ 0.25), ($\bullet$ 0.18); $q_{c,0} = (-1.00, -0.46, -0.22, -0.10)$. Solid line is elliptical vortex solution for strength/aspect ratio dependence.

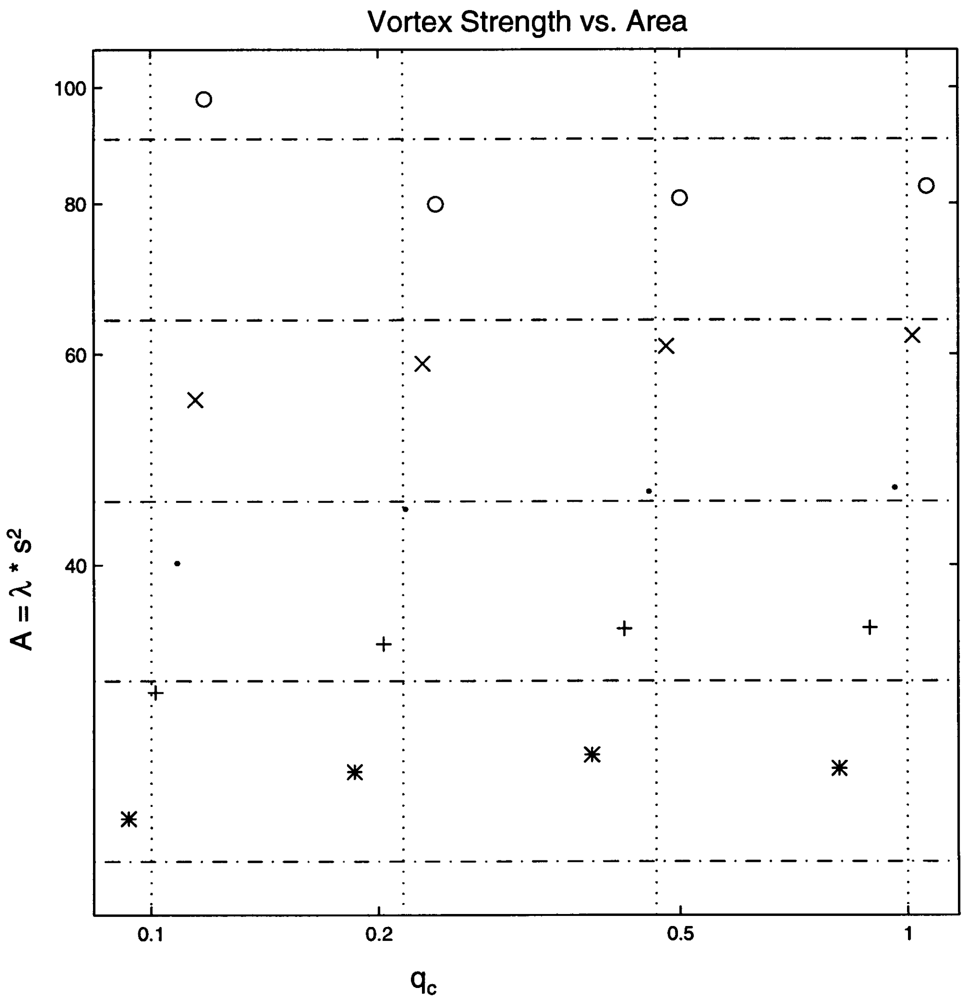

Figure 4-16: Vortex strength vs. area; (symbol A_0) pairs: (∘ 90.1), (× 64.0), (+ 45.25), ($*$ 32.0), (• 22.6); $q_{c,0} = (-1.00, -0.46, -0.22, -0.10)$.

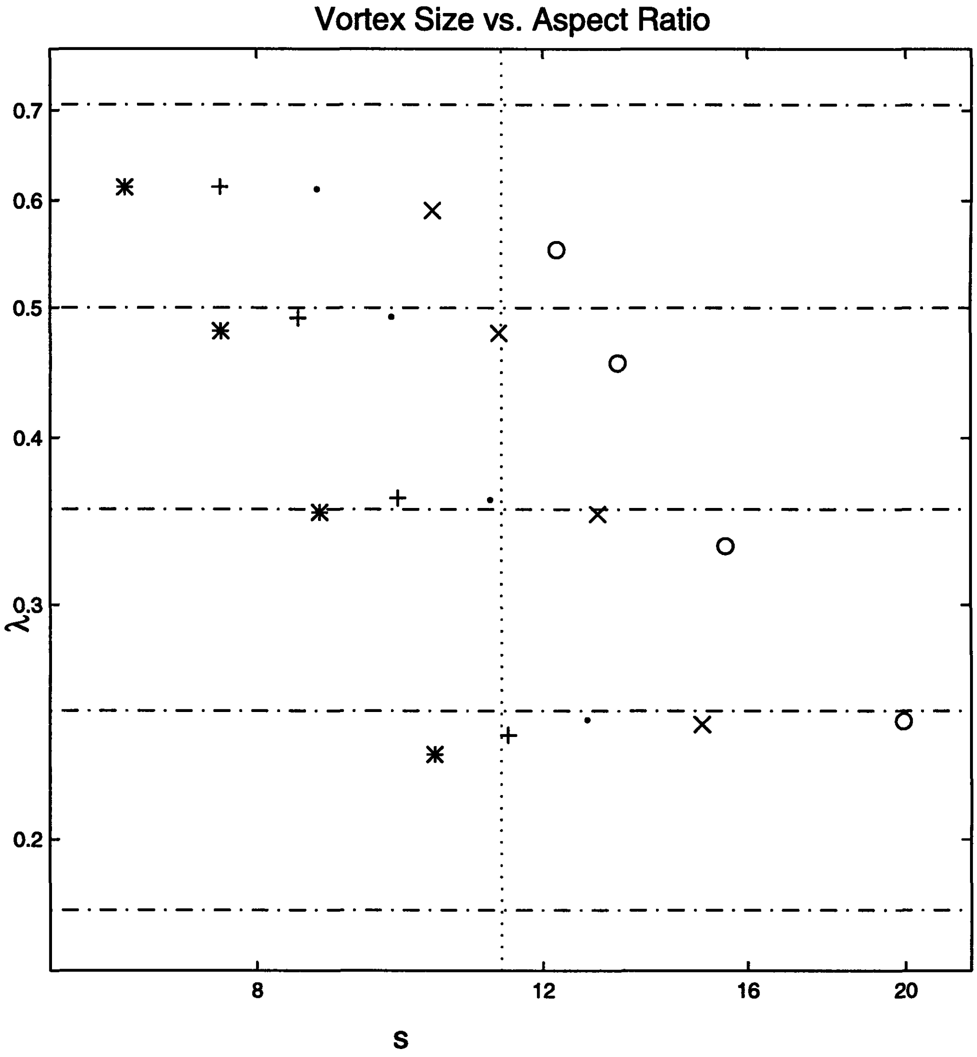

Figure 4-17: Size vs. aspect ratio; (symbol λ_0) pairs: ($\circ$ 0.71), ($\times$ 0.50), (+ 0.35), ($*$ 0.25), ($\bullet$ 0.18); $s_0 = 11.3$.

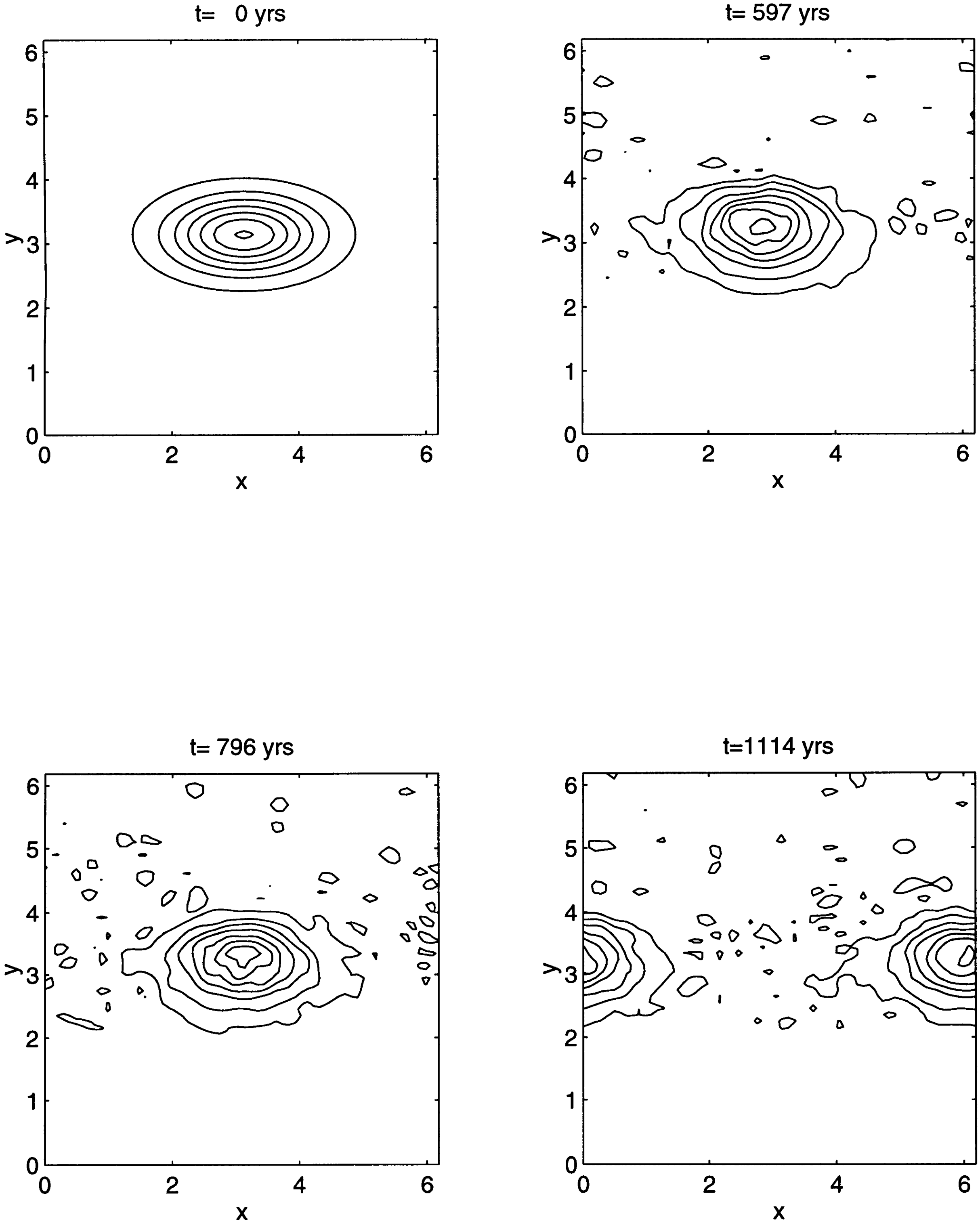
t= 0 yrs

t= 597 yrs

t= 796 yrs

t=1114 yrs

Figure 4-18: Robust vortex

4.3.4 Multiple Vortices

The behavior of multiple vortices is important because it helps show how the vortices may form. Specifically, calculations show that two negative vortices along the same longitude will merge to form one larger vortex in under ten orbit periods, as seen in Fig. 4-19. The merged vortex has a larger radial extent than either original vortex. Positive vortices inhibit merging, which is consistent with the findings of the behavior of single vortices.

Vortices which are separated radially do not tend to merge because the differential rotation of the disk moves them apart too quickly for them to interact. If the vortices start with the same angular center position, they will move apart with the angular separation becoming greater than the total width of the vortices in under one orbit period, as seen in Fig. 4-20.

4.3.5 Random Velocity Field

Calculations with a random vorticity field are performed to see how vortex formation may occur. This experiment is initialized with a vorticity energy spectrum proportional to the $-6th$ power of the wavenumber. While much of the vorticity remains distributed throughout the field, some becomes localized into a vortex, with an amplitude increase of more than 50% compared to the maximum initial vorticity amplitude in the field, as shown in Fig. 4-21. If the disk forms from a *turbulent* three-dimensional gas/dust cloud, the flow, when it becomes two-dimensional is quite likely to have considerable variability. This experiment (like those of Marcus in shears with constant vorticity [24]) demonstrates that larger, coherent vortices will emerge.

4.4 Model Tests

4.4.1 Courant-Friedrichs-Lewy Stability Criterion

The CFL criterion specifies the maximum time step which can be used in PDE calculations [8]. If disturbances propagate in the fluid with a maximum velocity U, then the time step must be small enough so that the disturbance cannot completely jump across a grid box in one time step. If this is not satisfied, then fluid characteristics can move across the region too quickly for the calculations to keep track of them. The CFL criterion therefore requires

$$h \leq c\frac{\Delta x}{U}, \tag{4.27}$$

where the constant c is a parameter of the integration scheme. For the RK4 scheme, $c \approx 2.6$ [8]. The speeds involved are dominated by the change in the Keplerian velocity across the region,

$$U = v_k(y = 0) - v_k(y = \pi), \tag{4.28}$$

and the grid spacing is smaller in y,

$$\Delta y = \frac{\pi}{L}, \tag{4.29}$$

where L is the number of grid points in the y direction. The time step must then be less than

$$h < \frac{9}{UL}. \tag{4.30}$$

This is in units of years. For $L = 128$ and $U \sim 2\pi$, the maximum timestep is approximately $h_{max} \sim 0.01$. In the calculations, timesteps larger than this result in rapid increase in numerical errors until the calculation returns invalid numbers. In general, most calculations of the vortex use a timestep of $h = 0.005$ or smaller, and numerical instabilities do not appear to be a factor.

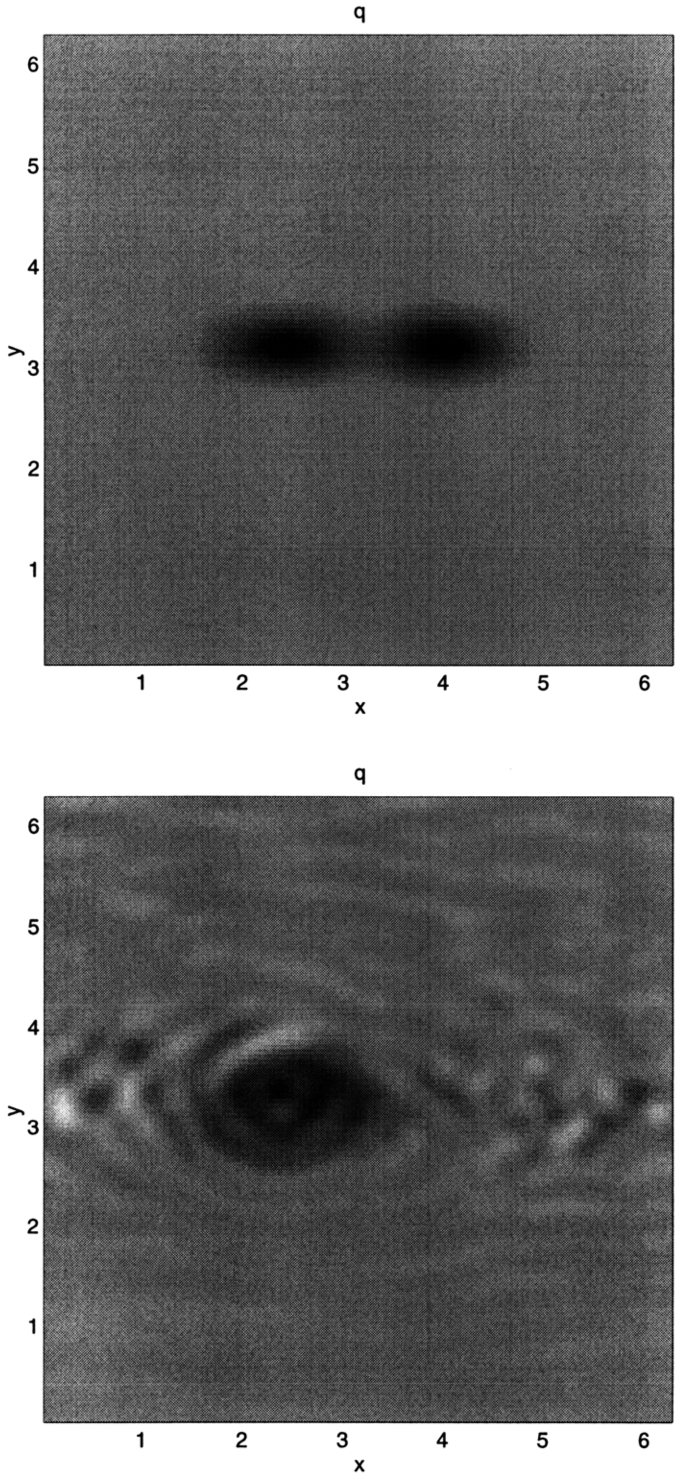

Figure 4-19: Two vortices merging; vorticity field at $t_0 = 0$, $t_f = 39.8\,\mathrm{yr}$

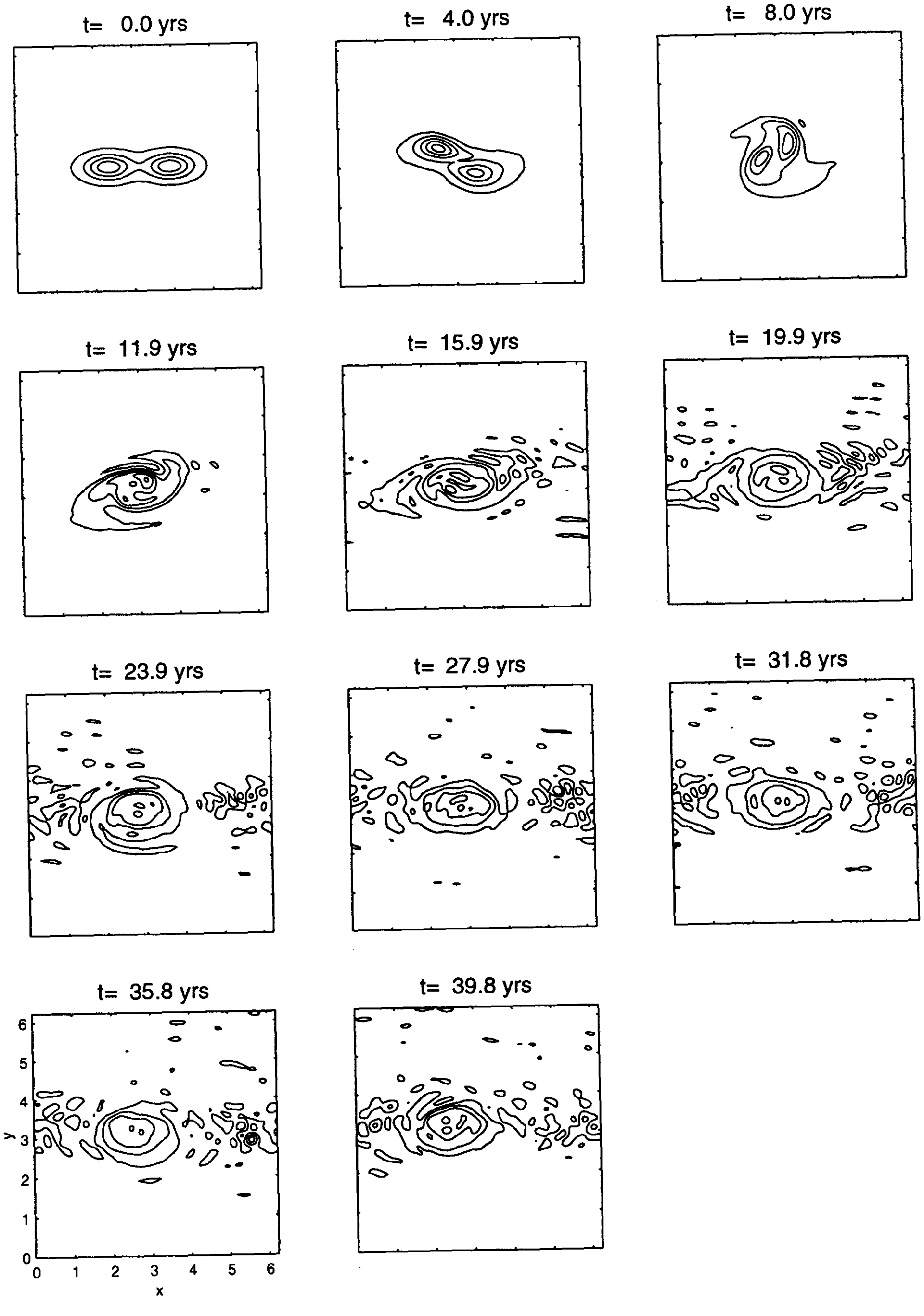

Figure 4-20: Two vortices merging

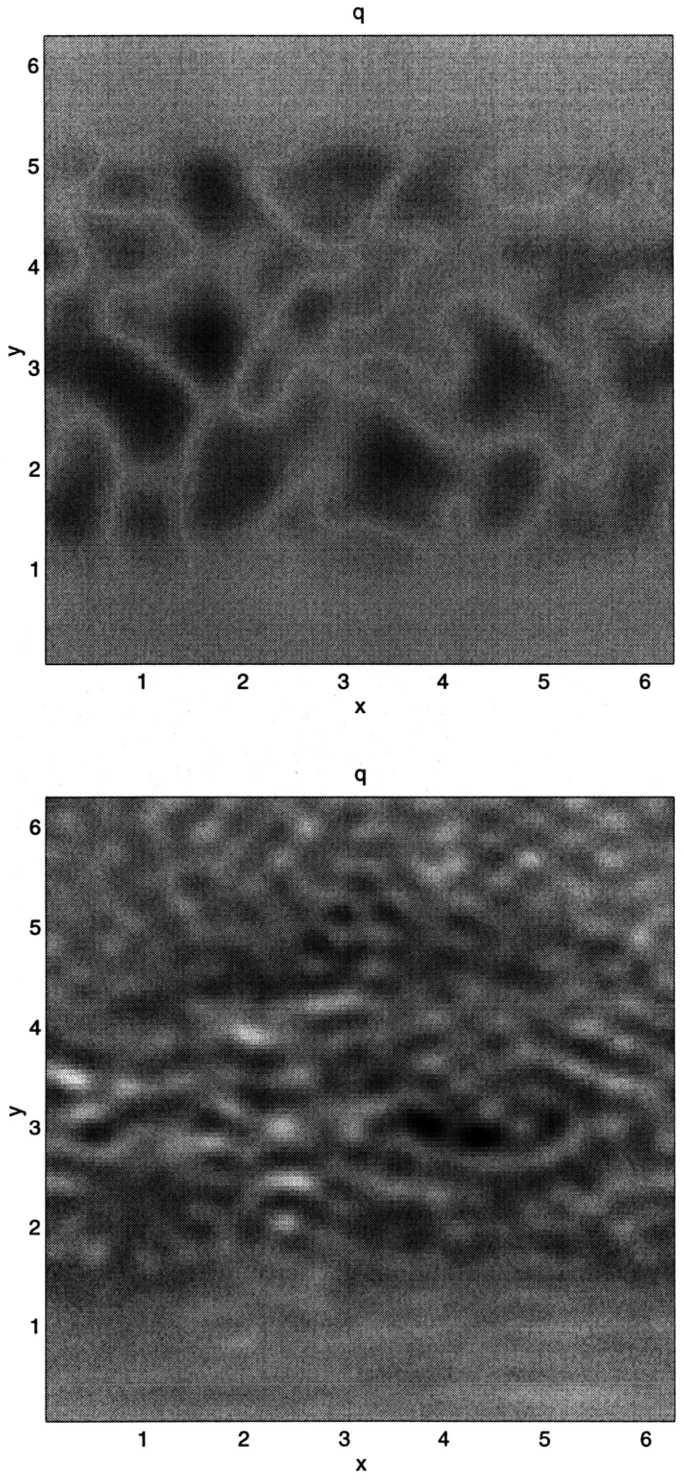

Figure 4-21: Random vorticity field at $t_0 = 0$, $t_f = 17.4\,\mathrm{yr}$

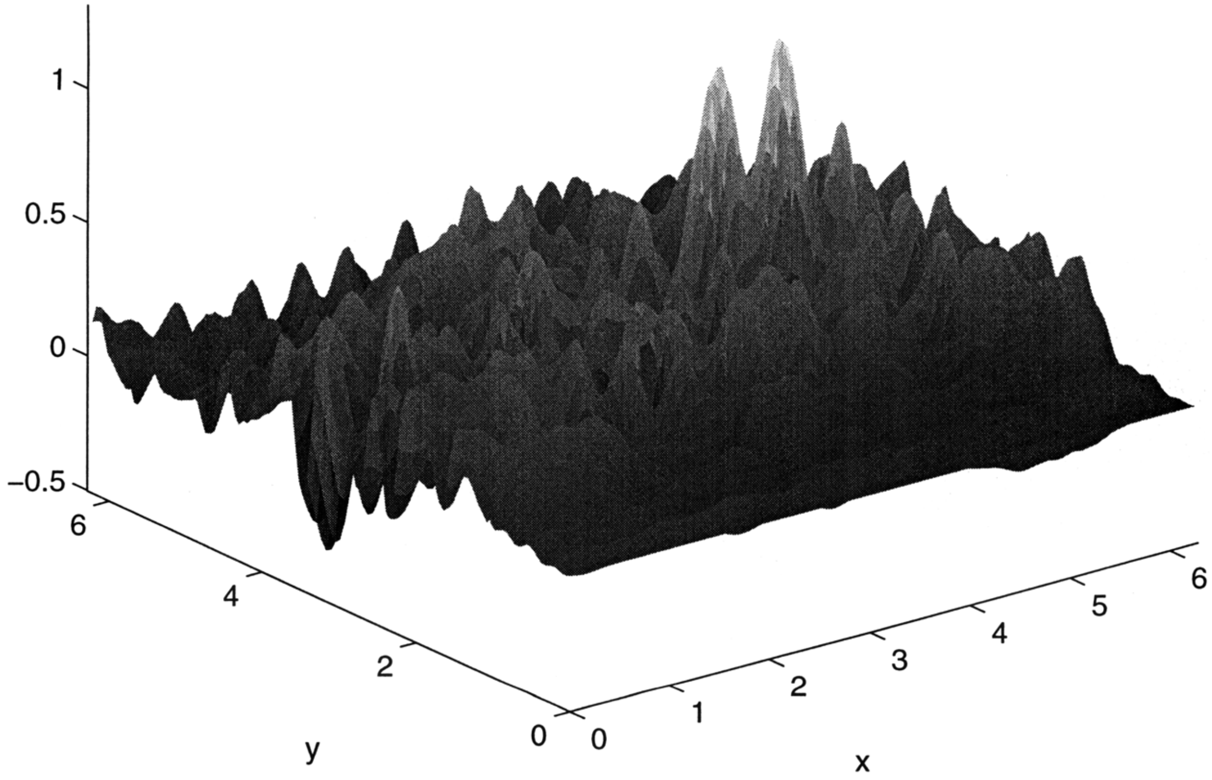

Figure 4-22: Random vorticity field at $t_f = 17.4\,\mathrm{yr}$

4.4.2 Grid Size

The effects of the grid size is tested by calculating the vortex evolution for the same vortex in the 64×64 and 128×128, with very small differences, as seen in Fig. 4-23.

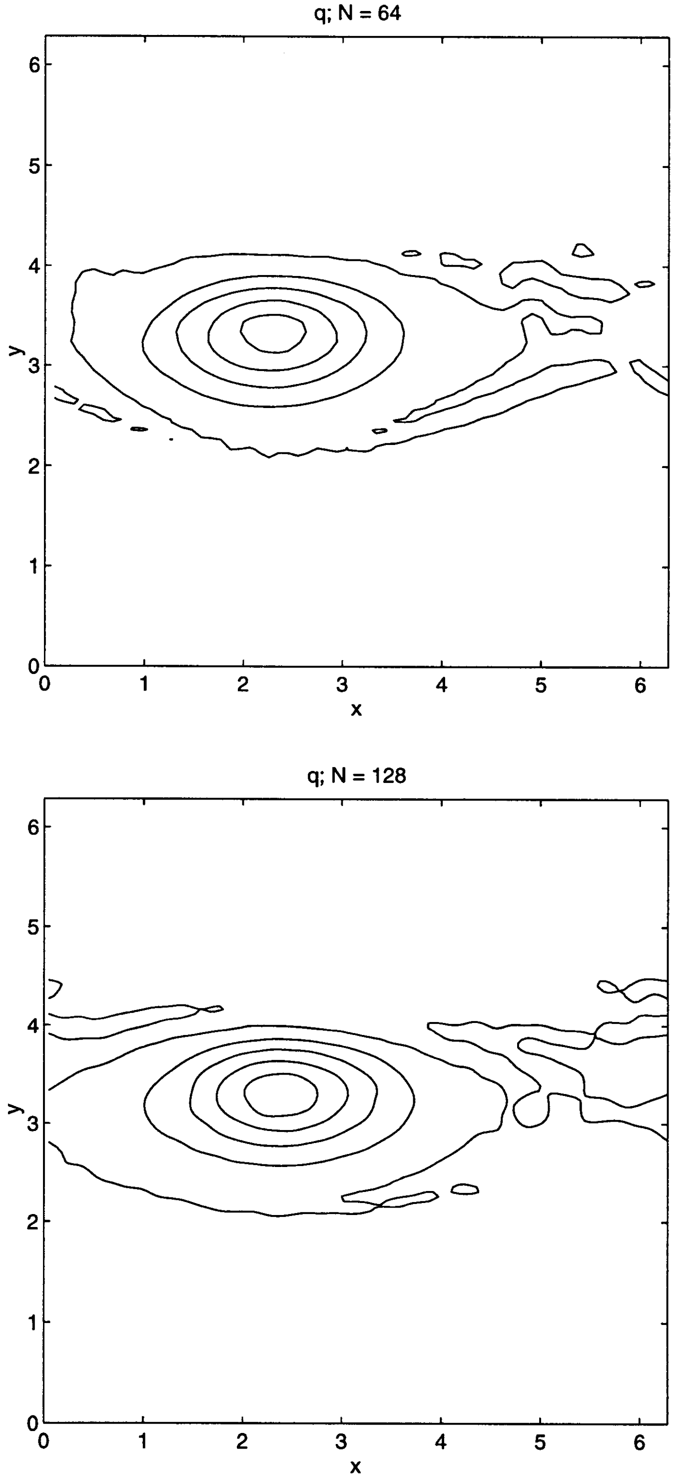

Figure 4-23: Grid size test

Chapter 5

Gas-Dust Interaction

In order for vortices to enhance the aggregation of dust particles into larger bodies, the dynamical effect of the gas on the suspended dust must be examined. This will be done in a series of steps, starting with a simple analytical calculation and progressing to a full calculation of particle trajectories in an evolving gas field.

The first calculation will look at an axisymmetric pressure band. This will demonstrate the convergence of particles into a high pressure band and the divergence out of a low pressure band, using orbital dynamics arguments. This will also allow the calculation of convergence times based on the dust-gas relaxation time and pressure band characteristics, especially the size and strength.

The second experiment will use an elliptical vortex patch orbiting the sun. Again, particle convergence times can be determined as a function of the dust-gas relaxation time and the vortex characteristics. This situation is also more realistic than the pressure band, since stability analysis shows that a strong axisymmetric disturbance cannot persist, but the non-axisymmetric vortex is not restricted.

To compute the particle trajectories suspended in the robust gas vortices, the gas velocity must be calculated at the location of the particle. The gas velocity is specified on a grid, so the value at points off the grid must be interpolated. To check the accuracy of trajectories, the elliptical vortex velocities are specified on the grid, and the dust trajectories are compared to the trajectories using the functional form of the gas velocity.

Particle trajectories are then calculated using the gas velocities from the robust vortex in annular coordinates. First, a single snapshot of the vortex is used, to isolate the effect of the gas. Finally, the gas field evolves concurrently with the dust trajectories.

The drift of particles can be explained using orbital dynamics arguments. In an elliptical orbit, the energy of the particle is proportional to the semi-major axis of the orbit. If the particle feels a drag from the gas which reduces its speed, it will slow down and lose energy. This will reduce the semi-major axis, so the particle will drift in towards the center. If, however, the gas is flowing faster than the particle, it will increase the speed of the particle, increasing its energy and semi-major axis, resulting in an outward drift.

5.1 Force on Dust Particle Suspended in Gas

As gas flows past a solid object, a boundary layer of the flow forms due to the molecular viscosity of the gas. Through this mechanism, the gas exerts a force on the object. This Stokes drag force depends on the gas viscosity, the object's geometry, and the object's velocity relative to the gas.

The force on the object can be calculated if a simple geometry is specified. For a solid sphere, the force is

$$\boldsymbol{F}_\eta = -6\pi\eta(\Delta/2)(\boldsymbol{u}_p - \boldsymbol{u}_g), \tag{5.1}$$

where η is the gas molecular viscosity, Δ is the sphere diameter, and $(\boldsymbol{u}_p, \boldsymbol{u}_g)$ are the particle and gas velocities. The acceleration is

$$\boldsymbol{a}_\eta = \frac{1}{m}\boldsymbol{F}_\eta = -\frac{1}{\tau_\eta}(\boldsymbol{u}_p - \boldsymbol{u}_g), \tag{5.2}$$

where τ_η is the relaxation time for the particle velocity to approach the gas velocity, given by

$$\tau_\eta = \frac{m}{3\pi\eta\Delta}. \tag{5.3}$$

For a solid sphere, with

$$m = \frac{1}{6}\pi\rho_p\Delta^3, \tag{5.4}$$

the relaxation time is

$$\tau_\eta = \frac{\rho_p\Delta^2}{18\eta}. \tag{5.5}$$

The dynamics of the interaction between the gas and dust are completely specified by τ_η, so the specific particle characteristics can be determined separately. For the dust in the solar nebula, both the exact shape and the packing density can vary for the same value of τ_η.

5.2 Dust Particle Equations of Motion

The equation of motion for the dust particle is

$$\begin{aligned} \ddot{\boldsymbol{r}}_p &= \boldsymbol{g} + \boldsymbol{a}_\eta & \text{(5.6.a)} \\ &= \boldsymbol{g} - \frac{1}{\tau_\eta}(\boldsymbol{u}_p - \boldsymbol{u}_g). & \text{(5.6.b)} \end{aligned}$$

This will be used in polar coordinates, annular coordinates, and the cartesian coordinate limit of the annular coordinate equations.

The gravity, velocity, and angular velocity are

$$\begin{aligned} k_k &\equiv \sqrt{GM_\odot} = 2\pi\,\mathrm{AU}^{3/2}\,\mathrm{yr}^{-2}, & \text{(5.7.a)} \\ \boldsymbol{g} &= -\hat{\boldsymbol{r}}k_k^2 r^{-2}, & \text{(5.7.b)} \\ v_k &= k_k r^{-1/2}, & \text{(5.7.c)} \\ \Omega_k &= k_k r^{-3/2}, & \text{(5.7.d)} \end{aligned}$$

and they are related by eliminating k_k,

$$g = \frac{1}{r}v_k^2 = r\Omega_k. \tag{5.8}$$

The equations may be expressed in a rotating coordinate frame, as described in §A.2.3. With the rotation rate

$$\begin{aligned} \boldsymbol{\Omega} &= \hat{\boldsymbol{z}}\Omega_c, & (5.9.a) \\ \Omega_c &= k r_c^{-3/2}, & (5.9.b) \end{aligned}$$

the velocity and acceleration vectors are

$$\begin{aligned} \dot{\boldsymbol{r}}' &= \dot{\boldsymbol{r}} + \boldsymbol{\Omega} \times \boldsymbol{r}, & (5.10.a) \\ \ddot{\boldsymbol{r}}' &= \ddot{\boldsymbol{r}} + 2\boldsymbol{\Omega}\times\dot{\boldsymbol{r}} + \boldsymbol{\Omega} \times (\boldsymbol{\Omega} \times \boldsymbol{r}), & (5.10.b) \end{aligned}$$

with $\boldsymbol{\Omega}$ constant. The equation of motion for a two-dimensional trajectory is then

$$\ddot{\boldsymbol{r}} + 2\Omega_c\hat{\boldsymbol{z}}\times\dot{\boldsymbol{r}} - \Omega_c^2\boldsymbol{r} = \boldsymbol{g} - \frac{1}{\tau_\eta}(\dot{\boldsymbol{r}} - \dot{\boldsymbol{r}}_g). \quad (5.11)$$

The Keplerian velocity, streamfunction, and vorticity are given by Eq. A.39. The gravitational acceleration is

$$g = \frac{r_c^3}{r^2}\Omega_c^2. \quad (5.12)$$

The gravitation and centripetal acceleration terms from Eq. 5.11 give

$$\boldsymbol{g} + \Omega_c^2\boldsymbol{r} = \boldsymbol{r}\Omega_c^2\left[1 - \left(\frac{r_c}{r}\right)^3\right]. \quad (5.13)$$

5.2.1 Non-Rotating, Cylindrical Coordinates

The equations of motion in cylindrical coordinates are

$$\begin{aligned} \boldsymbol{r} &= r\hat{\boldsymbol{r}}, & (5.14.a) \\ \dot{\boldsymbol{r}} &= u\hat{\boldsymbol{r}} + v\hat{\boldsymbol{\theta}}, & (5.14.b) \\ \ddot{\boldsymbol{r}} &= \hat{\boldsymbol{r}}\left(\dot{u} - \frac{1}{r}v^2\right) + \hat{\boldsymbol{\theta}}\left(\dot{v} + \frac{1}{r}uv\right). & (5.14.c) \end{aligned}$$

with the radial and angular velocities (u, v), defined as

$$\begin{aligned} u &\equiv \dot{r}, & (5.15.a) \\ v &\equiv r\dot{\theta}. & (5.15.b) \end{aligned}$$

Combining this with Eqs. 5.6 and 5.7 gives

$$\hat{\boldsymbol{r}}\left(\dot{u} - \frac{1}{r}v^2\right) + \hat{\boldsymbol{\theta}}\left(\dot{v} + \frac{1}{r}uv\right) = -\hat{\boldsymbol{r}}k^2r^{-2} - \frac{1}{\tau_\eta}[\hat{\boldsymbol{r}}(u - u_g) + \hat{\boldsymbol{\theta}}(v - v_g)], \quad (5.16)$$

which gives the system of equations

$$\begin{aligned} \dot{r} &= u, & (5.17.a) \\ \dot{\theta} &= \frac{1}{r}v, & (5.17.b) \\ \dot{u} &= +\frac{1}{r}v^2 - \frac{1}{\tau_\eta}(u - u_g) - \frac{1}{r}v_k^2, & (5.17.c) \\ \dot{v} &= -\frac{1}{r}uv - \frac{1}{\tau_\eta}(v - v_g). & (5.17.d) \end{aligned}$$

The gas velocity, $\boldsymbol{v}_g$ is be specified by the pressure band in §5.3.

5.2.2 Rotating, Annular Coordinates

To calculate the trajectories of particles suspended in the robust gas vortex, the equations of motion are needed in annular coordinates in a rotating reference frame. As described in §A.3, annular coordinates description uses

$$\begin{aligned} R &\equiv \frac{r_0}{M}, && \text{(5.18.a)} \\ Y &\equiv e^{y/M}. && \text{(5.18.b)} \end{aligned}$$

The position, velocity, and acceleration vectors are

$$\begin{aligned} \boldsymbol{r} &= \hat{\boldsymbol{y}} MRY, && \text{(5.19.a)} \\ \dot{\boldsymbol{r}} &= u\hat{\boldsymbol{x}} + v\hat{\boldsymbol{y}}, && \text{(5.19.b)} \\ \ddot{\boldsymbol{r}} &= \hat{\boldsymbol{x}}\left(\dot{u} + \frac{1}{r}uv\right) + \hat{\boldsymbol{y}}\left(\dot{v} - \frac{1}{r}u^2\right), && \text{(5.19.c)} \end{aligned}$$

with

$$\begin{aligned} u &\equiv RY\dot{x}, && \text{(5.20.a)} \\ v &\equiv RY\dot{y}. && \text{(5.20.b)} \end{aligned}$$

The equation of motion in annular coordinates, using Eqs. 5.11 and 5.13 for the rotating frame, gives

$$\ddot{\boldsymbol{r}} = 2\Omega_c(\hat{\boldsymbol{x}}v - \hat{\boldsymbol{y}}u) - \frac{1}{\tau_\eta}[\hat{\boldsymbol{x}}(u - u_g) + \hat{\boldsymbol{y}}(v - v_g)] + \hat{\boldsymbol{y}} MRY\Omega_c^2\left[1 - \left(\frac{Y_c}{Y}\right)^3\right]. \tag{5.21}$$

The background velocity, $\hat{\boldsymbol{x}}\bar{u}$, can be subtracted from the total velocity $\boldsymbol{u}$,

$$\boldsymbol{u} = \hat{\boldsymbol{x}}(\bar{u} + u') + \hat{\boldsymbol{y}}v', \tag{5.22}$$

with

$$\bar{u} = -MRY\Omega_c\left[1 - \left(\frac{Y_c}{Y}\right)^{3/2}\right]. \tag{5.23}$$

The following terms cancel from the equations:

$$\begin{aligned} \dot{\bar{u}} &= 0, && \text{(5.24.a)} \\ \frac{1}{r}\bar{u}^2 - 2\Omega_c\bar{u} + r\Omega_c^2 - g &= 0. && \text{(5.24.b)} \end{aligned}$$

This gives the system of equations,

$$\begin{aligned} \dot{x} &= \frac{1}{RY}(u' + \bar{u}), && \text{(5.25.a)} \\ \dot{y} &= \frac{1}{RY}v', && \text{(5.25.b)} \\ \dot{u}' &= -\frac{1}{MRY}(u' + \bar{u})v' + 2\Omega_c v' - \frac{1}{\tau_\eta}(u' - u_g'), && \text{(5.25.c)} \\ \dot{v}' &= \frac{1}{MRY}(u'^2 + 2u'\bar{u}) - 2\Omega_c u' - \frac{1}{\tau_\eta}(v' - v_g'). && \text{(5.25.d)} \end{aligned}$$

5.2.3 Rotating, Cartesian Coordinate Limit

From the annular coordinate system equations, the cartesian coordinate limit can be taken, as described in §A.3.5. This is reached by setting $R = 1$, taking the limit

$$Y = e^{y/M} \approx 1 + \frac{y}{M}, \tag{5.26}$$

and then taking the limit

$$\left(r_0, \frac{1}{M}\right) \to 0. \tag{5.27}$$

The gravity and centripetal acceleration terms (Eq. 5.13) in the annular form of Eq. 5.21 become

$$MRY\Omega_c^2 \left[1 - \left(\frac{Y_c}{Y}\right)^3\right] \approx 3\Omega_c^2(y - y_c). \tag{5.28}$$

The Keplerian velocity term, from Eq. 5.23, becomes

$$\bar{u} \approx -\frac{3}{2}\Omega_c(y - y_c). \tag{5.29}$$

This has a constant shear, and the vorticity is

$$\bar{q} = -\tfrac{3}{2}\Omega_c. \tag{5.30}$$

The u^2/r and uv/r terms in the equation of motion go to zero in the limit of large M, and the $1/Y$ terms approach unity, so the equations of motion are

$$\begin{aligned}
\dot{x} &= u' - \frac{3}{2}\Omega_c(y - y_c), && (5.31.a)\\
\dot{y} &= v', && (5.31.b)\\
\dot{u}' &= +2\Omega_c v' - \frac{1}{\tau_\eta}(u' - u_g'), && (5.31.c)\\
\dot{v}' &= -2\Omega_c v' - \frac{1}{\tau_\eta}(v' - v_g') + 3\Omega_c^2(y - y_c). && (5.31.d)
\end{aligned}$$

These can be integrated with a specified gas velocity field.

5.3 Axisymmetric Pressure Band

To gain a physical understanding of the effects of the gas flow on a dust particle, an examiniation of the axisymmetric analog of a vortex, a pressure band, is instructive. Both are high or low pressure regions with velocity perturbations resulting in a measureable vorticity. The pressure band does not completely eliminate angular considerations—the velocity perturbation is a change in the angular Keplerian velocity—but some angular and radial terms are dropped. The number of parameters which affect the dust particle trajectories are also fewer than for the two-dimensional vortex. The simpler system permits a better physical understanding of the effect of the gas, as well as some scaling laws for the convergence of particles into the band or vortex.

5.3.1 Gas Perturbation Velocity Equations

Starting with the general Navier-Stokes equation (NSE), the axisymmetric form is derived. Then, with the gravity and Keplerian velocity terms for a central star, the dependence of the steady-state velocity perturbation on the pressure gradient is calculated. This will be used to look at the effects of the pressure gradient in two cases—the solar nebula disk and a pressure band.

Euler's equation is

$$\frac{\partial \boldsymbol{u}}{\partial t} + (\boldsymbol{u} \cdot \boldsymbol{\nabla})\boldsymbol{u} = -\frac{1}{\rho}\boldsymbol{\nabla} p + \boldsymbol{g} - \frac{1}{\rho}\boldsymbol{f}_\eta, \tag{5.32}$$

where the drag force of the particles on the gas, $\boldsymbol{f}_\eta$, is negligible. In polar coordinates, the velocity vector is

$$\boldsymbol{u} \equiv \hat{\boldsymbol{r}} u + \hat{\boldsymbol{\theta}} v, \tag{5.33}$$

and the gravity term is given by Eqs. 5.7 and 5.12. The NSE becomes

$$u_t + \left(u\frac{\partial u}{\partial r} + \frac{1}{r}v\frac{\partial u}{\partial \theta} - \frac{1}{r}v^2\right) = \frac{1}{\rho}\frac{\partial p}{\partial r} - \frac{1}{r}v_k^2, \tag{5.34.a}$$

$$v_t + \left(u\frac{\partial v}{\partial r} + \frac{1}{r}v\frac{\partial v}{\partial \theta} + \frac{1}{r}uv\right) = \frac{1}{\rho}\frac{\partial p}{\partial \theta}. \tag{5.34.b}$$

For the axisymmetric band, assume that the velocity and pressure components are independent of angle, so

$$\frac{\partial u}{\partial \theta} = \frac{\partial v}{\partial \theta} = \frac{\partial p}{\partial \theta} = 0. \tag{5.35}$$

The steady state solution for the flow is found by setting the time derivative of the NSE to zero. The angular component of the NSE is

$$u\frac{\partial v}{\partial r} + \frac{1}{r}uv = 0. \tag{5.36}$$

The Keplerian velocity does not satisfy this equation, so the remaining solution is

$$u = 0. \tag{5.37}$$

The radial component of the NSE then gives

$$v^2 = v_k^2 + \frac{r}{\rho}\frac{\partial p}{\partial r} \tag{5.38.a}$$

$$= v_k^2[1 + 2\Pi(r)], \tag{5.38.b}$$

with

$$\Pi(r) \equiv \frac{r}{2v_k^2\rho}\frac{\partial p}{\partial r}. \tag{5.39}$$

The angular velocity can be separated into the Keplerian and perturbation terms,

$$v = v_k + v_g'. \tag{5.40}$$

The velocity perturbation is

$$v_g' = v_k\left[(1 + 2\Pi)^{1/2} - 1\right] \tag{5.41.a}$$

$$\approx v_k\Pi, \tag{5.41.b}$$

where the approximation assumes that the pressure term is small, $\Pi \ll 1$.

The velocity perturbations can be combined with the dust equations of motion. By first separating the Keplerian and the perturbation velocities for the dust, Eq. 5.17 becomes

$$\begin{aligned} \dot{r} &= u', &\quad (5.42.a) \\ \dot{\theta} &= \frac{v_k}{r}\left(1+\frac{v'}{v_k}\right), &\quad (5.42.b) \\ \dot{u}' &= \frac{v_k}{r}\left(2+\frac{v'}{v_k}\right)v' - \frac{1}{\tau_\eta}u', &\quad (5.42.c) \\ \dot{v}' &= -\frac{v_k}{r}\left(1+\frac{v'}{v_k}\right)u' - \frac{1}{\tau_\eta}(v'-v_g'). &\quad (5.42.d) \end{aligned}$$

The orbital period, T_0, is related to the Keplerian velocity and the angular velocity by

$$\frac{v_k}{r} = \Omega_k = \frac{2\pi}{T_0}, \tag{5.43}$$

and the relaxation parameter is defined as

$$\alpha = \frac{T_0}{\tau_\eta}. \tag{5.44}$$

In the limit where the perturbations are all smaller than the Keplerian velocity, the velocity equations simplify to

$$\begin{aligned} T_0\,\dot{u}' - 4\pi v' + \alpha u' &= 0, &\quad (5.45.a) \\ T_0\,\dot{v}' + 2\pi u' + \alpha v' &= \alpha v_g'. &\quad (5.45.b) \end{aligned}$$

This is a system of coupled, first order, inhomogeneous differential equations. Some insight can be gained from consideration of the case where the gas velocity is uniform, $v_g' = V_g$, and constant in time. The solutions have the form

$$\begin{aligned} u' &= A_+ e^{s_+ t} + A_- e^{s_- t} + u_c, &\quad (5.46.a) \\ v' &= A_+ e^{s_+ t} + B_- e^{s_- t} + v_c. &\quad (5.46.b) \end{aligned}$$

The exponential terms are the homogeneous solution, describing the transients to the steady state. The constants are the inhomogeneous solution, giving the steady state values. The constant terms are related to the gas velocity by

$$\begin{aligned} u_c &= \frac{4\pi\alpha}{8\pi^2+\alpha^2}V_g, &\quad (5.47.a) \\ v_c &= \frac{\alpha^2}{8\pi^2+\alpha^2}V_g. &\quad (5.47.b) \end{aligned}$$

The exponential terms describe the damped oscillations, with

$$s_\pm = \frac{1}{T_0}(-\alpha \pm i2\sqrt{2\pi}). \tag{5.48}$$

The damping is determined by α, while the oscillation frequency is related to the orbital period. The coefficients are related by

$$\begin{aligned} B_{\pm} &= A_{\pm}\left(\frac{T_0 s_{\pm}+\alpha}{4\pi}\right) \\ &= \pm\frac{1}{\sqrt{2\pi}}A_{\pm}e^{i\pi/2}. \end{aligned} \tag{5.49.a}$$

The coefficients for the radial velocity, $B_{\pm}$, are out of phase with the coefficients for the angular velocity, $A_{\pm}$. The homogeneous term coefficients, $A_{\pm}$, can be determined by specifying the initial velocity values, $(u'(0), v'(0))$.

The particles can be grouped into three categories: strongly coupled, weakly coupled, and uncoupled with the gas, based on the ratio of the coupling and dynamical timescales. The strongly coupled particles have $\tau_\eta \ll T_0$, so the particle velocity quickly relaxes to the gas flow, limiting the drift force. These tend to be the smallest and fluffiest particles. If the particle is perturbed (probably through collisions), so that its velocity is different from the gas velocity, the coupling terms will dominate and quickly equilibrate the particle and gas velocities before the cross velocities in the dynamical terms can cause a drift.

In the uncoupled case, with $\tau_\eta \gg T_0$, the dynamical terms dominate over the coupling terms, so the effect of the gas is too small to influence the motion. If a particle starts with no perturbation, and the gas perturbation is negative, then the angular acceleration will have a small, negative value. This will cause a small, radially inward acceleration. A small, negative radial velocity will cancel a larger gas perturbation in the angular acceleration equation, reaching an equilibrium where the particle perturbations are smaller than the gas perturbation by order T_0/τ_η, which has been assumed to be small. Since the gas perturbation is already smaller than the Keplerian velocity, the particle perturbations are negligible.

In the weakly coupled case, with $\tau_\eta \sim T_0$, an appreciable drift can result. The angular perturbation will approach but not equal the gas perturbation, as the radial perturbation will offset the difference. A steady state can be found, with the radial and angular accelerations set to zero. By first defining the relaxation parameter,

$$\alpha = \frac{T_0}{2\pi\tau_\eta}, \tag{5.50}$$

the simple system of equations is obtained,

$$2v' - \alpha u' = 0, \tag{5.51.a}$$

$$u' + \alpha v' = \alpha v'_g. \tag{5.51.b}$$

This has the solution

$$u' = \frac{2\alpha}{2+\alpha^2}\, v'_g, \tag{5.52.a}$$

$$v' = \frac{\alpha^2}{2+\alpha^2}\, v'_g, \tag{5.52.b}$$

like that for a constant gas velocity, as plotted in Fig. 5-1. The maximum radial velocity is obtained with $\alpha = 1/\sqrt{2}$, so the relaxation time is

$$\tau_\eta = \frac{T_0}{\pi\sqrt{2}} \approx 0.23\ T_0, \tag{5.53}$$

and the velocity perturbations are $u'_{max} = v'_g/\sqrt{2}$ and $v'_{max} = v'_g/2$.

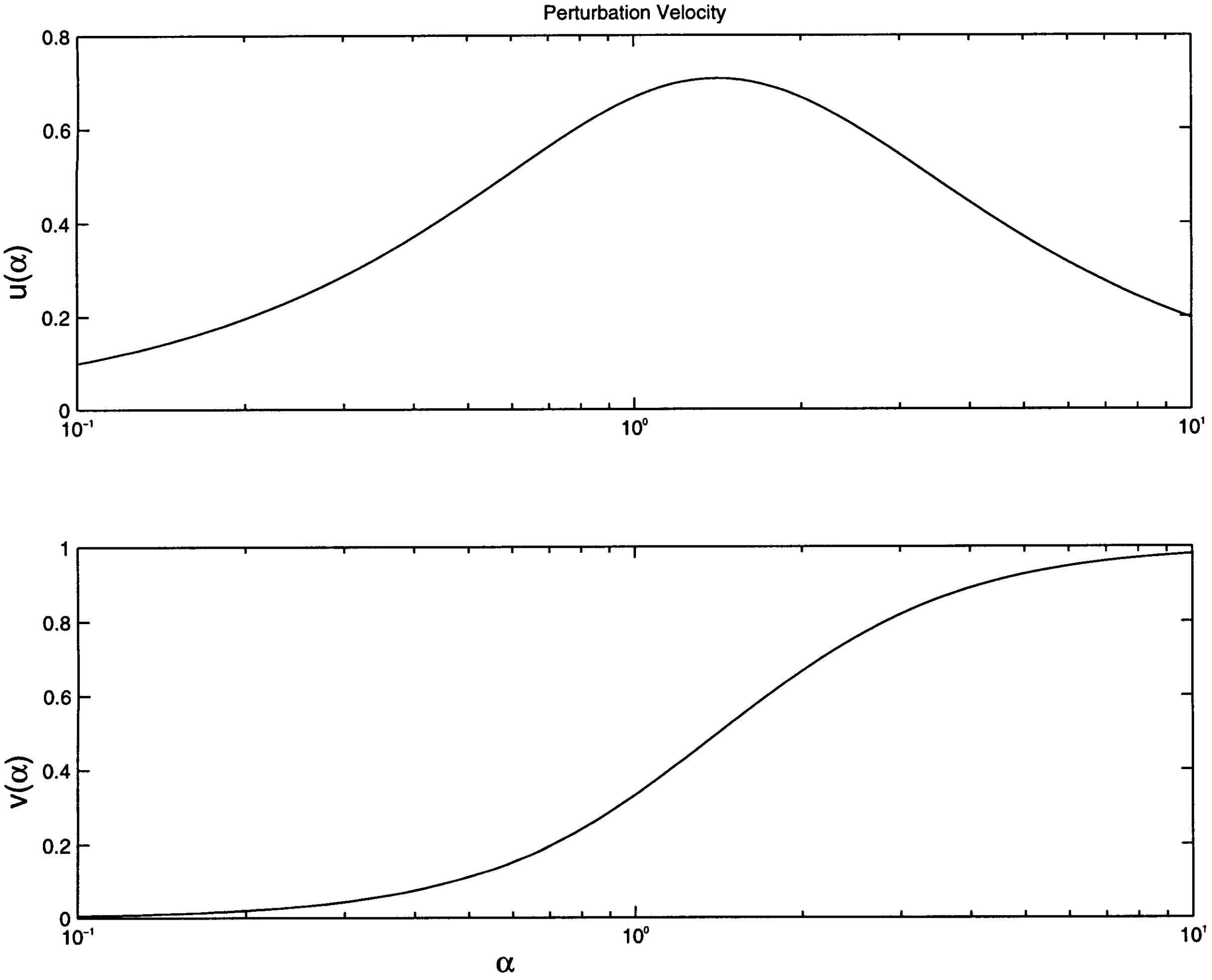

Figure 5-1: Particle perturbation velocity, (u, v) vs. $\log(\alpha)$

5.3.2 Velocity Perturbations in the Steady State Solar Nebula

The solar nebula disk has a pressure gradient which results in a small velocity perturbation relative to the Keplerian velocity. If the pressure in the nebula obeys a power law, then the velocity perturbation is inversely proportional to the square of the Mach number of the Keplerian velocity.

The pressure, density, temperature, and sound speed are related (see §2.1.2),

$$c_s^2 = \gamma\left(\frac{k_B T}{m_H \mu_0}\right) \tag{5.54.a}$$

$$= \gamma\left(\frac{p}{\rho}\right). \tag{5.54.b}$$

With the pressure given by

$$p(r) = P_0\left(\frac{r}{r_c}\right)^{I_p}, \tag{5.55}$$

the gradient is

$$\frac{\partial p}{\partial r} = \frac{I_p}{r}p(r), \tag{5.56}$$

and the perturbation term, using Eq. 5.39, is

$$\Pi(r) = \frac{I_p c_s^2}{2\gamma v_k^2} = \frac{I_p}{2\gamma M_k^2}. \tag{5.57}$$

For the solar nebula, the pressure index is about two, the Mach number is of order 10–30, so the perturbation is of order 10^{-3} times the Keplerian velocity.

5.3.3 Pressure Band Velocity Perturbation

A pressure band results in a velocity perturbation which affects the particle motions. To be able to translate these results to a vortex, the vorticity of the pressure band will be calculated. The gas flow perturbation, combined with the equation of motion in cylindrical coordinates, gives the system of equations to be studied. Both analytical estimates and more numerical calculations can be performed using these equations.

The total vorticity is the sum of the Keplerian and the perturbation vorticities. Each term is the curl of the corresponding velocity term. The perturbation velocity, and therefore the perturbation vorticity, depends on the pressure gradient of the band. A non-dimensional measure of the band vorticity can be calculated by taking the ratio of the perturbation and Keplerian terms. This gives a relationship between the pressure amplitude and vorticity strength of the band. While this has a radial dependence, a comparison can be made to vortices by calculating the strength at the center of the band. This will include various band parameters, including the width, position, and pressure amplitude.

The vorticity and velocity are related in cylindrical coordinates by

$$q = \frac{1}{r}\frac{\partial(rv)}{\partial r}. \tag{5.58}$$

Separating the Keplerian and perturbation velocities, and using the approximation for the perturbation, Eq. 5.41.b, the components of the vorticity are

$$\begin{aligned} q_k &= \frac{1}{r}\frac{\partial(r v_k)}{\partial r} = \tfrac{1}{2}\frac{v_k}{r}, && (5.59.a) \\ q' &= \frac{1}{r}\frac{\partial(r v_k \Pi)}{\partial r} = v_k\frac{\partial \Pi}{\partial r} + \tfrac{1}{2}\frac{v_k}{r}\Pi, && (5.59.b) \end{aligned}$$

and the non-dimensional vorticity strength is

$$\epsilon = \frac{q'}{q_k} = \Pi + 2r\frac{\partial \Pi}{\partial r}. \tag{5.60}$$

The pressure band can be described by a Gaussian radial pressure distribution, in addition to the disk pressure (see Fig. 5-2). The radial derivatives can be calculated easily, giving expressions for the perturbation velocity, vorticity, and band strength. Then the band strength can be used to eliminate the thermodynamic terms (pressure and density) in the velocity perturbation, giving the velocity field as a function of the band strength. In addition, the change in pressure and temperature can be calculated.

The pressure function and the radial derivative are

$$\begin{aligned} p(r) &= P_c e^{-(r-r_c)^2/\sigma^2}, && (5.61.a) \\ \frac{\partial p}{\partial r} &= -2\left(\frac{r-r_c}{\sigma^2}\right)p(r). && (5.61.b) \end{aligned}$$

Using this in Eq. 5.39 for Π gives

$$\begin{aligned} \Pi(r) &= -\frac{r}{v_k^2}\left(\frac{r-r_c}{\sigma^2}\right)\frac{p}{\rho}, && (5.62.a) \\ \frac{\partial \Pi}{\partial r} &= -\frac{p}{k^2\rho}\left[\frac{r^2}{\sigma^2} + 2r\left(\frac{r-r_c}{\sigma^2}\right) - 2r^2\left(\frac{r-r_c}{\sigma^2}\right)^2\right]. && (5.62.b) \end{aligned}$$

At the center of the band, with $r = r_c$ and $p(r_c) = P$, these terms become

$$\begin{aligned} \Pi(r_c) &= 0, && (5.63.a) \\ \frac{\partial \Pi}{\partial r}(r_c) &= -\frac{r_c P_c}{\sigma^2 v_{k,c}^2\, \rho}. && (5.63.b) \end{aligned}$$

The band strength is then

$$\epsilon = -2\frac{r_c^2}{\sigma^2}\frac{P_c}{v_{k,c}^2\, \rho}, \tag{5.64}$$

where $v_{k,c} = k r_c^{-1/2}$ is the Keplerian velocity at the center of the band. The band strength is negative, indicating that the vorticities of the Keplerian flow and the perturbation are in opposite directions for a high pressure band and a positive pressure amplitude ($P > 0$). For a low pressure band, with negative pressure amplitude, the band strength is positive. The stable vortex flow exists when the perturbation vorticity is negative, which corresponds to the high pressure band.

The length terms can be scaled by the position of the center of the band, so

$$y \equiv \frac{r}{r_c}, \tag{5.65.a}$$

$$s \equiv \frac{\sigma}{r_c}, \tag{5.65.b}$$

and the pressure, perturbation, and band strength become

$$p(y) = P_c e^{-(y-1)^2/s^2}, \tag{5.66.a}$$

$$\Pi(y) = -\frac{y(y-1)}{s^2}\frac{p(y)}{v_k^2 \rho}, \tag{5.66.b}$$

$$\epsilon = -2\frac{1}{s^2}\frac{P_c}{v_{k,c}\,\rho}. \tag{5.66.c}$$

Using the band strength with the pressure perturbation term, the ratio

$$\frac{v_k}{v_{k,c}} = \frac{kr^{-1/2}}{kr_c^{-1/2}} = y^{-1/2}, \tag{5.67}$$

gives

$$\Pi(y; s, \epsilon) = \tfrac{1}{2}\,\epsilon\, y^{3/2}\,(y-1)e^{-(y-1)^2/s^2}, \tag{5.68}$$

as plotted in Fig. 5-2.

First examine the case of the high pressure band, so the band strength is negative. For the gas radially in from the center of the band, the perturbation is positive ($\Pi(y < 1) > 0$), so the gas is moving faster than the Keplerian velocity. The dust particles will be accelerated, resulting in an outward drift, toward the center of the band. For the gas radially out from the center of the band, the perturbation is negative and the gas is moving slower than the Keplerian velocity. The dust particles will be decelerated, resulting in an inward drift, again towards the center of the band. Therefore, particles will tend to converge into the high pressure band, and it will be useful to estimate the convergence timescales. For a low pressure band, the sign of the perturbations are reversed, and particles will drift out of the band.

The thermodynamic properties of the band can be calculated using the equations from §5.3.2. Writing the band strength as a function of the change in the gas temperature at the center of the band,

$$\epsilon = -2\frac{r_c^2}{\sigma^2}\frac{1}{v_{k,c}^2}\left(\frac{k_B T_{c0}}{m_H \mu_0}\right)\frac{\Delta T_c}{T_{c0}}, \tag{5.69}$$

so the change in temperature is

$$\frac{\Delta T_c}{T_{c0}} = -\tfrac{1}{2}\,\epsilon\, s^2 M_{k,c}^2, \tag{5.70}$$

with negative ϵ for a positive pressure perturbation. For the temperature change to be small compared to the ambient disk temperature, the band strength and width are limited, compared to the Mach number. For example, with $M_{k,c} \approx 30$, $s = 0.05$, and $\epsilon = -0.1$, the temperature change is approximately 10% of the disk temperature.

The dust particle equations of motion, Eq. 5.42, can be solved numerically with the gas velocity, given by Eq. 5.41.a, and the perturbation parameter, given by Eq. 5.68.

In addition, making the approximation that the perturbation is small, the convergence time for particles to drift into the band can be estimated. The gas velocity perturbation is given

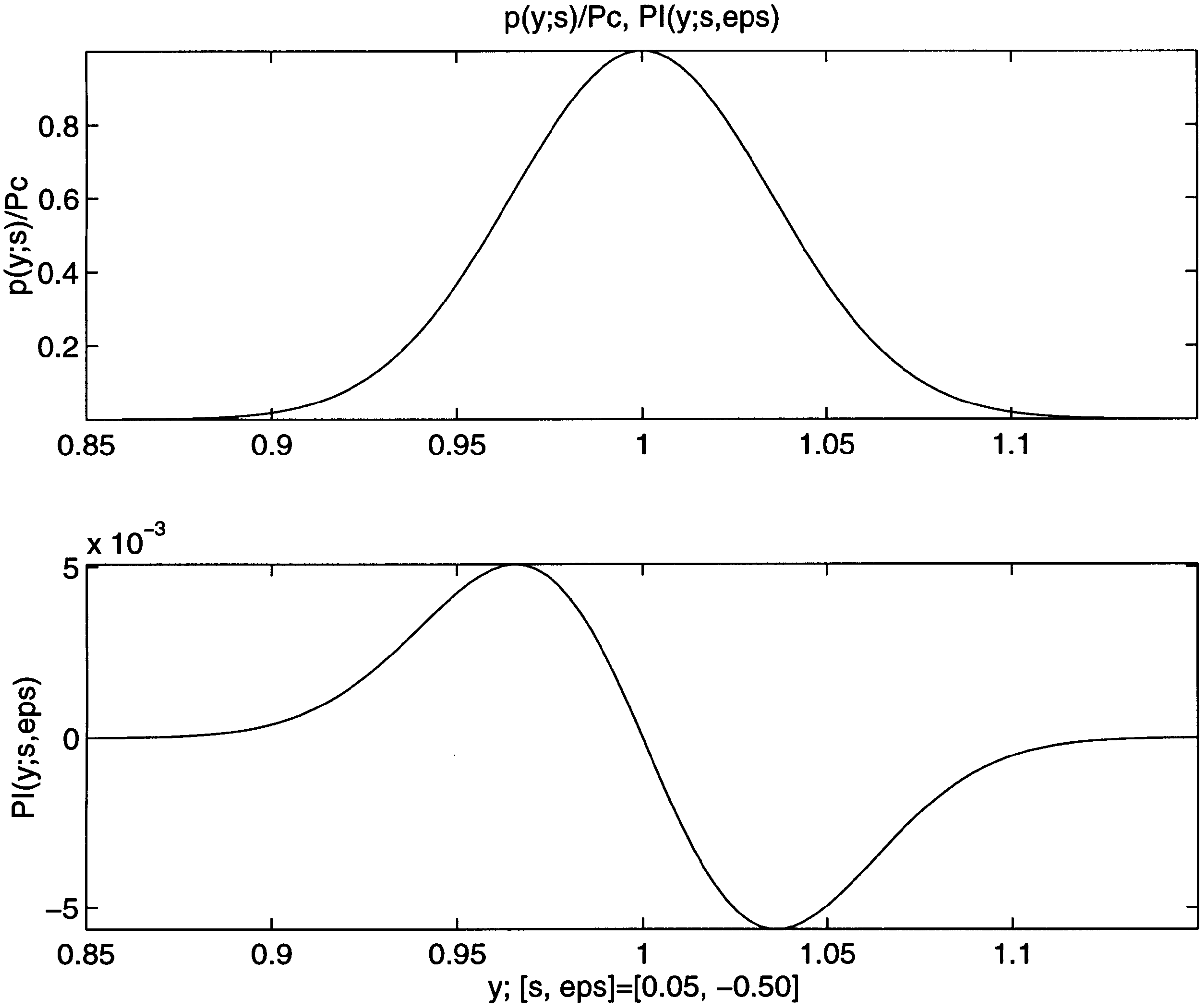

Figure 5-2: Pressure, Perturbation, $(p(y), \Pi(y), s = 0.05)$

by Eq. 5.41.b, with the perturbation parameter given by Eq. 5.68. These can be used in the simplified form of the equations of motion, Eq. 5.45, which required the same approximation, that the perturbation is small.

Following the arguments at the end of §5.3.1, the particle drift velocity in the steady state can be approximated by Eq. 5.52. This does not exactly apply to the pressure band, since the gas velocity is not constant radially and a steady state will not be reached. They do, however, illustrate the dependence of the convergence time on the band strength.

Consider a particle near the edge of the band, at the $1/e$ value of the pressure. This happens at $y = 1 - s$, so with small, the perturbation velocity is

$$v'_g \approx \tfrac{1}{2}\,\epsilon s v_k e^{-1}, \tag{5.71}$$

which is smaller than the Keplerian velocity for small band strength. Taking the values of the particle perturbation velocities, from Eq. 5.52, the radial drift velocity is

$$u'(s) \approx \frac{\alpha}{2+\alpha^2}\epsilon v_k s e^{-1}. \tag{5.72}$$

Then the convergence time can be estimated by

$$\begin{aligned} \tau_c &\approx \frac{s r_c}{u'(s)} && \text{(5.73.a)} \\ &\sim 0.4\frac{T_0}{\epsilon}\left(\frac{2+\alpha^2}{\alpha}\right), && \text{(5.73.b)} \end{aligned}$$

substituting the period for $2\pi r/v_k$ (see Fig. 5-3). The convergence time will be shorter for the stronger band, as expected, with an inverse proportionality. In addition, the convergence time will be long if the relaxation time ($\tau_\eta = T_0/\alpha$) is either very long or very short, supporting the expectation that strongly or uncoupled particles would not tend to drift significantly. The convergence time is minimized for $\alpha = \sqrt{2}$,

$$\tau_{c,min} \sim \frac{T_0}{\epsilon}, \tag{5.74}$$

so the particle will reach the center of the band in $1/\epsilon$ orbits.

5.4 Two-Dimensional Vortices

While a study of the axisymmetric pressure band is useful to understand the basic physical process governing the drift of particles, it is physically more relevant to study the effects of two dimensional vortices on particle flows. The equations of motion, as derived in §5.2, are integrated to determine the particle trajectories after the gas velocity is specified.

The gas velocity can be obtained in two ways: from a functional form of an elliptical vortex, and from the robust vortex data. Using the functional form has several advantages, since it gives more control over the vortex parameters, it is an exact solution of the vorticity equation, and the calculations are performed significantly faster. The Cartesian limit of the annular coordinates is used, however, so it is not an exact solution for a finite-sized vortex in the disk.

To get the best representation of a vortex in the disk, the robust vortex in annular coordinates is used. The velocity is specified on a discrete grid, so the values at intermediate points must be interpolated. While this introduces a small error, the resulting particle trajectories are not significantly affected.

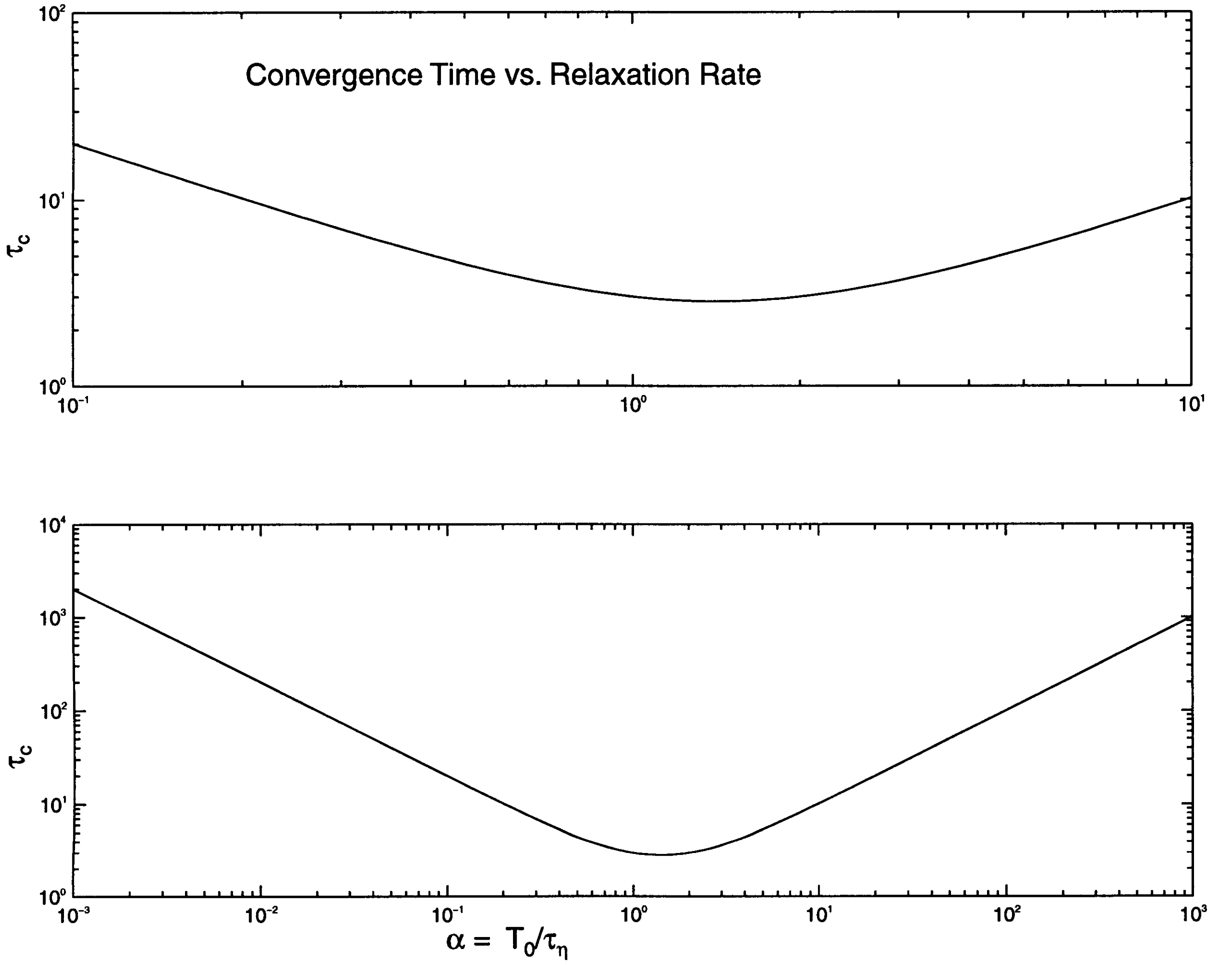

Figure 5-3: Convergence time, τ_c vs. relaxation rate, α, with $\alpha = T_0/\tau_\eta$, and $0.4T_0/\epsilon = 1$

5.4.1 Robust Gas Vortex in Annular Coordinates

The velocity, streamfunction, and vorticity fields of the robust vortex are determined by interpolating the discretized data from the gas model, as described in §6.1. The (u_g, v_g) values are then used in Eq. 5.25, which are integrated by the dust model to calculate the particle trajectories.

Chapter 6

Numerical Experiments of Dust Trajectories

The equations of motion for dust particles can be integrated numerically to study the effect of the gas flow on the particle trajectories. Since the equations of motion are ordinary differential equations, a Runge-Kutta scheme can be used. The series of gas flows examined includes the pressure band, the elliptical vortex, and the robust vortex in annular coordinates. For each, the trajectories can be used to calculate the convergence time for particles as a function of the particle relaxation time and gas flow parameters.

6.1 Numerical Model

The numerical model involves a temporal integration of the dust particle equations of motion using a fourth-order Runge-Kutta scheme, as used for the vorticity equation integration (Eq. 4.16). The gas flow is specified by either a functional form, for the pressure band and the elliptical vortex, or a discretized data set, for the elliptical vortex and the robust vortex. For the particles, the relaxation time and the initial position are specified, and the initial velocity is set equal to the velocity of the gas at that position.

The periodic boundary condition needs to be implemented, both by having particles wrap around the integration region and by making the streamfunction continous and differentiable at the angular boundary. In addition, for the discrete fluid data, the gas velocity at intermediate particle positions needs to be determined by interpolation.

The accuracy of the model can be measured by using particles which track the gas, with zero relaxation time. These particles should follow the streamlines, so, for a steady flow, the value of the streamfunction at the particle positions should not change throughout the trajectory, and the error is a measure of the numerical accuracy of the integration.

6.1.1 Periodic Boundary Conditions

As the particles traverse the region, they tend to move across the boundaries in the angular direction, and the periodic boundary condition allows them to wrap around to the other side. For the elliptical vortex, the streamfunction and its derivative, the velocity, must be continuous across the boundary so that the error in the particle trajectories is minimized. This can be accomplished by filtering the streamfunction and the radial velocity. Within a width w_f of the boundary, the filter is

$$
\begin{aligned}
a(x) &= \begin{cases} \frac{\pi}{w_f}(x - x_{min}) & x - x_{min} < w_f \\ \frac{\pi}{w_f}(x_{max} - x) & x_{max} - x < w_f \end{cases}, && \text{(6.1.a)} \\
f(x) &= \tfrac{1}{2}(1 - \cos(a)), && \text{(6.1.b)} \\
fx &= \frac{\pi}{2w_f}\sin(a). && \text{(6.1.c)}
\end{aligned}
$$

The effects of this filter can be tested in two ways. First, by increasing the angular width of the region, the need for the filter is minimized, so the difference in the trajectories is due to the filter. In addition, the change in the streamfunction over the whole trajectory indicates if the filter allows the particle to shift to different streamlines.

6.1.2 Cubic Interpolation

The robust vortex data is calculated on a discrete grid, so the gas velocity at the particle positions must be interpolated, for which a cubic interpolation method is used. A 4 × 4 grid is specified around the particle position, with the particle within the central element. If the particle is in the element along either radial boundary, it is assumed that it has escaped the region, and the calculation stops. For the angular boundaries, extra columns of data are used on both sides, taking advantage of the periodic boundary conditions, so the particle remains in the central element.

The denominator coefficient matrix, $\mathcal{D}_{ij}$, is generated initially for the $4x4$ grid around the element. Then the particle position is used to calculate the numerical coefficient, $\mathcal{N}$. Finally, the fluid values on the grid are used to calculate the interpolated values,

$$
\begin{aligned}
\mathcal{D}_{ij} &= \sum_k \sum_l (x_i - x_k)(y_j - y_l), && \text{(6.2.a)} \\
f(x,y) &= \sum_i \sum_j f_{ij} \frac{(x - x_i)(y - y_j)}{\mathcal{D}_{ij}}. && \text{(6.2.b)}
\end{aligned}
$$

The error from using interpolation on the discrete grid can be measured by comparing the functional and discretized elliptical vortex calculations.

6.2 Numerical Experiments

6.2.1 Pressure Band

The pressure band can be characterized by two parameters, the width and the strength, once the band is normalized using the center position. Calculations show that particles do converge into the center of the band if the strengh is negative, corresponding to a high pressure band.

The convergence time for a particle depends on the relaxation time, the initial position, and the band parameters. The convergence time, as a function of the relaxation time, has a minimum, as expected from §5.3.1. The relaxation time corresponding to the minimum convergence time can be calculated, as shown in Fig. 6-1. The convergence time is determined by measuring the time for a particle to drift to the center of the band from the edge of the band, one band width away from the center.

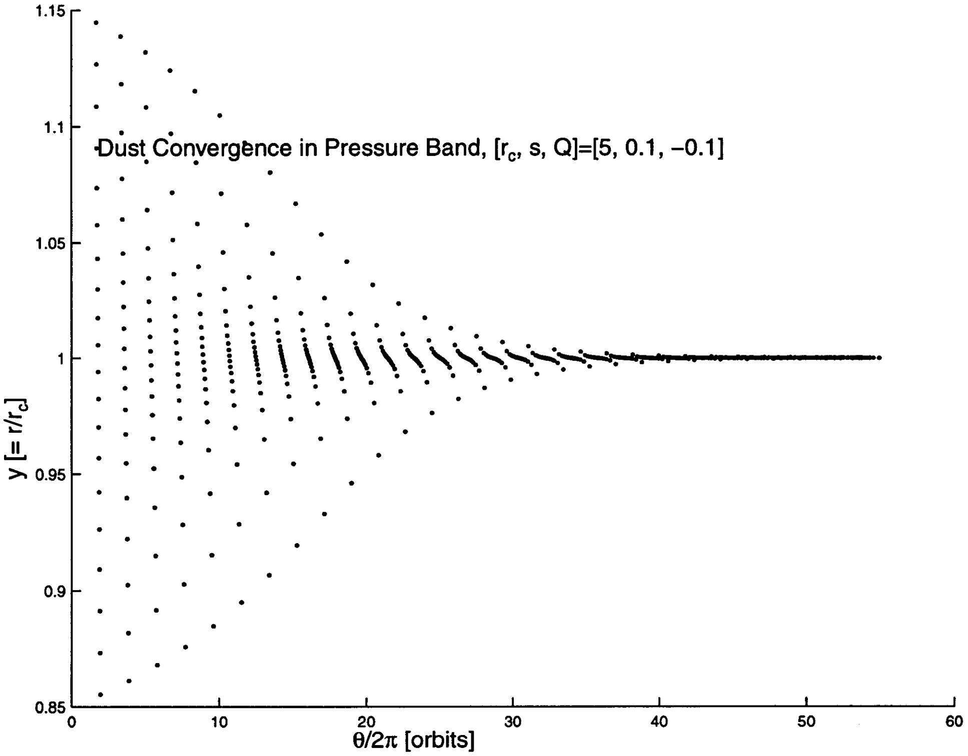

Figure 6-1: Relaxation time vs. minimum convergence time

6.2.2 Elliptical Vortex

While both the relaxation time and the vortex strength are important factors in the convergence time, for the elliptical vortex the relaxation time is more important. As seen in Fig. 6-5, the particles with the relaxation time of $\tau_\eta = 10^{-2}$ tend to converge slightly faster for $Q = 0.1$ than the particles with $\tau_\eta = 10^{-1}$ and $Q = 0.5$.

6.2.3 Single Vortex

Dust particles are distributed in a fluid field which includes a vortex. The particles with $\tau_\eta \sim 0.1$–0.2 yr have the fastest convergence times, while either shorter or longer relaxation times converge more slowly. The results are very similar to those of the elliptical vortex, indicating that the temporal variation in the evolving vorticity field does not significantly affect the convergence of dust.

The vorticity field is shown in Fig. 6-6 to show gas flow within which the particles are suspended. Figure 6-7, shows the rapid convergence of particles into the center of the vortex. Particles first move radially toward the center of the vortex. Then, when they are in the same radial band as the vortex, the particles are trapped inside the vortex. The cluster of particles is not centered in angle because the center of the vortex has drifted. The particles which are closer to the sun than the vortex are captured more rapidly than those further away from the sun. This is an effect of the geometry of the annular coordinates, where the radial positions of $y = 0, \pi/2,$ and π correspond to $r = 1.0, 1.5,$ and 2.2 respectively.

The dependence of the convergence time on τ_η is shown in Figs. 6-8–6-10. Starting with the initial distribution of particles at t_0, Fig. 6-8 shows the distribution of the particles at the end of the calculation, at $t_f = 11.1$ yr for different values of τ_η. The spread of particles is measured by calculating the standard deviation of the radial positions. In Fig. 6-9, the standard deviations for different values of τ_η are plotted as a function of time during the run. In Fig. 6-10, the standard deviations at the end of the calculation are shown. While the effect of the gas flow is strongest for $\tau_\eta \approx 0.1$–0.2 yr, there is a range of several orders of magnitude in τ_η for which there is a noticable gas effect.

In Fig. 6-11, the particles along the central vertical line are shown for $\tau_\eta = (1.0, 0.1, 0.01)$. The particles spread out in angle while moving radially toward the vortex. In addition, particles with one τ_η cross the trajectories of particles with different τ_η, enhancing the probability of collisions and coagulation.

6.2.4 Multiple Vortices

Particles suspended in a vorticity field with two vortices behave very similarly to the particles in a single vortex field. The initial and final vorticity fields are shown in Fig. 6-12. The particle positions at the initial and final times are shown in Fig. 6-13. The particle distributions shown in Fig. 6-14 indicate the same preference for $\tau_\eta \approx 0.1$–0.2 yr as seen with the single vortex.

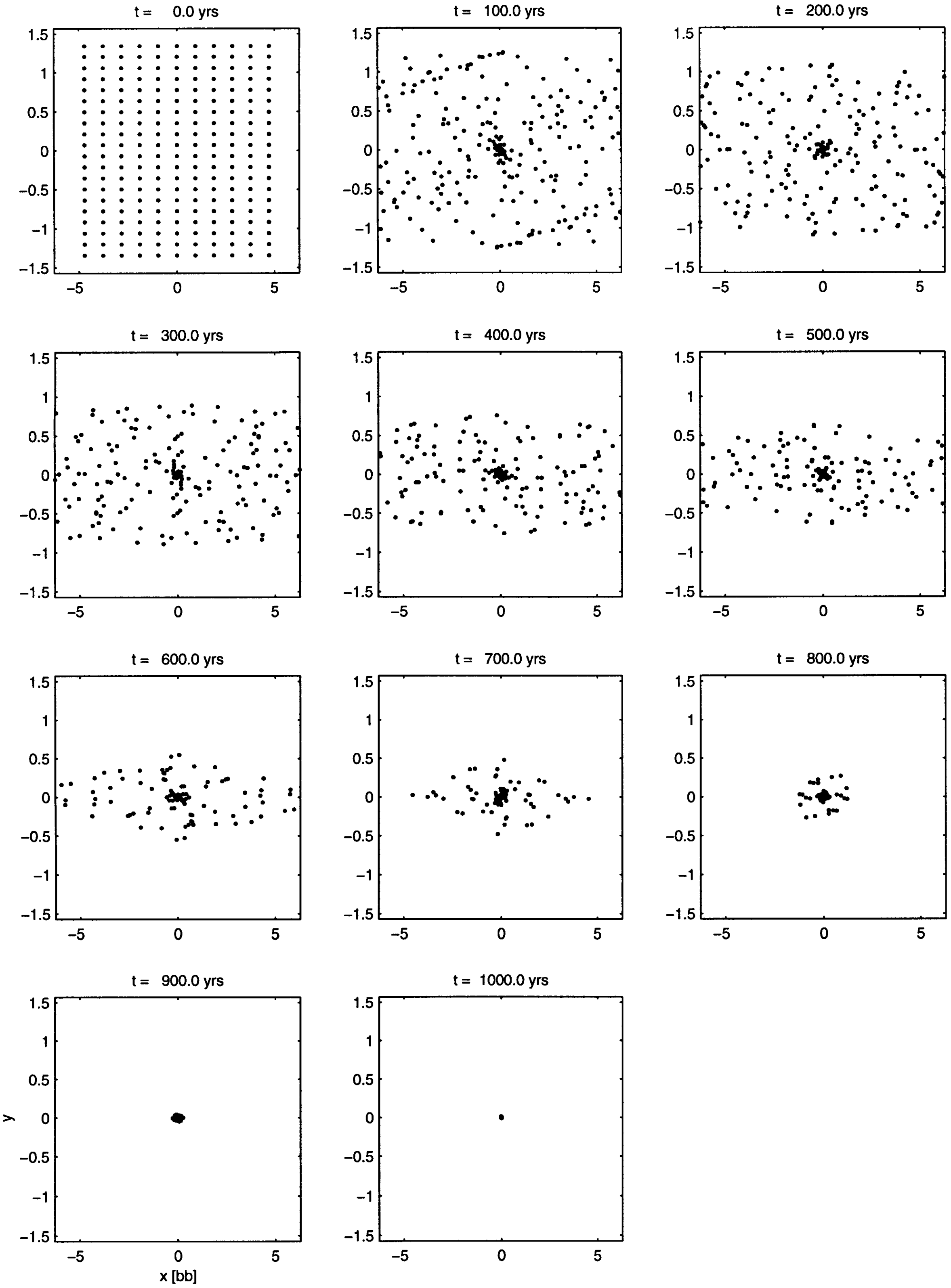

Figure 6-2: Convergence for particles in an elliptical vortex, $Q = 0.5$, $\tau_\eta = 10^{-1}$

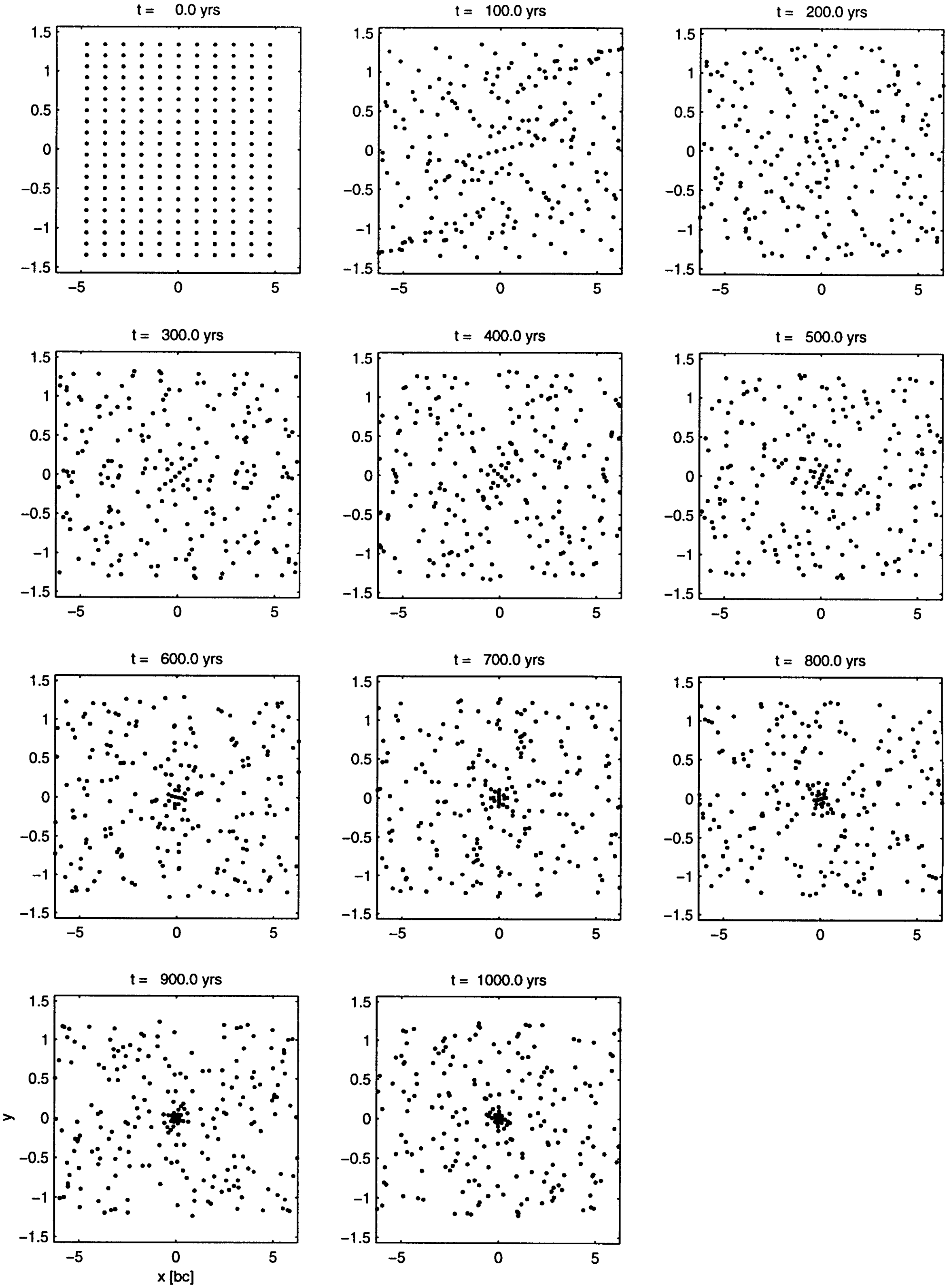

Figure 6-3: Convergence for particles in an elliptical vortex, $Q = 0.5$, $\tau_\eta = 10^{-2}$

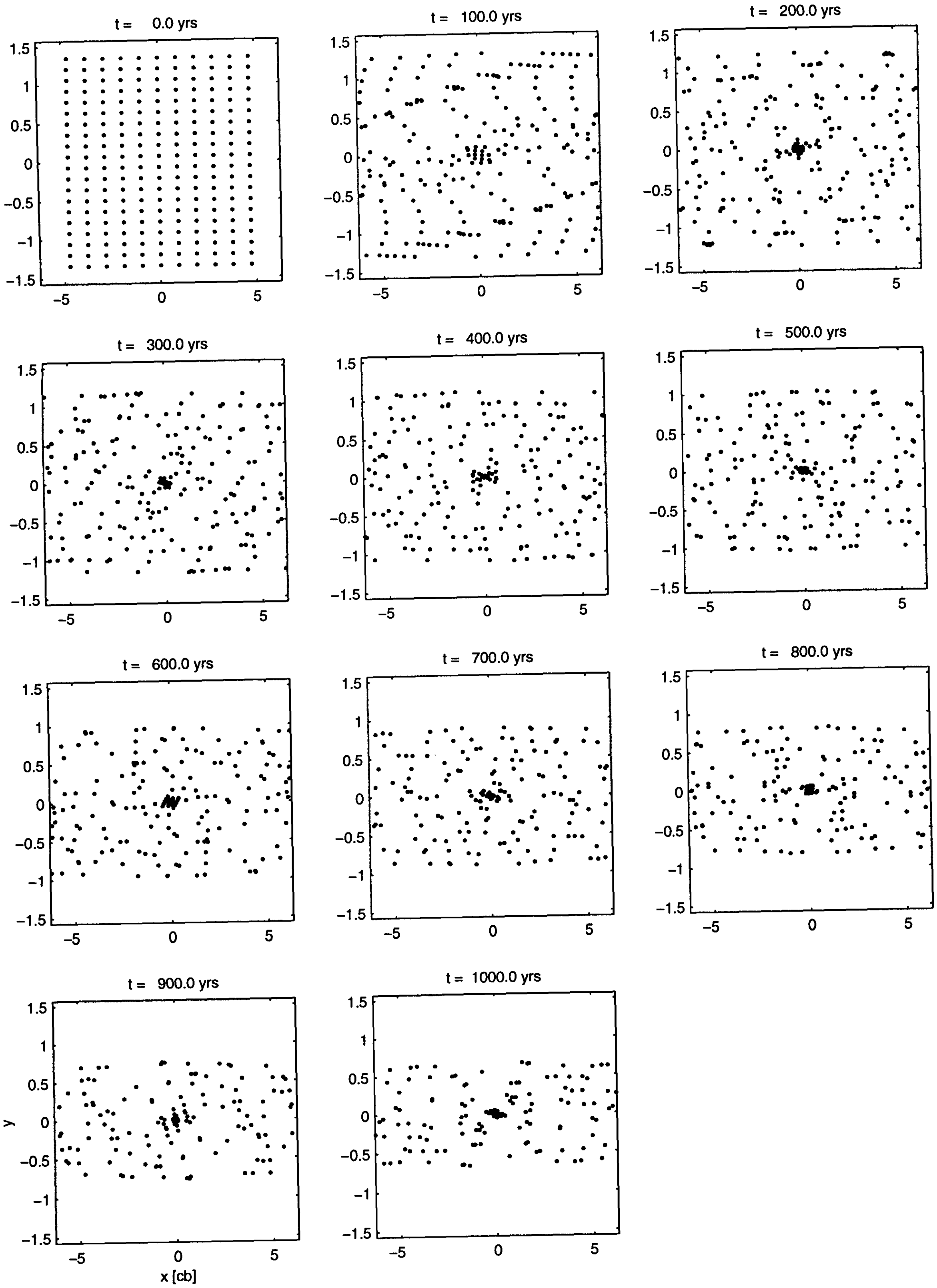

Figure 6-4: Convergence for particles in an elliptical vortex, $Q = 0.2$, $\tau_\eta = 10^{-1}$

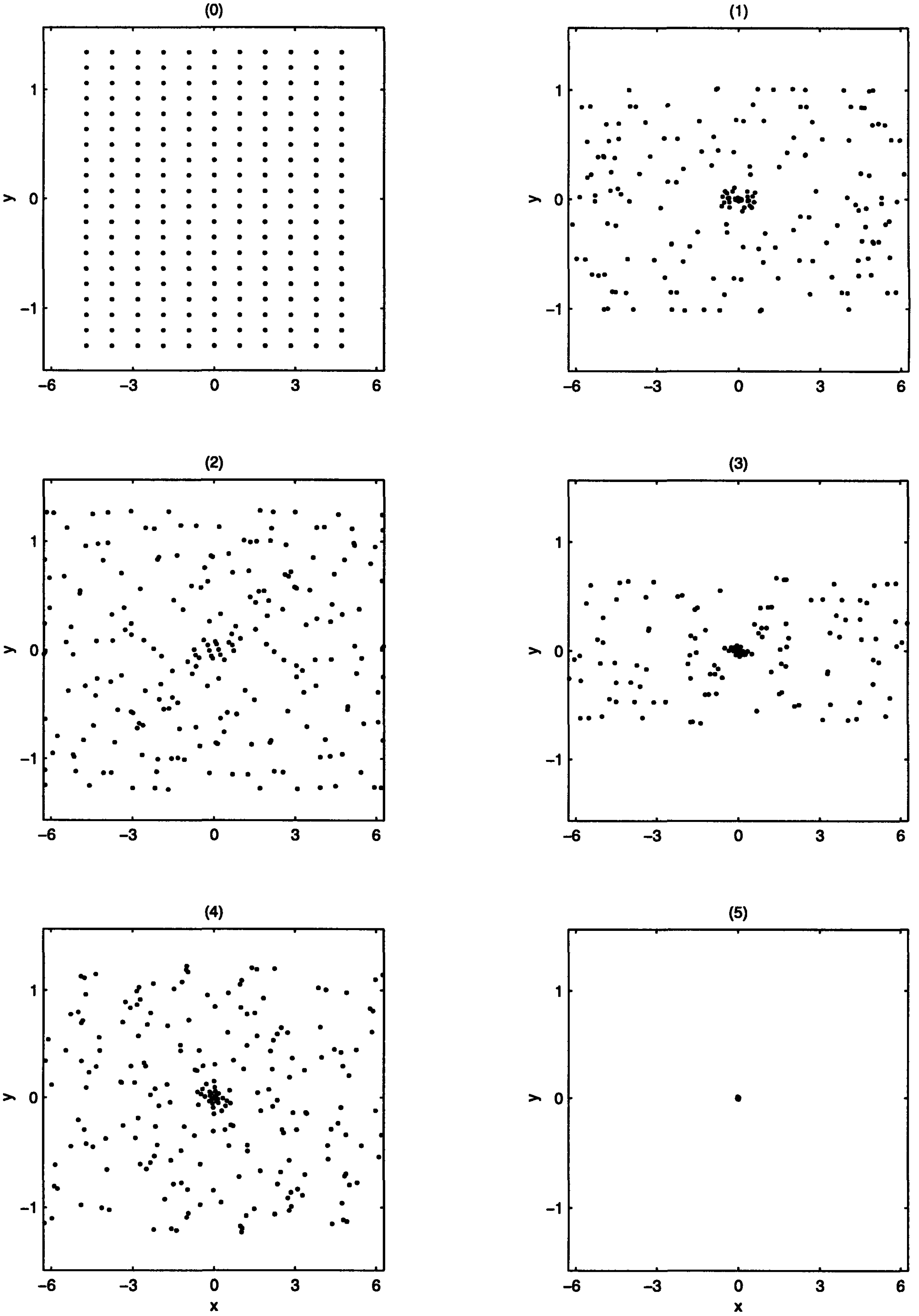

Figure 6-5: Convergence for particles in an elliptical vortex, (0): $t = 0$; (1): $[Q, \tau_\eta] = [0.1, 10^{-1}]$; (2): $[0.2, 10^{-2}]$; (3): $[0.2, 10^{-1}]$; (4): $[0.5, 10^{-2}]$; (5): $[0.5, 10^{-1}]$

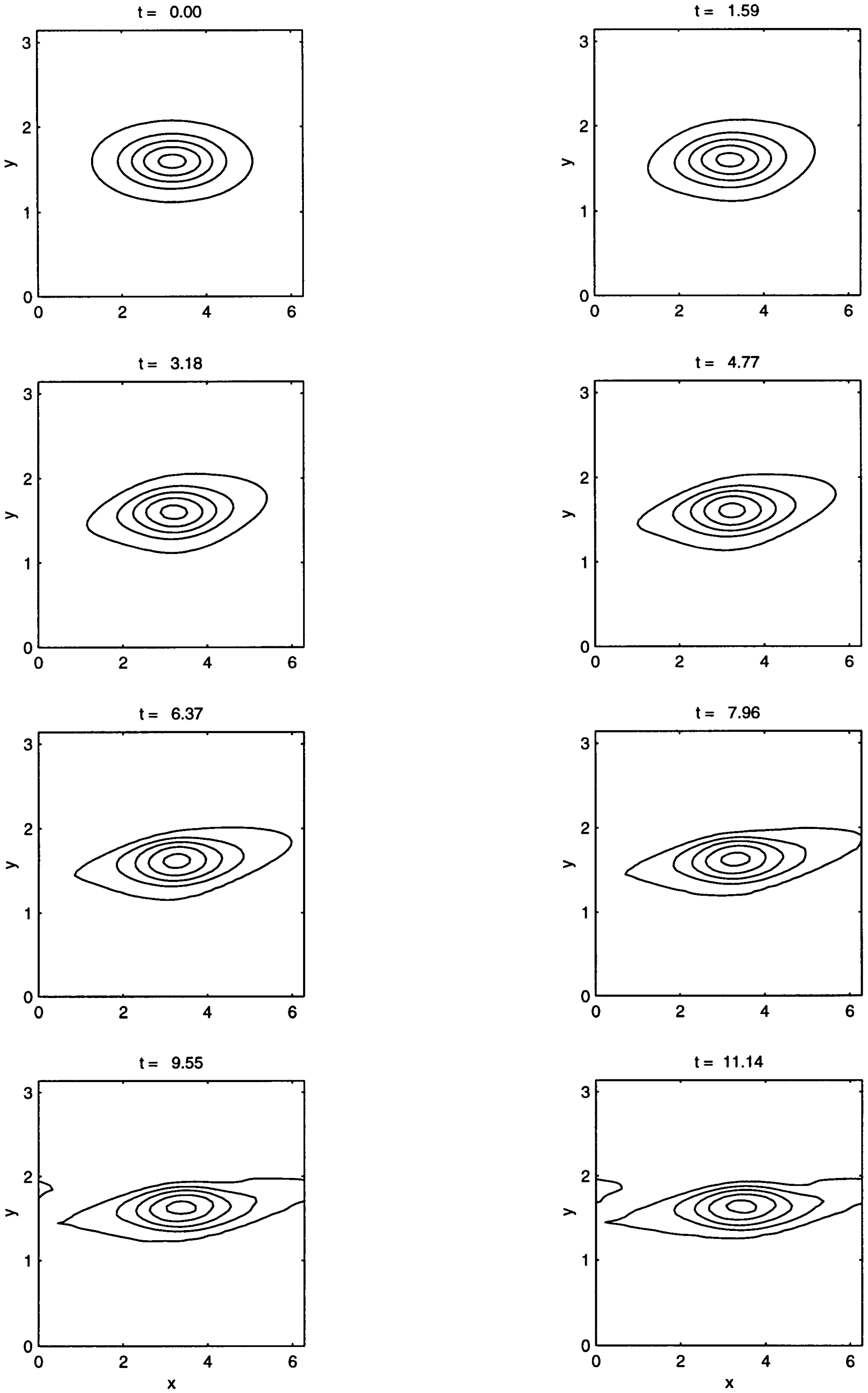

Figure 6-6: Gas flow

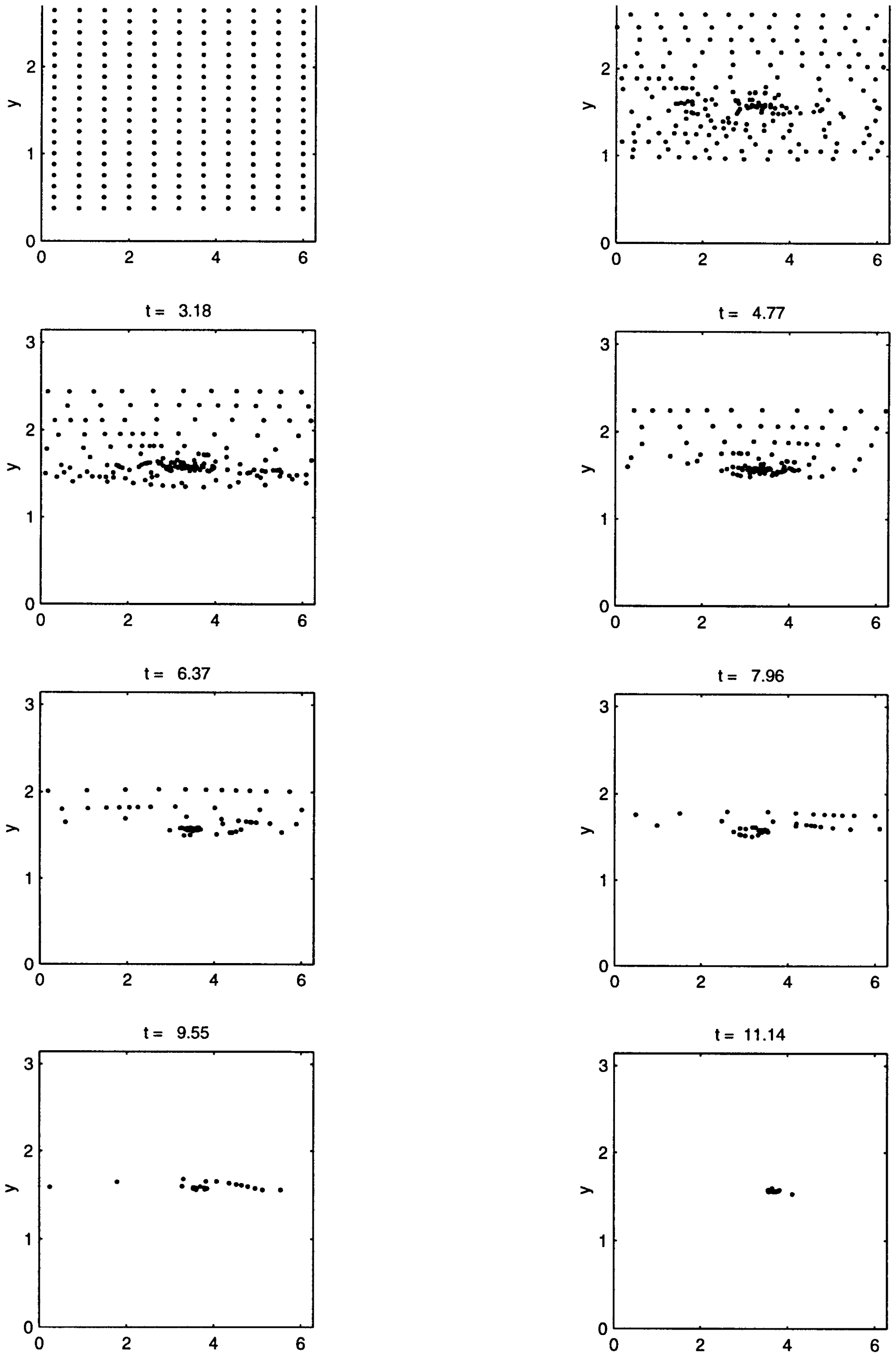
y
0
1
2
0
2
4
6
t = 3.18
t = 4.77
t = 6.37
t = 7.96
t = 9.55
t = 11.14
3

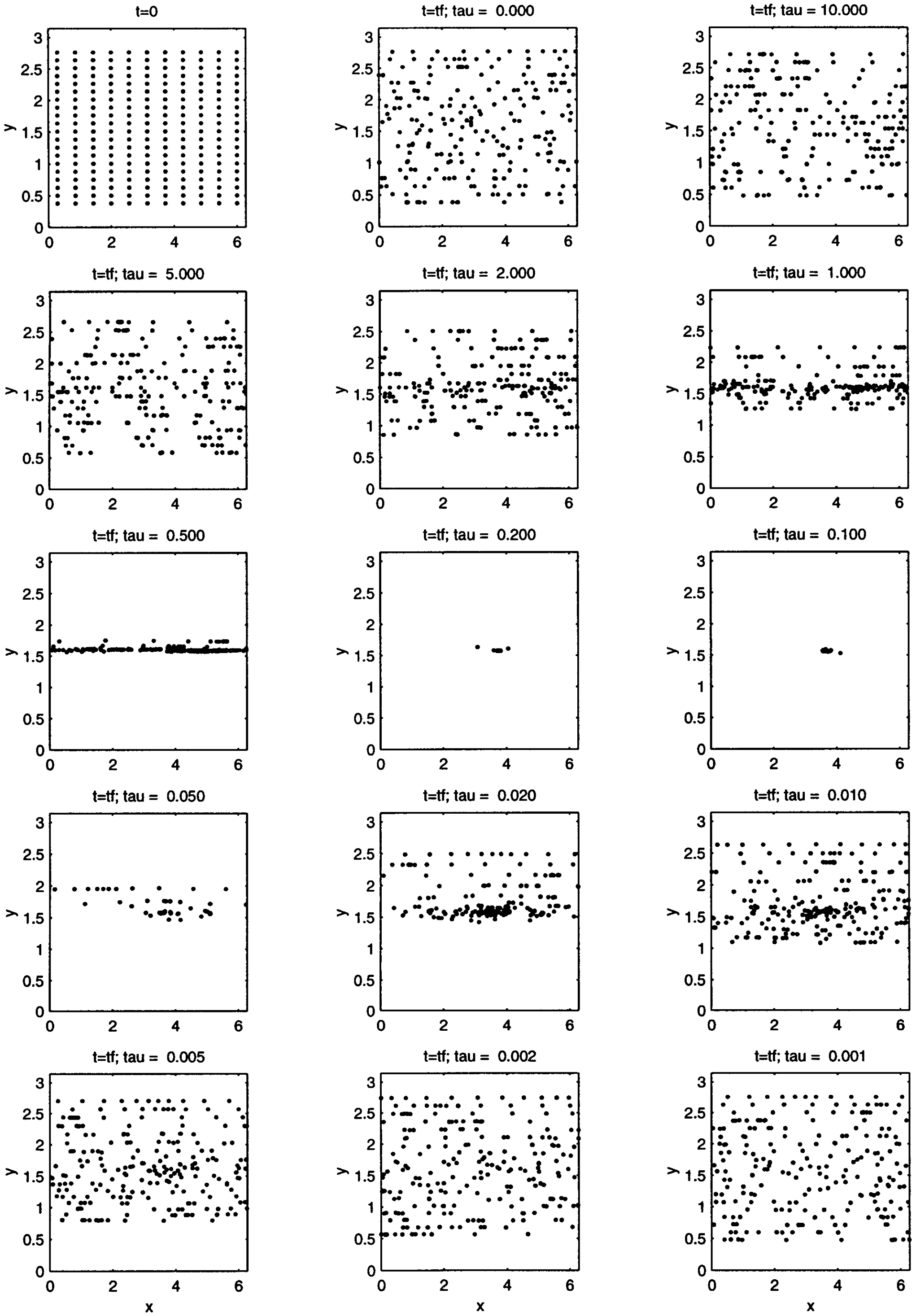
t=0

t=tf; tau = 0.000

t=tf; tau = 10.000

t=tf; tau = 5.000

t=tf; tau = 2.000

t=tf; tau = 1.000

t=tf; tau = 0.500

t=tf; tau = 0.200

t=tf; tau = 0.100

t=tf; tau = 0.050

t=tf; tau = 0.020

t=tf; tau = 0.010

t=tf; tau = 0.005

t=tf; tau = 0.002

t=tf; tau = 0.001

Figure 6-8: Particles at end of run ($t_f = 11.1\,\mathrm{yr}$), different values of τ_η.

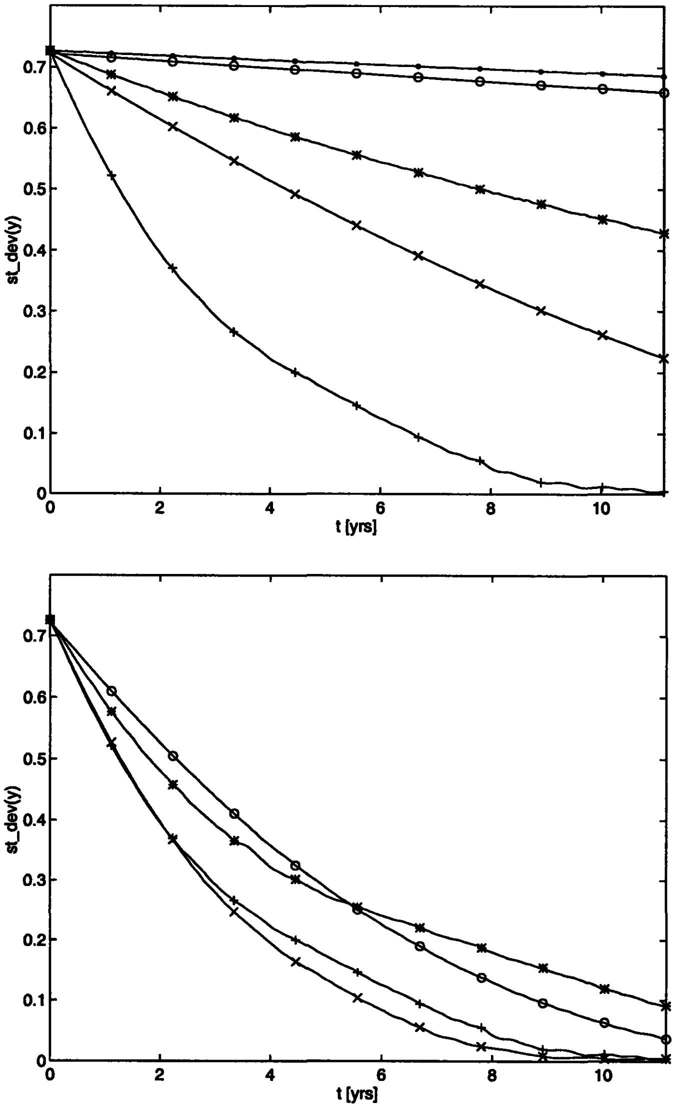

Figure 6-9: Particle distribution for different values of τ_η; The (symbol τ_η) pairs for each figure are (a) $(\circ\ 10.0), (\times\ 1.0), (+\ 0.1), (*\ 0.01), (\bullet\ 0.001)$; (b) $(\circ\ 0.5), (\times\ 0.2), (+\ 0.1), (*\ 0.05)$

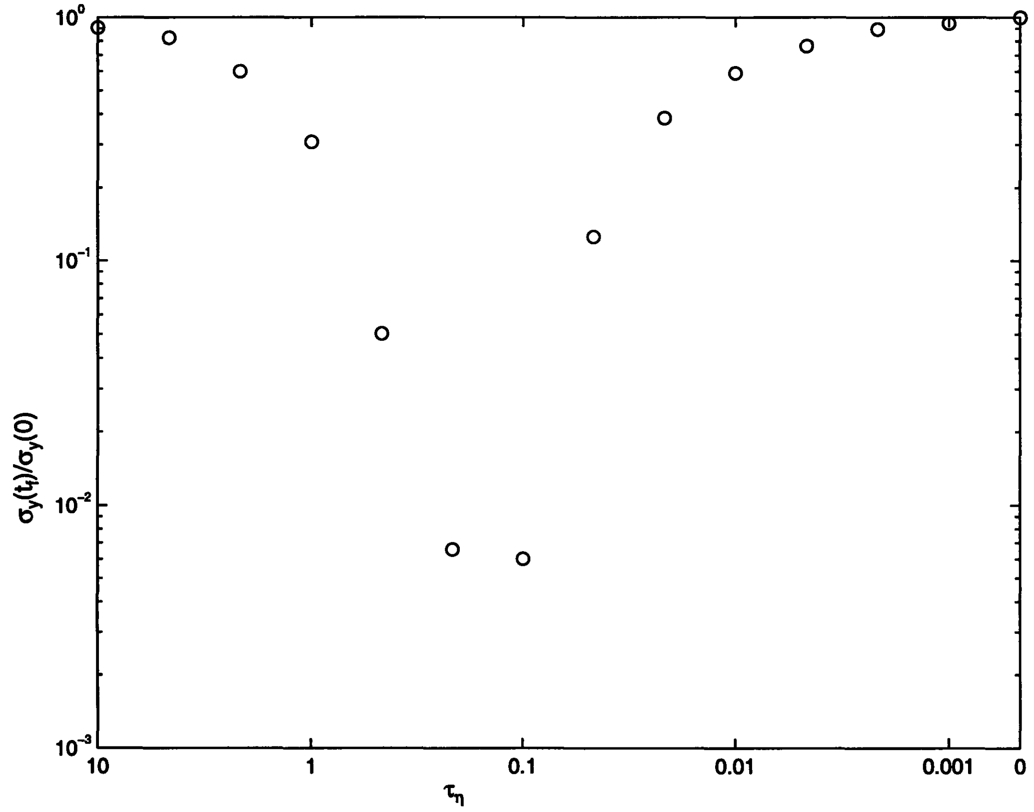

Figure 6-10: Radial spread of particles for different τ_η at $t_f = 11.1\,\mathrm{yr}$

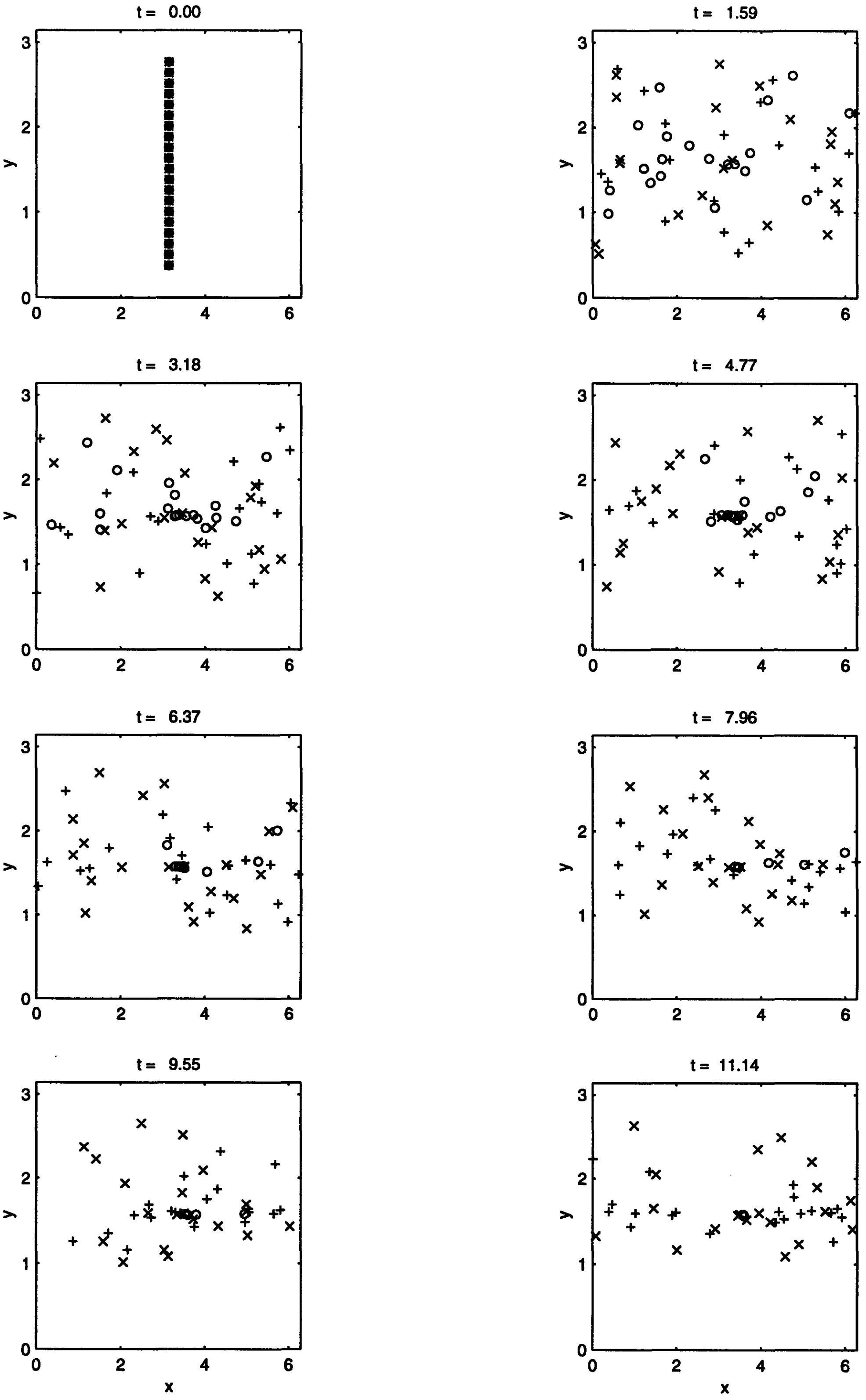

Figure 6-11: Positions of particles originally located along central vertical line; The (symbol τ_η) pairs are $(+\ 1.0), (\circ\ 0.1), (\times\ 0.01)$

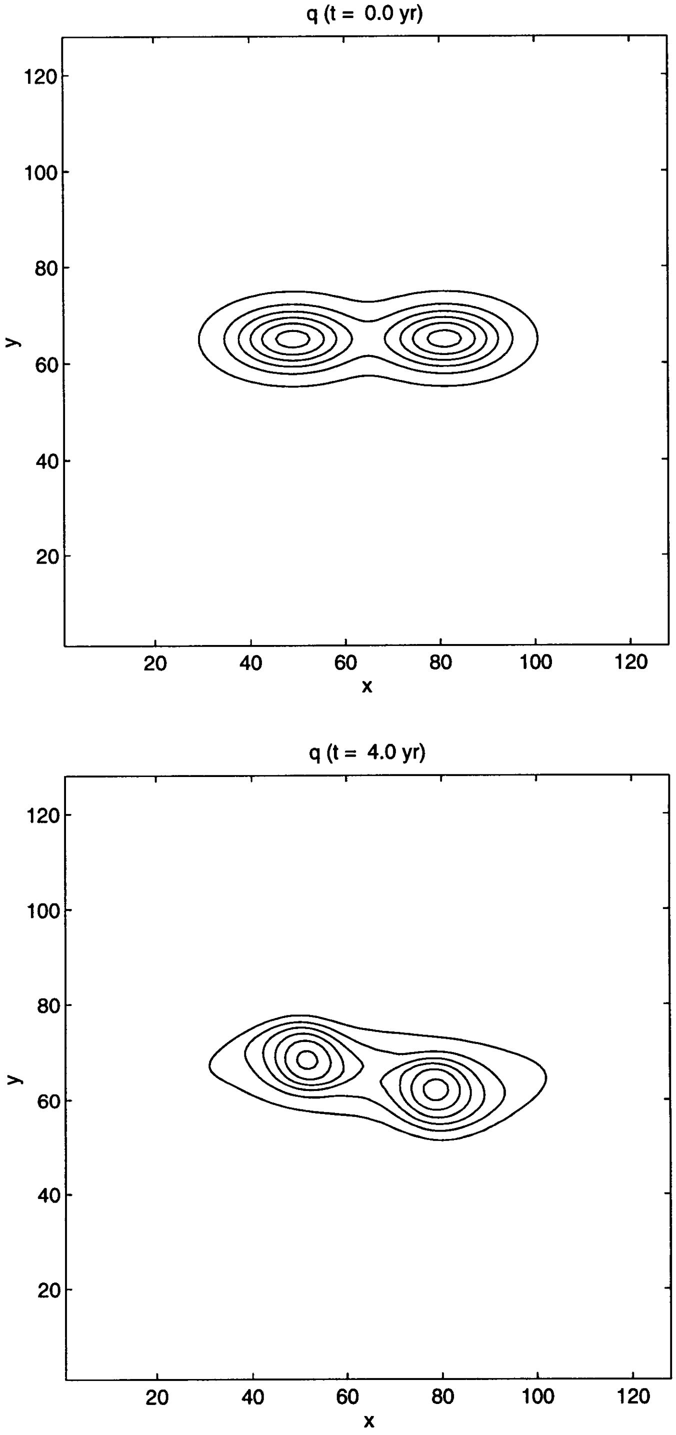

Figure 6-12: Gas flow for merging vortices

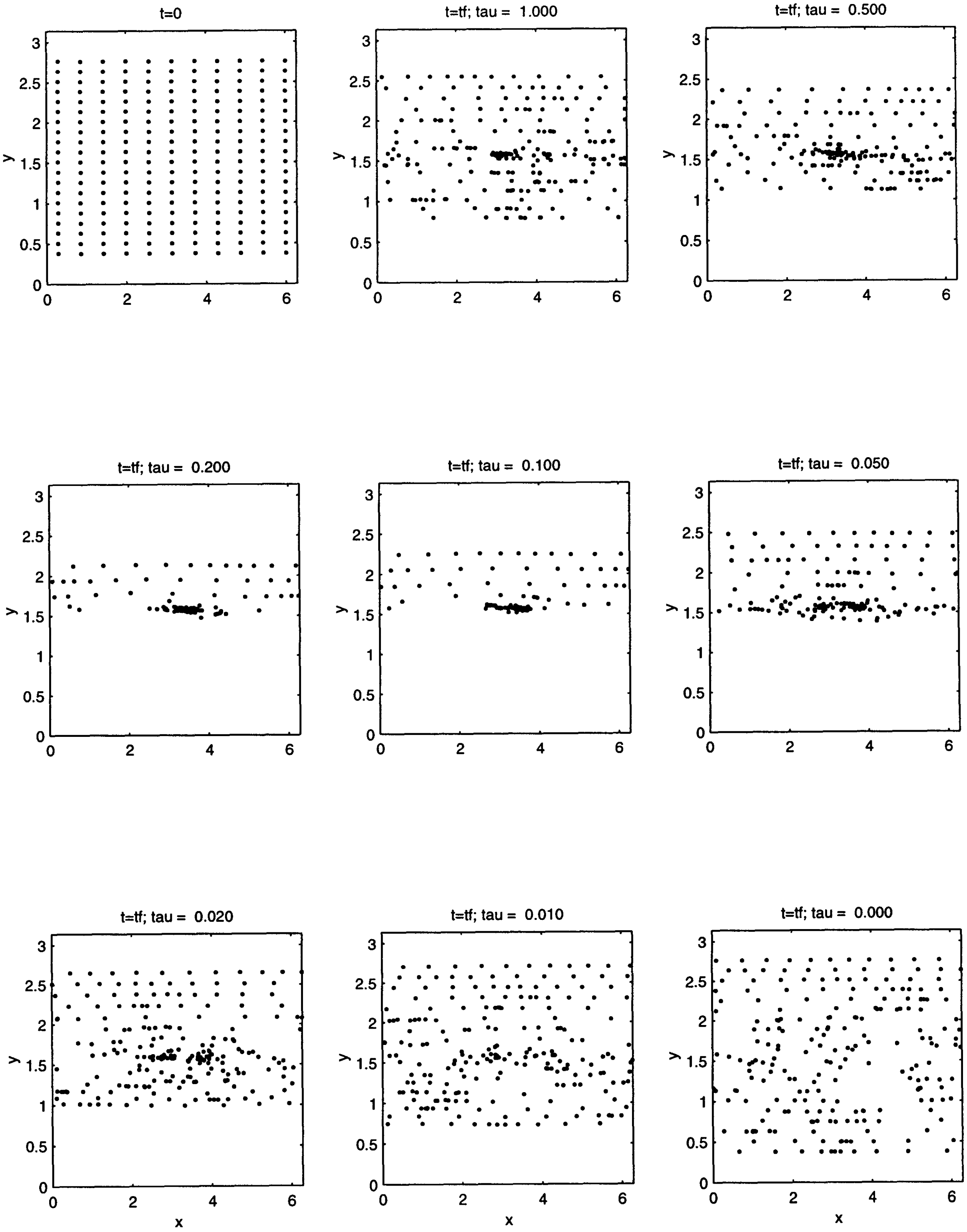

Figure 6-13: Dust flow in merging vortices

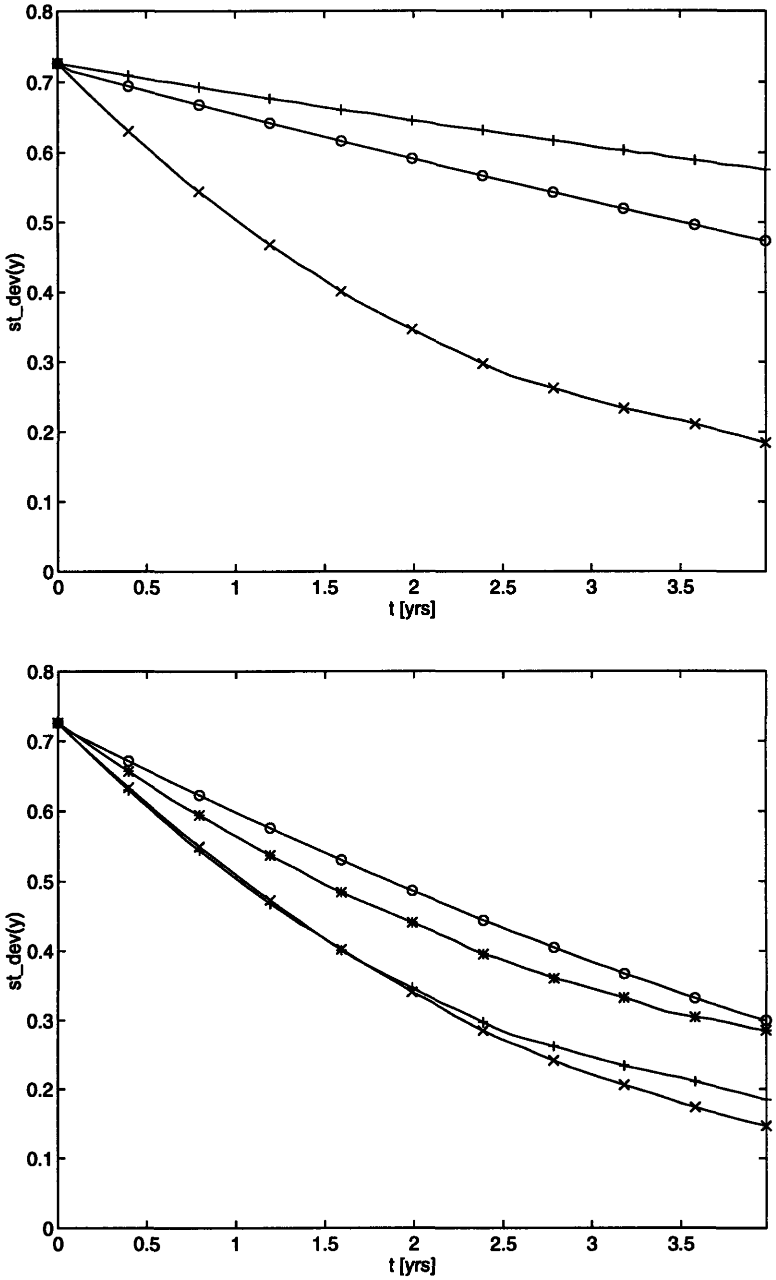

Figure 6-14: Convergence times in merging vortices for different values of τ_η; The (symbol τ_η) pairs for each figure are (a) $(\circ\ 1.0), (\times\ 0.1), (+\ 0.01)$; (b) $(\circ\ 0.5), (\times\ 0.2), (+\ 0.1), (*\ 0.05)$

Chapter 7

Conclusions and Further Work

One important question in understanding the formation of the solar system is how small particles accumulate into larger bodies, with sizes ranging from nanometers to thousands of kilometers. For the range from millimeters to meters, vorticies in the gas may enhance the coagulation process. To examine this hypothesis, both the characteristics of a gas vortex and the effect on dust particles were studied.

7.1 The Gas Vortex

A form of the vorticity equation was derived assuming inviscid, barotropic, locally incompressible, two-dimensional flow of a neutral gas. The form in use does retain nonlinear terms of the velocity and its derivatives, as well as the curvature of the rotating field. With the aid of faster computers, further work could treat a compressible, viscous fluid with three-dimensional motions and magnetic fields. This would probably be most useful in understanding how vortices form, especially as the gas settles into a circumstellar disk from a spherical cloud. To understand the behavior of the vortex after it has been formed, the approximations made seem reasonable.

A numerical model was developed to examine the evolution of a vorticity field. A pseudospectral scheme was used to calculate the spatial products and derivatives in the vorticity equation, and a Runge-Kutta scheme was used for the time integration. Different vorticity fields were studied with this model including a single vortex, multiple vortices, and random vorticity fields.

A single vortex was used to study the orientation, size, shape, strength, and robustness of a vortex. The orientation is most important–only a vortex with a negative vorticity, prograde relative to the *local* flow, oriented along the angular axis is long-lived. This is the only case where the vortex gas flow is predominantly parallel to the shear, perpendicular to the shear for only a fraction of the time, and does not oppose the shear.

The strength and shape are definitely related, very closely following the functional form for an elliptical vortex in a rotating, cartesian geometry. The stronger vortex tends to be rounder, while the weaker vortex is stretched in the angular direction by the Keplerian shear. This is definitely a one-way relationship: the strength remains fixed while the shape changes. The size, shape, and area are also related. Here, the area remains fixed, the shape changes according to the strength, and then the linear size conforms to the other parameters. The dependencies of the parameters are shown below,

orientation
strength
area
shape
size

The robustness of a single vortex was estimated by performing a calculation of order 10^3 yr or over 10^6 timesteps. The strength of the vortex changes by less than 1% in this time, indicating that, once formed, this vortex is long-lived on timescales long enough to affect solar system formation processes, especially regarding dust accumulation.

Vorticity fields with multiple vortices were used to see if they would merge in the presence of Keplerian shear, to see if a large vortex can be formed from smaller vortices. When the vortices are at the same radial distance, they quickly merge to form one vortex, in only a few orbit periods. If they are radially separated, however, they do not merge because the differential angular velocity takes them past each other too quickly for the interaction to have an effect.

A random vorticity field was used to get a preliminary idea of whether vortices can form in the Keplerian shear. While the merging is not efficient, there does appear to be some collection of vorticity in a few strong vortices with larger amplitudes than the initial field. Both the random field and multiple vortex experiments indicate that vortices do form in fairly short times, of order 10s of years. The scenario proposed here is that the three-dimensional, turbulent cloud settles into a disk with a very irregular vorticity field. As the behavior becomes more two-dimensional, the turbulent processes transfer energy to larger scales and this occurs through repeated mergers of vortices to form larger and more widely-spaces vortices. The latter part of this scenario is supported by the calculations in this thesis. For the first part, given the sparsity of detailed observations, a three dimensional calculation appears to be the best approach to gaining a better understanding of how vortices form.

7.2 Dust Particles Suspended in a Vortex

The behavior of dust particles suspended in the gas flow has also been studied, using the Stokes drag force as the link between the gas and the dust. The force can be written using the relaxation time, which is the timescale for the difference in the particle and gas velocity to exponentially approach zero. The relaxation time is proportional to the particle mass and inversely proportional to the gas viscosity and particle size. This assumes that the dust is composed of solid spheres; the behavior of fluffy particles may be important, depending on the coagulation of smaller particles. This should not change the qualitative results, however, since the Stokes drag force is due to the viscous boundary layer around the sphere rather than the actual collision of gas molecules with the dust particle. Using the fluid viscosity here does not invalidate the inviscid treatment of the gas flow because of the difference in length scales involved. For the gas vortex, the lengths are of order 10^{12} cm, while for the flow around dust particles, the lengths are of order 10^{-2}–10^{3} cm The corresponding change in the Reynolds number takes the flow from the inviscid regime to the viscous regime.

With the viscosity estimates for the gas flow, the relaxation times of $1.0, 0.1,$ and 0.01 cm correspond approximately to particles diameters of $60, 20,$ and 6 cm. While the actual sizes may vary with different viscosities and particle densities, the dynamics are completely parametrized by the relaxation time.

The ratio of the relaxation time and the period characterizes the interaction:

- relaxation time $\ll$ period: strongly coupled

- relaxation time $\sim$ period: weakly coupled
- relaxation time $\gg$ period: uncoupled

This follows from the equations of motion, where the gravity and drag force terms contribute to the net force on a particle. The strength of one force or the other depends on their timescales, the period and the relaxation time respectively. In the strongly coupled case, the particle tracks the gas flow, with no differential velocity. Uncoupled particles follow Keplerian trajectories, independent of the gas flow, since the drag force is insufficient to affect the motion. The most interesting dynamics occurs for weakly coupled particles, where there is some differential velocity, and the resulting force is strong enough to alter the trajectories.

The basic effect on the dust particles can be seen by using a pressure band. A high pressure band has the gas radially in from the center moving faster than the Keplerian velocity, while the gas radially out is moving slower, as summarized below,

	radially in	radially out
high pressure	positive velocity change	negative velocity change
low pressure	negative velocity change	positive velocity change

If a dust particle traveling at the Keplerian velocity is suspended in a gas moving faster than it, the particle is accelerated, increasing its energy and the semi-major axis of its orbit. This implies a drift which is radially outward. For a high pressure band, the drift is in toward the center of the band, and for a low pressure band, the particle drifts away from the band. Conversely, for a negative differential velocity, the particle drifts radially inward, to the center of a high pressure band and away from a low pressure band. Calculations with the pressure band confirm this analysis, and calculations with high pressure vortices show particles pulled toward the vortex center.

The convergence timescales for particles to reach the center of the vortex can be estimated as a function of the relaxation time. The convergence is shortest for relaxation times around $0.1 \sim 0.2\,\mathrm{yr}$, independent of the vortex strength. The vortex strength does influence the magnitude of the convergence time, with a weaker vortex resulting in longer convergence times. The shortest convergence times are approximately a few years for a vortex strength of $0.5\,\mathrm{yr}$. Particles of different sizes drift in at different rates, but this tends to increase the number of particle crossings, increasing the probability of collisions, helping to form larger bodies.

The models in this thesis argue that vortices can play a significant role as accumulation points for dust, as well as enhancing collisions, during the phase when larger particles are forming. This connection seems robust and not especially sensitive to the vortex structure. In addition, it is clear that vortices can survive for long enough that this mechanism can operate very effectively.

Bibliography

[1] Adams, F. C. and Watkins, R. (1995), "Vortices in Circumstellar Disks," *Astrophys. J.*, **451**, 314–327.

[2] Barge, P. and Sommeria, J. (1995), "Did Planet Formation Begin Inside Persistent Gaseous Vortices?," *Astron. Astrophys.*, **295**, L1–L4.

[3] Batchelor, G. K., *An Introduction to Fluid Dynamics*, Cambridge University Press, 1967.

[4] Beckwith, S. V. W., and Sargent, A. I. (1993), "The Occurrence and Properties of Disks Around Young Stars," in *Protostars and Planets III*, pp. 521–41.

[5] Bernatowicz, T. J. (1997), "Presolar Grains from Meteorites," in *From Stardust to Planetesimals*, pp. 227–251.

[6] Blum, J. and Münch, M. (1993), "Experimental Investigations on Aggregate-Aggregate Collisions in the Early Solar Nebula," *Icarus*, **106**, 151–167.

[7] Blum, J. (1997), "Coagulation Experiments," in *From Stardust to Planetesimals*, pp. 295–311.

[8] Canuto, C., Hussaini, M. Y., Quarteroni, A., & Zang, T. A., *Spectral Methods in Fluid Dynamics*, Springer-Verlag, 1988.

[9] Chandler, C. J., and Sargent, A. I. (1997), "The Role of Dust in Star and Planet Formation: Observations," in *From Stardust to Planetesimals*, pp. 25–36.

[10] Chandrasekhar, S., *Hydrodynamic and Hydromagnetic Stability*, Dover Publications, Inc., 1961.

[11] Drazin, P. G. & Reid, W. H., *Hydrodynamic Stability*, Cambridge University Press, 1981.

[12] Encrenaz, , *The Solar System*, Springer Verlag, 1990.

[13] Flierl, G. R. (1988), "On the Instability of Geostrophic Vortices," *J. Fluid Mech.*, **197**, 349–388.

[14] Fox, D. G. and Orszag, S. A. (1973), "Inviscid Dynamics of Two-Dimensional Turbulence," *The Physics of Fluids*, **16**, 169–171.

[15] Fox, D. G. and Orszag, S. A. (1973), "Pseudospectral Approximation to Two-Dimensional Turbulence," *J. Comp. Phys.*, **11**, 612–619.

[16] Goldreich, P. and Ward, W. R. (1973), "The Formation of Planetesimals," *Astrophys. J.*, **183**, 1051–61.

[17] Hayashi, C., Nakazawa, K., and Nakagawa, Y. (1985), "Formation of the Solar System," in *Protostars and Planets II*, pp. 1100–53.

[18] Huang, K., *Statistical Mechanics*, John Wiley & Sons, 1987.

[19] Kerridge, J. F., and Anders, E. (1990), "Boundary Conditions for the Origin of the Solar System," in *Meteorites and the Early Solar Sytem*, pp. 1149–54.

[20] Landau, L. D. & Lifschitz, E. M., *Fluid Mechanics, 2nd Ed.*, Pergamon Press, 1987.

[21] Levy, E. H. & Lunine, J. I., eds., *Protostars and Planets III*, U. Arizona Press, 1993.

[22] Marble, F. E. (1970), "Dynamics of Dusty Gases," , , .

[23] Marcus, P. S. (1990), "Vortex Dynamics in a Shearing Zonal Flow," *J. Fluid Mech.*, **215**, 393–430.

[24] Marcus, P. S. (1993), "Jupiter's Great Red Spot and Other Vortices," *Ann. Rev. Astron. Astrophys.*, **31**, 523–73.

[25] McQuarrie, D. A., *Statistical Mechanics*, Harper Collins Publishers, 1976.

[26] Meacham, S. P., Flierl, G. R., and Send, U. (1990), "Vortices in Shear," *Dynamics of Atmospheres and Oceans*, **14**, 333–86.

[27] Moore, D. W., and Saffman, P. G. (1971), "Structure of a Line Vortex in an Imposed Strain," in *Aircraft Wake Turbulence and Its Detection* (J. H. Olsen, A. Goldburg, and M. Rogers, eds.), New York, Plenum Press pp. 339–354.

[28] Morse, P. M. & Feshbach, H., *Methods of Theoretical Physics*, McGraw-Hill Book Co., Inc., 1953.

[29] Mundy, et. al. (1996), "Observations," *Astrophys. J.*, **464**, L169–L173.

[30] Pedlosky, J., *Geophysical Fluid Dynamics, 2nd Ed.*, Springer-Verlag, 1987.

[31] Pendleton, Y. J. & Tielens, A. G. G. M., eds., *From Stardust to Planetesimals*, Astronomical Society of the Pacific Conference Series, 1997.

[32] Press, W. H., Teukolsky, S. A., Vetterling, W. T., and Flannery, B. P., *Numerical Recipes in C, 2nd Ed.*, Cambridge University Press, 1993.

[33] Pringle, J. E. (1981), "Accretion Disks in Astrophysics," *Ann. Rev. Astron. Astrophys.*, **19**, 137–162.

[34] Safronov, V. S. (1972). In *Evolution of the Protoplanetary Cloud and Formation of the Earth and Planets* (Moscow: Nauka Press).

[35] Schwarzschild, M., *Structure and Evolution of the Stars*, Princeton University Press, 1958.

[36] Shore, S. N., *An Introduction to Astrophysical Hydrodynamics*, Academic Press, Inc., 1992.

[37] Shu, F. H., Adams, F. C. and Lizano, S. (1987), "Star Formation in Molecular Clouds: Observation and Theory," *Ann. Rev. Astron. Astrophys.*, **25**, 23–81.

[38] Shu, F. H., *The Physics of Astrophysics, Vol II: Gas Dynamics*, University Science Books, 1992.

[39] Shu, F., et. al. (1993), "The Collapse of Clouds and the Formation and Evolution of Stars and Disks," in *Protostars and Planets III*, pp. 3–45.

[40] Strikwerda, J. C., *Finite Difference Schemes and Partial Differential Equations*, Wadsworth, Inc., 1989.

[41] Strom, S. E., Edwards, S., and Skrutskie, M. F. (1993), "Evolutionary Time Scales for Circumstellar Disks Associated with Intermediate- and Solar-Type Stars," in *Protostars and Planets III*, pp. 837–866.

[42] Weidenschilling, S. J. (1980), "Dust to Planetesimals: Settling and Coagulation in the Solar Nebula," *Icarus*, **44**, 172–189.

[43] Weidenschilling, S. J. (1984), "Evolution of Grains in a Turbulent Solar Nebula," *Icarus*, **60**, 553–67.

[44] Weidenschilling, S. (1993a), "Dust Accretion," *Icarus*, **105**, 103–132.

[45] Weidenschilling, S. J., and Cuzzi, J. N. (1993), "Formation of Planetesimals in the Solar Nebula," in *Protostars and Planets III*, pp. 1031–60.

Appendix A

Derivations of Coordinate Systems

Several curvilinear coordinate systems are used in this thesis, so the unit vectors, vector derivatives, and transformations to other systems need to be determined. In particular, cylindrical and annular coordinates will be used extensively. While the equations for cylindrical coordinates are readily available, developing equations for this coordinate system will be helpful in doing the same for annular coordinates. These equations can be developed in two ways: using the generalized curvilinear coordinate transformations, and using directional derivatives. The first approach, following the description in Morse & Feshbach [28, §1.3,1.4], will be described in general and then applied to the specific systems. The second will be illustrated with cylindrical coordinates, and then applied to annular coordinates.

In addition, the cartesian limit of annular coordinates will be derived, as will an elliptical coordinate system.

A.1 Generalized Curvilinear Coordinate Systems

It is useful to understand how to transform quantities from Cartesian coordinates,

$$\boldsymbol{\xi} = \boldsymbol{\xi}(\xi, \eta, \zeta) = \hat{\varepsilon}_j \xi_j, \tag{A.1}$$

to curvilinear coordinates,

$$\boldsymbol{x} = \boldsymbol{x}(x, y, z) = \hat{a}_i x_i, \tag{A.2}$$

where $\hat{\varepsilon}_j$ and $\hat{a}_i$ are the unit vectors in Cartesian and curvilinear coordinates respectively. The unit vector transformations are related by the direction cosines matrix γ_{ij},

$$\begin{aligned} \hat{a}_i &= \gamma_{ij}\hat{\varepsilon}_j, && \text{(A.3.a)} \\ \hat{\varepsilon}_j &= \gamma_{ij}\hat{a}_i. && \text{(A.3.b)} \end{aligned}$$

The coordinate transformation equations, $\xi_j(x_i)$ and $x_i(\xi_j)$, are also needed. The scale factors, h_i, are used to relate the curvilinear differentials to the Cartesian differentials. The scale factors are calculated using either of two forms,

$$\begin{aligned} h_i^2 &= \sum_j \left(\frac{\partial \xi_j}{\partial x_i}\right)^2, && \text{(A.4.a)} \\ &= \left[\sum_j \left(\frac{\partial x_i}{\partial \xi_j}\right)^2\right]^{-1}. && \text{(A.4.b)} \end{aligned}$$

Then the length and volume elements are

$$\begin{aligned} ds^2 &= \sum_j d\xi_j^2 = \sum_i h_i^2 dx_i^2, && \text{(A.5.a)} \\ dV &= \prod_j d\xi_j = \prod_i h_i dx_i. && \text{(A.5.b)} \end{aligned}$$

The derivatives of the unit vectors are

$$\begin{aligned} \frac{\partial \hat{a}_i}{\partial x_i} &= \frac{\hat{a}_i}{h_i}\frac{\partial h_i}{\partial x_i} - \sum_k \frac{\hat{a}_k}{h_k}\frac{\partial h_i}{\partial x_k}, && \text{(A.6.a)} \\ \frac{\partial \hat{a}_k}{\partial x_i} &= \frac{\hat{a}_i}{h_k}\frac{\partial h_i}{\partial x_k}. && \text{(A.6.b)} \end{aligned}$$

To transform a Cartesian vector, $f_j(\xi,\eta,\zeta)$, to curvilinear components, $f_i'(x,y,z)$, use

$$\begin{aligned} f_i'(\boldsymbol{x}) &= \gamma_{ij} f_j(\boldsymbol{\xi}) = \gamma_{ij} f_j(\xi_l(x_k)), && \text{(A.7.a)} \\ f_j(\boldsymbol{\xi}) &= \gamma_{ij} f_i'(\boldsymbol{x}), && \text{(A.7.b)} \end{aligned}$$

where γ_{ij} are the direction cosines. The vector derivatives are

$$\begin{aligned} \boldsymbol{\nabla} a &= \sum_i \hat{a}_i \frac{1}{h_i}\frac{\partial a}{\partial x_i}, && \text{(A.8.a)} \\ \boldsymbol{\nabla}\cdot\boldsymbol{b} &= \frac{1}{h_1 h_2 h_3}\sum_i \frac{\partial}{\partial x_i}\left(\frac{h_1 h_2 h_3}{h_i} b_i\right), && \text{(A.8.b)} \\ \boldsymbol{\nabla}\times\boldsymbol{b} &= \frac{1}{h_1 h_2 h_3}\sum_{i,j,k} \epsilon_{ijk}\, \hat{a}_i h_i \,\frac{\partial}{\partial x_j}(h_k b_k), && \text{(A.8.c)} \\ \nabla^2 a &= \frac{1}{h_1 h_2 h_3}\sum_i \frac{\partial}{\partial x_i}\left(\frac{h_1 h_2 h_3}{h_i^2}\frac{\partial a}{\partial x_i}\right). && \text{(A.8.d)} \end{aligned}$$

A.2 Cylindrical Coordinates

A.2.1 Using Generalized Coordinate Transformations

To derive the coordinate transformation between cartesian and cylindrical cordinates, with

$$\boldsymbol{r} = \boldsymbol{r}(r,\theta,Z) = \hat{e}_i r_i, \qquad \text{(A.9)}$$

start with the direction cosines matrix,

$$\gamma_{ij} = \begin{pmatrix} \sin\theta & -\cos\theta & 0 \\ \cos\theta & \sin\theta & 0 \\ 0 & 0 & 1 \end{pmatrix}. \qquad \text{(A.10)}$$

The coordinate transformation equations are

$$\begin{aligned} \xi &= r\cos\theta \\ \eta &= r\sin\theta \ , \\ \zeta &= Z \end{aligned} \qquad \begin{aligned} r &= (\xi^2+\eta^2)^{1/2} \\ \theta &= \tan^{-1}\left(\frac{\eta}{\xi}\right) \ . \\ Z &= \zeta \end{aligned} \qquad \text{(A.11)}$$

The scale factors are more easily calculated by using Eq. A.4.a,

$$h_i^2 = \sum_j \left(\frac{\partial \xi_j}{\partial r_i}\right)^2, \tag{A.12}$$

giving

$$\begin{aligned} h_r = h_Z &= 1, && \text{(A.13.a)} \\ h_\theta &= r. && \text{(A.13.b)} \end{aligned}$$

The differential length and volume are

$$\begin{aligned} ds^2 &= dr^2 + r^2 d\theta^2 + dZ^2, && \text{(A.14.a)} \\ dV &= r\ dr\ d\theta\ dZ. && \text{(A.14.b)} \end{aligned}$$

The derivatives of the unit vectors have two non-zero terms,

$$\begin{aligned} \frac{\partial \hat{\boldsymbol{\theta}}}{\partial \theta} &= \frac{\hat{\boldsymbol{\theta}}}{r}\frac{\partial r}{\partial \theta} - \frac{\hat{\boldsymbol{r}}}{1}\frac{\partial r}{\partial r} = -\hat{\boldsymbol{r}}, && \text{(A.15.a)} \\ \frac{\partial \hat{\boldsymbol{r}}}{\partial \theta} &= \frac{\hat{\boldsymbol{\theta}}}{1}\frac{\partial r}{\partial r} = -\hat{\boldsymbol{\theta}}. && \text{(A.15.b)} \end{aligned}$$

Finally, the vector derivatives are

$$\begin{aligned} \boldsymbol{\nabla} a &= \left(\hat{\boldsymbol{r}}\frac{\partial}{\partial r} + \hat{\boldsymbol{\theta}}\frac{1}{r}\frac{\partial}{\partial \theta} + \hat{\boldsymbol{Z}}\frac{\partial}{\partial Z}\right) a, && \text{(A.16.a)} \\ \boldsymbol{\nabla}\cdot\boldsymbol{b} &= \frac{1}{r}\frac{\partial (r b_r)}{\partial r} + \frac{1}{r}\frac{\partial b_\theta}{\partial \theta} + \frac{\partial b_Z}{\partial Z}, && \text{(A.16.b)} \\ \boldsymbol{\nabla}\times\boldsymbol{b} &= \hat{\boldsymbol{r}}\left(\frac{1}{r}\frac{\partial b_Z}{\partial \theta} - \frac{\partial b_\theta}{\partial Z}\right) + \hat{\boldsymbol{\theta}}\left(\frac{\partial b_r}{\partial Z} - \frac{\partial b_Z}{\partial r}\right) + \hat{\boldsymbol{Z}}\frac{1}{r}\left(\frac{\partial (r b_\theta)}{\partial r} - \frac{\partial b_r}{\partial \theta}\right), && \text{(A.16.c)} \\ \nabla^2 a &= \left[\frac{1}{r}\frac{\partial}{\partial r}\left(r\frac{\partial}{\partial r}\right) + \frac{1}{r^2}\frac{\partial^2}{\partial \theta^2} + \frac{\partial^2}{\partial Z^2}\right] a. && \text{(A.16.d)} \end{aligned}$$

A.2.2 Using Directional Derivatives

Using directional derivatives, the vector derivatives of Eq. A.16 can be derived. While this is simpler than using the generalized coordinate form, the results are the same. The advantage of developing this method, however, is seen when deriving more complicated terms, such as the advection term which involves the gradient of a vector.

The vector derivatives can be calculated by starting with the derivatives of the unit vectors, which can be shown graphically (see Fig. A-1) and the definition of the del operator,

$$\begin{aligned} \frac{\partial \hat{\boldsymbol{r}}}{\partial \theta} &= \hat{\boldsymbol{\theta}}, && \text{(A.17.a)} \\ \frac{\partial \hat{\boldsymbol{\theta}}}{\partial \theta} &= -\hat{\boldsymbol{r}}, && \text{(A.17.b)} \\ \boldsymbol{\nabla} &\equiv \hat{\boldsymbol{r}}\frac{\partial}{\partial r} + \hat{\boldsymbol{\theta}}\frac{1}{r}\frac{\partial}{\partial \theta} + \hat{\boldsymbol{Z}}\frac{\partial}{\partial Z}. && \text{(A.17.c)} \end{aligned}$$

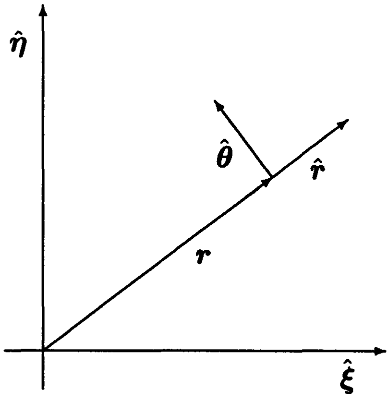

Figure A-1: Annular and cylindrical coordinates unit vectors

In addition, the unit vectors are all ortho-normal, so

$$\hat{e}_i\cdot\hat{e}_j = \delta_{ij}, \tag{A.18.a}$$

$$\hat{e}_i\times\hat{e}_j = \epsilon_{ijk}\,\hat{e}_k. \tag{A.18.b}$$

Then, with the scalar a and the vector $\boldsymbol{b}$,

$$\boldsymbol{b} = \hat{\boldsymbol{r}}b_r + \hat{\boldsymbol{\theta}}b_\theta + \hat{\boldsymbol{Z}}b_Z. \tag{A.19}$$

The vector derivatives will be the same as in Eq. A.16, but the derivations will be different (except for the gradient of a scalar, which is the same). The divergence has the term

$$\left(\hat{\boldsymbol{\theta}}\frac{1}{r}\frac{\partial}{\partial\theta}\right)\cdot(\hat{\boldsymbol{r}}b_r) = \hat{\boldsymbol{\theta}}\cdot\hat{\boldsymbol{\theta}}\frac{1}{r}b_r = \frac{1}{r}b_r, \tag{A.20}$$

so

$$\boldsymbol{\nabla}\cdot\boldsymbol{b} = \frac{\partial b_r}{\partial r} + \frac{1}{r}b_r + \frac{1}{r}\frac{\partial b_\theta}{\partial\theta} + \frac{\partial b_Z}{\partial Z}. \tag{A.21}$$

The curl has the term

$$\hat{\boldsymbol{\theta}}\frac{1}{r}\frac{\partial}{\partial\theta}\times(\hat{\boldsymbol{\theta}}b_\theta) = \hat{\boldsymbol{\theta}}\times(-\hat{\boldsymbol{r}})\frac{1}{r}b_\theta = \hat{\boldsymbol{Z}}\frac{1}{r}b_\theta, \tag{A.22}$$

so the Z-component of the curl is

$$\hat{\boldsymbol{Z}}\cdot(\boldsymbol{\nabla}\times\boldsymbol{b}) = \frac{\partial b_\theta}{\partial r} - \frac{1}{r}\frac{\partial b_r}{\partial\theta} + \frac{1}{r}b_\theta. \tag{A.23}$$

The Laplacian operator is derived by writing it out as the divergence of the gradient,

$$\nabla^2 \equiv \boldsymbol{\nabla}\cdot\boldsymbol{\nabla} = \frac{\partial}{\partial r}\left(\frac{\partial}{\partial r}\right) + \frac{1}{r}\frac{\partial}{\partial r} + \frac{1}{r}\frac{\partial}{\partial\theta}\left(\frac{1}{r}\frac{\partial}{\partial\theta}\right) + \frac{\partial}{\partial Z}\left(\frac{\partial}{\partial Z}\right) \tag{A.24.a}$$

$$= \frac{\partial^2}{\partial r^2} + \frac{1}{r}\frac{\partial}{\partial r} + \frac{1}{r^2}\frac{\partial^2}{\partial\theta^2} + \frac{\partial^2}{\partial Z^2}. \tag{A.24.b}$$

Finally, the advection term is $(\boldsymbol{v}\cdot\boldsymbol{\nabla})\boldsymbol{v}$, with the extra terms from the expression

$$(\hat{\boldsymbol{\theta}}v_\theta)\cdot\left(\hat{\boldsymbol{\theta}}\frac{1}{r}\frac{\partial}{\partial\theta}\right)(\hat{\boldsymbol{r}}v_r + \hat{\boldsymbol{\theta}}v_\theta + \hat{\boldsymbol{Z}}v_Z), \tag{A.25}$$

where the dot operation accounts for the left two $\hat{\boldsymbol{\theta}}$ unit vectors. The unit vectors in the last terms will give the actual directions of the advection terms,

$$v_\theta \frac{1}{r}\left(\hat{\boldsymbol{r}}\frac{\partial v_r}{\partial \theta} + \hat{\boldsymbol{\theta}} v_r + \hat{\boldsymbol{\theta}}\frac{\partial v_\theta}{\partial \theta} - \hat{\boldsymbol{r}} v_\theta + \hat{\boldsymbol{Z}}\frac{\partial v_Z}{\partial \theta}\right). \tag{A.26}$$

Combining this with the $\hat{\boldsymbol{r}}$ and $\hat{\boldsymbol{Z}}$ components of the advection term,

$$v_r\left(\hat{\boldsymbol{r}}\frac{\partial v_r}{\partial r} + \hat{\boldsymbol{\theta}}\frac{\partial v_\theta}{\partial r} + \hat{\boldsymbol{Z}}\frac{\partial v_Z}{\partial r}\right), \tag{A.27}$$

and

$$v_Z\left(\hat{\boldsymbol{r}}\frac{\partial v_r}{\partial Z} + \hat{\boldsymbol{\theta}}\frac{\partial v_\theta}{\partial Z} + \hat{\boldsymbol{Z}}\frac{\partial v_Z}{\partial Z}\right), \tag{A.28}$$

gives

$$\begin{aligned}
(\boldsymbol{v}\cdot\nabla)\boldsymbol{v} &= +\hat{\boldsymbol{r}}\left(v_r\frac{\partial v_r}{\partial r} + \frac{1}{r}v_\theta\frac{\partial v_r}{\partial \theta} + v_Z\frac{\partial v_r}{\partial Z} - \frac{1}{r}v_\theta^2\right) && \text{(A.29.a)}\\
&\quad +\hat{\boldsymbol{\theta}}\left(v_r\frac{\partial v_\theta}{\partial r} + \frac{1}{r}v_\theta\frac{\partial v_\theta}{\partial \theta} + v_Z\frac{\partial v_\theta}{\partial Z} + \frac{1}{r}v_r v_\theta\right) && \text{(A.29.b)}\\
&\quad +\hat{\boldsymbol{Z}}\left(v_r\frac{\partial v_Z}{\partial r} + \frac{1}{r}v_\theta\frac{\partial v_Z}{\partial \theta} + v_Z\frac{\partial v_Z}{\partial Z}\right). && \text{(A.29.c)}
\end{aligned}$$

This same procedure is used to derive the advection term in annular coordinates.

A.2.3 Rotating Coordinate System

It is convenient to transform to a rotating coordinate system, with a constant angular velocity,

$$\boldsymbol{\Omega} = \hat{z}\Omega_c. \tag{A.30}$$

The coordinate transformation from non-rotating (primed) to rotating coordinates (unprimed) is

$$\left(\frac{d}{dt}\right)' = \left(\frac{d}{dt} + \boldsymbol{\Omega}\times\right), \tag{A.31}$$

so

$$\begin{aligned}
\boldsymbol{v}' &= \frac{d}{dt}\boldsymbol{r}'\\
&= \boldsymbol{v} + \boldsymbol{\Omega}\times\boldsymbol{r}, && \text{(A.32.a)}
\end{aligned}$$

and

$$\begin{aligned}
\frac{d\boldsymbol{v}'}{dt} &= \frac{d^2\boldsymbol{r}'}{dt^2}\\
&= \left(\frac{d}{dt} + \boldsymbol{\Omega}\times\right)\left(\frac{d}{dt} + \boldsymbol{\Omega}\times\right)\boldsymbol{r}\\
&= \frac{d^2\boldsymbol{r}}{dt^2} + \boldsymbol{\Omega}\times\frac{d\boldsymbol{r}}{dt} + \frac{d(\boldsymbol{\Omega}\times\boldsymbol{r})}{dt} + \boldsymbol{\Omega}\times(\boldsymbol{\Omega}\times\boldsymbol{r})\\
&= \frac{d\boldsymbol{v}}{dt} + 2\boldsymbol{\Omega}\times\boldsymbol{v} + \boldsymbol{\Omega}\times(\boldsymbol{\Omega}\times\boldsymbol{r}) + \left[\frac{d\boldsymbol{\Omega}}{dt}\times\boldsymbol{r}\right]. && \text{(A.33)}
\end{aligned}$$

The last term is zero with a constantly rotating coordinate system. The centrifugal term can be expressed as a gradient, using

$$\begin{aligned}
\boldsymbol{\nabla}[(\boldsymbol{\Omega} \times \boldsymbol{r}) \cdot (\boldsymbol{\Omega} \times \boldsymbol{r})] &= \partial_i[(\epsilon_{jkl}\Omega_k r_l)(\epsilon_{jmn}\Omega_m r_n)] \\
&= \epsilon_{jkl}\epsilon_{jmn}\Omega_k\Omega_m\partial_i(r_l r_n) \\
&= 2\epsilon_{jkl}\epsilon_{jmn}\Omega_k\Omega_m r_n\delta_{il} \\
&= -2\epsilon_{ikj}\Omega_k\epsilon_{jmn}\Omega_m r_n \\
&= -2\,\boldsymbol{\Omega} \times (\boldsymbol{\Omega} \times \boldsymbol{r}). \qquad \text{(A.34)}
\end{aligned}$$

The transformation for the acceleration is

$$\frac{d\boldsymbol{v}'}{dt} = \frac{d\boldsymbol{v}}{dt} + 2\boldsymbol{\Omega} \times \boldsymbol{v} - \boldsymbol{\nabla}\left(\tfrac{1}{2}|\boldsymbol{\Omega} \times \boldsymbol{r}|^2\right). \qquad \text{(A.35)}$$

Transformations to the rotating system are simplified by using

$$\begin{aligned}
\boldsymbol{\nabla}\cdot(\boldsymbol{\Omega} \times \boldsymbol{r}) &= 0, \qquad \text{(A.36.a)} \\
\nabla^2(\boldsymbol{\Omega} \times \boldsymbol{r}) &= 0. \qquad \text{(A.36.b)}
\end{aligned}$$

The values for the Keplerian disk, first in non-rotating terms, are

$$\begin{aligned}
k_k &\equiv \sqrt{GM_\odot} = 2\pi\,\mathrm{AU}^{3/2}\,\mathrm{yr}^{-2}, \qquad \text{(A.37.a)} \\
v_k &= k_k r^{-1/2}, \qquad \text{(A.37.b)} \\
\Omega_k &= k_k r^{-3/2}, \qquad \text{(A.37.c)} \\
q_k &= \tfrac{1}{2}k_k r^{1/2}, \qquad \text{(A.37.d)} \\
\psi_k &= 2k_k r^{-3/2}, \qquad \text{(A.37.e)} \\
\boldsymbol{g} &= -\hat{\boldsymbol{r}} k_k^2 r^{-2}. \qquad \text{(A.37.f)}
\end{aligned}$$

For the rotating frame,

$$\Omega_c = k_k r_c^{-3/2}, \qquad \text{(A.38)}$$

and the fluid values are

$$\begin{aligned}
\vec{v} &= \hat{\boldsymbol{\theta}} k_k \left[r^{-1/2} - r r_c^{-3/2}\right], \qquad \text{(A.39.a)} \\
\bar{\psi} &= k_k \left[2r^{1/2} - \tfrac{1}{2}r^2 r_c^{-3/2}\right], \qquad \text{(A.39.b)} \\
\bar{q} &= k_k \left[\tfrac{1}{2}r^{-3/2} - 2r_c^{-3/2}\right]. \qquad \text{(A.39.c)}
\end{aligned}$$

A.2.4 Equations of Motion

The equations of motion in cylindrical coordinates can be calculated using the time derivatives of the unit vectors,

$$\begin{aligned}
\frac{d\hat{\boldsymbol{r}}}{dt} &= \frac{d\theta}{dt}\frac{d\hat{\boldsymbol{r}}}{d\theta} = \dot{\theta}\hat{\boldsymbol{\theta}}, \qquad \text{(A.40.a)} \\
\frac{d\hat{\boldsymbol{\theta}}}{dt} &= \frac{d\theta}{dt}\frac{d\hat{\boldsymbol{\theta}}}{d\theta} = -\dot{\theta}\hat{\boldsymbol{r}}. \qquad \text{(A.40.b)}
\end{aligned}$$

Then, starting with the position vector, $\boldsymbol{r}$, the velocity and acceleration are

$$\begin{aligned} \boldsymbol{r} &= r\hat{\boldsymbol{r}}, && \text{(A.41.a)} \\ \dot{\boldsymbol{r}} &= \dot{r}\hat{\boldsymbol{r}} + r\dot{\theta}\hat{\boldsymbol{\theta}}, && \text{(A.41.b)} \\ \ddot{\boldsymbol{r}} &= \hat{\boldsymbol{r}}(\ddot{r} - r\dot{\theta}^2) + \hat{\boldsymbol{\theta}}(r\ddot{\theta} + 2\dot{r}\dot{\theta}). && \text{(A.41.c)} \end{aligned}$$

Defining the radial and angular velocities (u, v), their time derivatives can be calculated as

$$\begin{aligned} u &\equiv \dot{r} \\ v &\equiv r\dot{\theta} \end{aligned}, \qquad \begin{aligned} \dot{u} &= \ddot{r} \\ \dot{v} &= r\ddot{\theta} + \dot{r}\dot{\theta} \end{aligned}. \tag{A.42}$$

The velocity and acceleration vectors are

$$\begin{aligned} \dot{\boldsymbol{r}} &= u\hat{\boldsymbol{r}} + v\hat{\boldsymbol{\theta}}, && \text{(A.43.a)} \\ \ddot{\boldsymbol{r}} &= \hat{\boldsymbol{r}}\left(\dot{u} - \frac{1}{r}v^2\right) + \hat{\boldsymbol{\theta}}\left(\dot{v} + \frac{1}{r}uv\right). && \text{(A.43.b)} \end{aligned}$$

A.3 Annular Coordinates

A.3.1 Description of Annular Coordinates

A system of annular coordinates is developed, based on cylindrical coordinates, but with the radial coordinate proportional to the logarithm of the distance. The proportionality constant specifies the radius of the origin of the coordinate system. The angular coordinate includes a periodicity factor which allows a specified number of coordinate frames in the annulus, each 2π wide. The (x, y) coordinates are related to (r, θ) with two parameters, r_0 and M, and the relations

$$\begin{aligned} x &= -M\theta \\ y &= M\ln\left(\frac{r}{r_0}\right) \end{aligned}, \qquad \begin{aligned} r &= r_0\, e^{y/M} \\ \theta &= -\frac{1}{M}x \end{aligned}. \tag{A.44}$$

There are a number of features which make these coordinates useful. First, quantities which obey a power law in radius become linear in y. Second, the coordinate differentials are both non-dimensional, so the area differential maintains its aspect ratio at different radii. This also gives a higher resolution closer to the center of the disk and a lower resolution further away, which is computationally efficient since most quantities change more at smaller radii. Third, the origin can also be set at various locations without changing the equations or most of the quantities, except for r_0 as a multiplicative factor. This allows the study of regions at different radii to be done easily, i.e. at the Earth's and Jupiter's positions. The radial dependencies can be seen as factors of r_0. Fourth, the region can be restricted to a small portion of the annulus, which allows the study of properties at different length scales, again by only changing one parameter, M. With large M, the curvature of the grid is reduced, leading to a cartesian coordinate limit which will be derived below. Fifth, the Laplacian in annular coordinates has only second derivative terms, in contrast to the cylindrical coordinate form, simplifying the calculation of the inverse Laplacian, which is used to calculate the streamfunction from the vorticity.

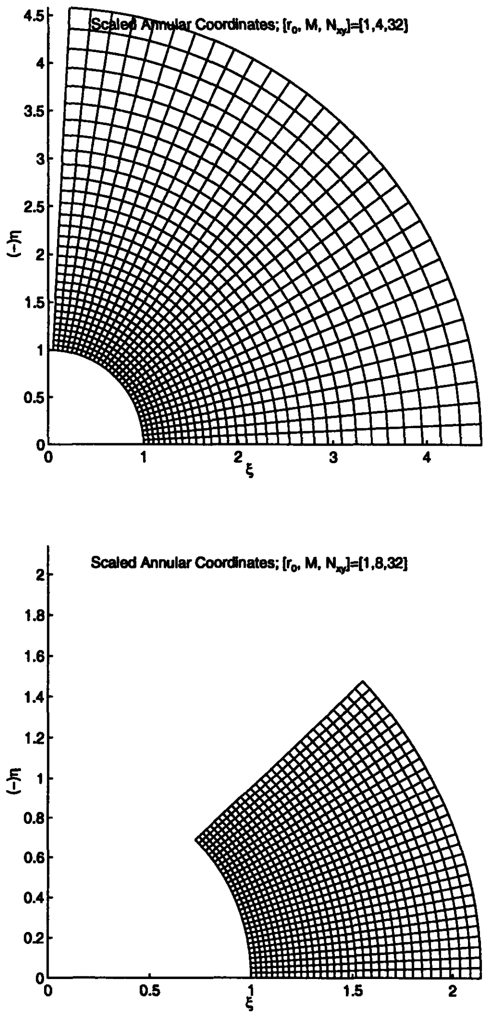

Figure A-2: Annular ccordinate grid, with $r_0 = 1.0$, $x = [0, 2\pi]$, $y = [0, 2\pi]$; (a) $M = 4$, (b) $M = 8$

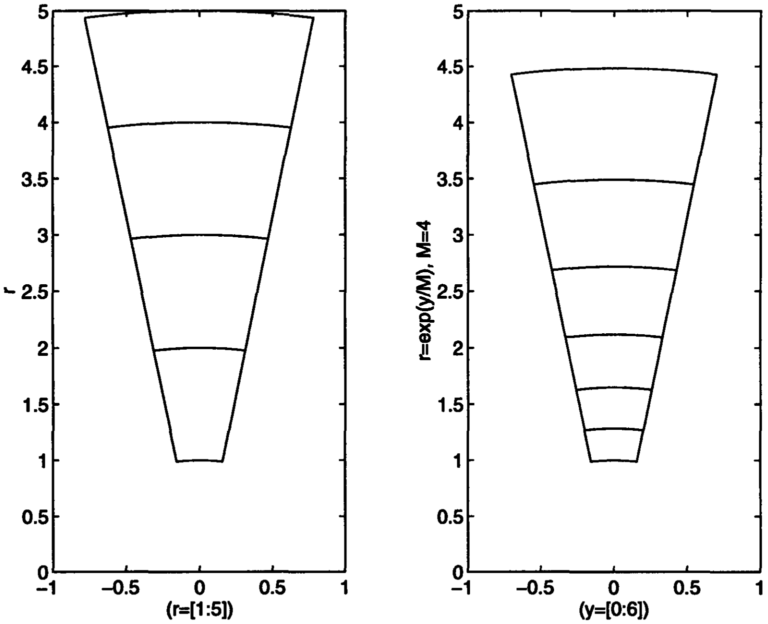

Figure A-3: Area differentials in cylindrical and annular coordinates at different radii

It is useful to define the two quantities,

$$Y \equiv e^{y/M}, \tag{A.45.a}$$

$$R \equiv \frac{r_0}{M}, \tag{A.45.b}$$

giving

$$r = MRY, \tag{A.46.a}$$

$$\frac{\partial Y}{\partial y} = \frac{1}{M}Y, \tag{A.46.b}$$

$$\frac{dY}{dt} = \frac{1}{M}Y\dot{y}. \tag{A.46.c}$$

The unit vectors are related to the cylindrical coordinate unit vectors by

$$\hat{\boldsymbol{x}} = -\hat{\boldsymbol{\theta}}, \tag{A.47.a}$$

$$\hat{\boldsymbol{y}} = \hat{\boldsymbol{r}}. \tag{A.47.b}$$

The vector derivatives can be derived using either generalized curvilinear coordinate transformations or the directional derivatives, both described below.

A.3.2 Using Generalized Coordinate Transformations

The annular coordinates, $\boldsymbol{x} = \boldsymbol{x}(x, y, z)$, are related to the cartesian coordinates, $\boldsymbol{\xi}$, and the cylindrical coordinates, $\boldsymbol{r}$, by the set of coordinate transformation equations,

$$r = r_0 e^{y/M}, \tag{A.48.a}$$

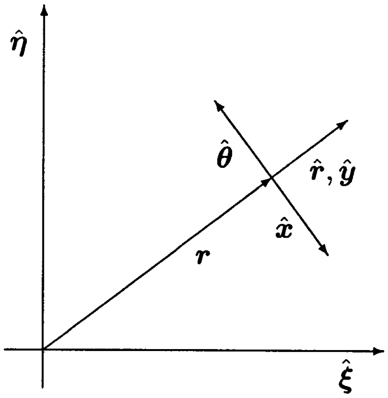

Figure A-4: Annular and cylindrical coordinates unit vectors

$$\theta = -\frac{1}{M}x, \tag{A.48.b}$$

$$Z = z; \tag{A.48.c}$$

$$y = \frac{1}{M}\ln\left(\frac{r}{r_0}\right) = \tfrac{1}{2}M\ln\left(\frac{\xi^2+\eta^2}{r_0^2}\right), \tag{A.49.a}$$

$$x = -M\theta = -M\tan^{-1}\left(\frac{\eta}{\xi}\right), \tag{A.49.b}$$

$$z = Z = \zeta; \tag{A.49.c}$$

and

$$\xi = +r_0 e^{y/M}\cos\left(\frac{1}{M}x\right), \tag{A.50.a}$$

$$\eta = -r_0 e^{y/M}\sin\left(\frac{1}{M}x\right), \tag{A.50.b}$$

$$\zeta = z. \tag{A.50.c}$$

The annular coordinate unit vectors, $\hat{a} = (\hat{\boldsymbol{x}}, \hat{\boldsymbol{y}}, \hat{\boldsymbol{z}})$, are related to the cylindrical coordinate unit vectors, $\hat{e} = (\hat{\boldsymbol{r}}, \hat{\boldsymbol{\theta}}, \hat{\boldsymbol{Z}})$, by

$$\hat{\boldsymbol{x}} = -\hat{\boldsymbol{\theta}}, \tag{A.51.a}$$

$$\hat{\boldsymbol{y}} = \hat{\boldsymbol{r}}, \tag{A.51.b}$$

$$\hat{\boldsymbol{z}} = \hat{\boldsymbol{Z}}, \tag{A.51.c}$$

so the direction cosine matrix is

$$\gamma_{ij} = \begin{pmatrix} \sin\theta & \cos\theta & 0 \\ -\cos\theta & \sin\theta & 0 \\ 0 & 0 & 1 \end{pmatrix}, \tag{A.52}$$

as shown in Fig. A-5.

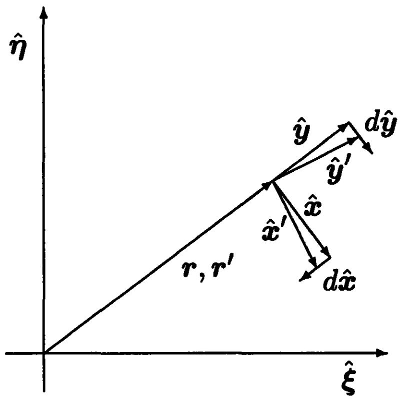

Figure A-5: Annular coordinates unit vectors derivatives

The scale factors are more easily calculated by using Eq. A.4.a,

$$h_i^2 = \sum_j \left(\frac{\partial \xi_j}{\partial x_i}\right)^2, \tag{A.53}$$

giving

$$\begin{aligned} h_x = h_y &= \frac{r}{M} = RY, && \text{(A.54.a)} \\ h_z &= 1. && \text{(A.54.b)} \end{aligned}$$

The differential length and volume are

$$\begin{aligned} ds^2 &= (RY)^2 dx^2 + (RY)^2 dy^2 + dz^2, && \text{(A.55.a)} \\ dV &= (RY)^2\, dx\, dy\, dz. && \text{(A.55.b)} \end{aligned}$$

The derivatives of the unit vectors have two non-zero terms,

$$\begin{aligned} \frac{\partial \hat{x}}{\partial x} &= -\frac{1}{M}\hat{y}, && \text{(A.56.a)} \\ \frac{\partial \hat{y}}{\partial x} &= \frac{1}{M}\hat{x}. && \text{(A.56.b)} \end{aligned}$$

The vector derivatives are

$$\begin{aligned} \nabla a &= \left[\left(\frac{M}{r}\right)\left(\hat{x}\frac{\partial}{\partial x} + \hat{y}\frac{\partial}{\partial y}\right) + \hat{z}\frac{\partial}{\partial z}\right] a, && \text{(A.57.a)} \\ \nabla\cdot b &= \left(\frac{M}{r}\right)\left(\frac{\partial b_x}{\partial x} + \frac{\partial b_y}{\partial y} + \frac{1}{M}b_y\right) + \frac{\partial b_z}{\partial z}, && \text{(A.57.b)} \\ \nabla\times b &= \hat{x}\left[\frac{M}{r}\frac{\partial b_z}{\partial y} - \frac{\partial b_y}{\partial z}\right] + \hat{y}\left[\frac{\partial b_x}{\partial z} - \frac{M}{r}\frac{\partial b_z}{\partial x}\right] + \hat{z}\frac{M}{r}\left[\frac{\partial b_y}{\partial x} - \frac{\partial b_x}{\partial y} - \frac{1}{M}b_x\right], && \text{(A.57.c)} \\ \nabla^2 a &= \left[\left(\frac{M}{r}\right)^2\left(\frac{\partial^2}{\partial x^2} + \frac{\partial^2}{\partial y^2}\right) + \frac{\partial^2}{\partial z^2}\right] a. && \text{(A.57.d)} \end{aligned}$$

A.3.3 Using Directional Derivatives

Using directional derivatives, the x-derivatives of the unit vectors and the y-derivative of r will all add terms to the various expressions. The unit vector derivatives, r derivative, and del operator are

$$\begin{aligned}
\frac{\partial \hat{\boldsymbol{x}}}{\partial x} &= -\frac{1}{M}\hat{\boldsymbol{y}}, && \text{(A.58.a)}\\
\frac{\partial \hat{\boldsymbol{y}}}{\partial x} &= +\frac{1}{M}\hat{\boldsymbol{x}}, && \text{(A.58.b)}\\
\frac{\partial r}{\partial y} &= \frac{1}{M}r, && \text{(A.58.c)}\\
\boldsymbol{\nabla} &= \hat{\boldsymbol{x}}\frac{M}{r}\frac{\partial}{\partial x} + \hat{\boldsymbol{y}}\frac{M}{r}\frac{\partial}{\partial y} + \hat{\boldsymbol{z}}\frac{\partial}{\partial z}. && \text{(A.58.d)}
\end{aligned}$$

The vector derivatives are given in the previous section.

A.3.4 Equations of Motion

To get the velocity and acceleration vectors, the time derivatives of Y, $\hat{\boldsymbol{x}}$, and $\hat{\boldsymbol{y}}$ are needed,

$$\begin{aligned}
\frac{dY}{dt} &= \frac{1}{M}Y\dot{y}, && \text{(A.59.a)}\\
\frac{d\hat{\boldsymbol{x}}}{dt} &= -\frac{1}{M}\dot{x}\hat{\boldsymbol{y}}, && \text{(A.59.b)}\\
\frac{d\hat{\boldsymbol{y}}}{dt} &= \frac{1}{M}\dot{x}\hat{\boldsymbol{x}}. && \text{(A.59.c)}
\end{aligned}$$

The velocity and acceleration vectors are

$$\begin{aligned}
\dot{\boldsymbol{r}} &= RY(\dot{x}\hat{\boldsymbol{x}} + \dot{y}\hat{\boldsymbol{y}}), && \text{(A.60.a)}\\
\ddot{\boldsymbol{r}} &= RY\left[\hat{\boldsymbol{x}}\left(\ddot{x} + \frac{2}{M}\dot{x}\dot{y}\right) + \hat{\boldsymbol{y}}\left(\ddot{y} + \frac{1}{M}\dot{y}^2 - \frac{1}{M}\dot{x}^2\right)\right]. && \text{(A.60.b)}
\end{aligned}$$

Defining the velocity components, (u, v), and taking the time derivatives, gives

$$\begin{array}{rcl} u &\equiv& RY\dot{x} \\ v &\equiv& RY\dot{y} \end{array}, \qquad \begin{array}{rcl} \dot{u} &=& RY(\ddot{x} + \dot{x}\dot{y}/M) \\ \dot{v} &=& RY(\ddot{y} + \dot{y}^2/M) \end{array}. \qquad \text{(A.61)}$$

These velocity components are rotated from the definitions for cylindrical coordinates. Here, u is the tangential, clockwise velocity and v is the radial velocity. In the cylindrical coordinates, u is the radial velocity and v is the clockwise tangential velocity. The velocity and acceleration vectors are then

$$\begin{aligned}
\dot{\boldsymbol{r}} &= u\hat{\boldsymbol{x}} + v\hat{\boldsymbol{y}}, && \text{(A.62.a)}\\
\ddot{\boldsymbol{r}} &= \hat{\boldsymbol{x}}\left(\dot{u} + \frac{1}{r}uv\right) + \hat{\boldsymbol{y}}\left(\dot{v} - \frac{1}{r}u^2\right). && \text{(A.62.b)}
\end{aligned}$$

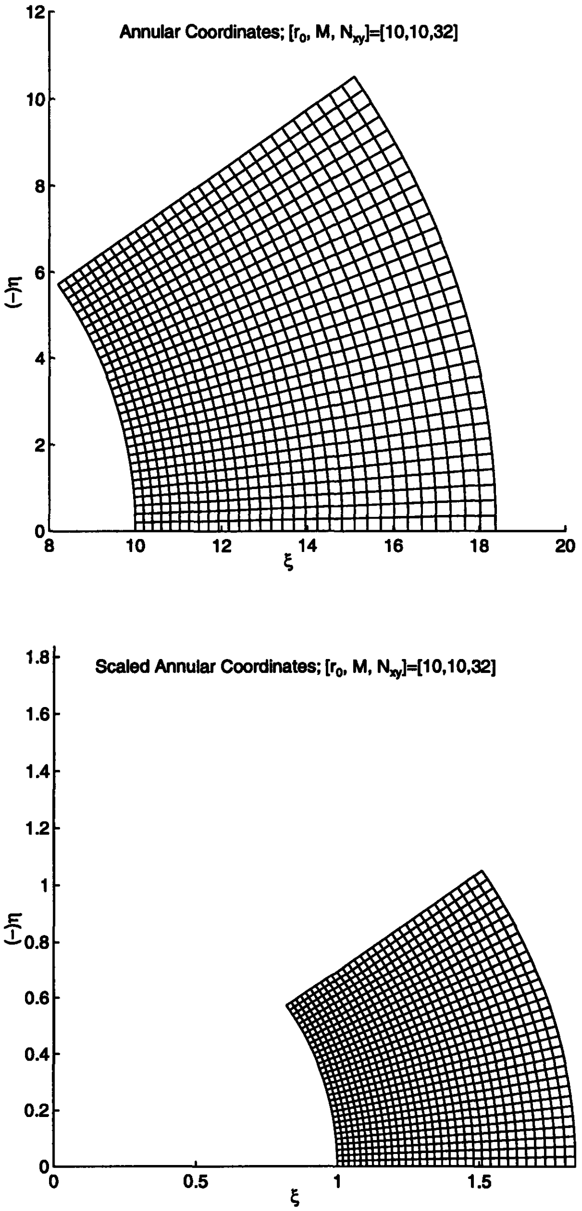

Figure A-6: Annular grid for large M ($M = 10$)

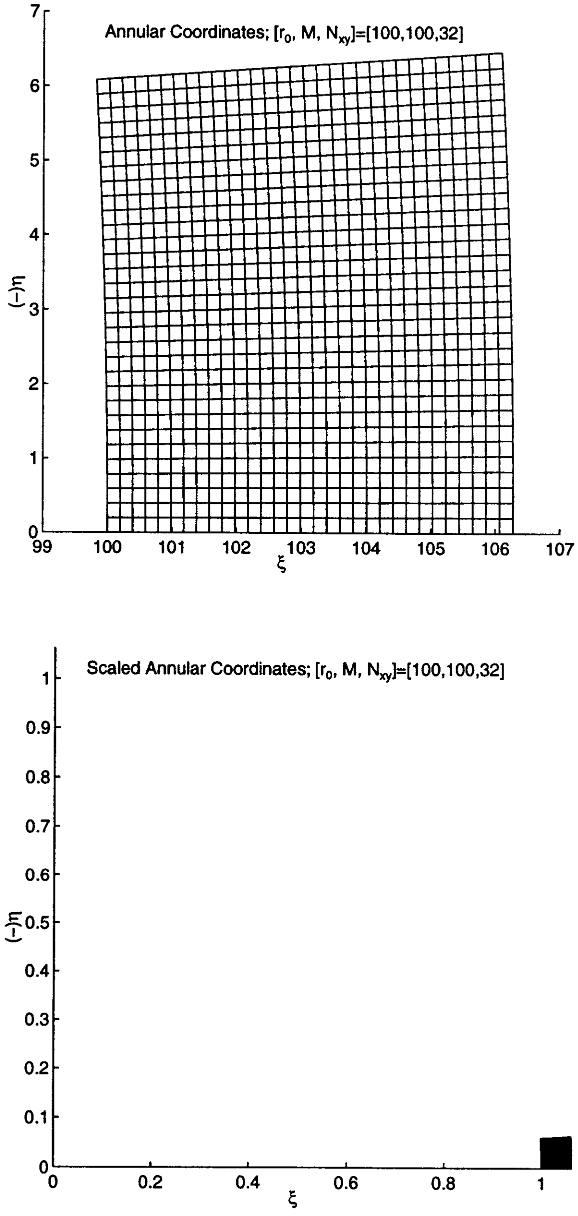

Figure A-7: Annular grid for large M ($M = 100$)

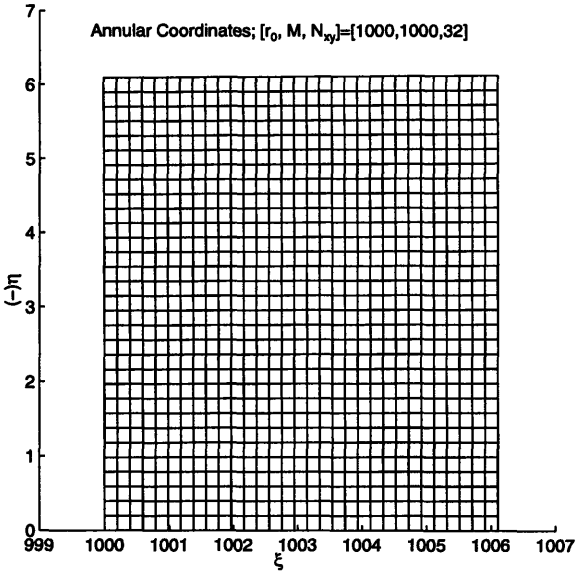

Figure A-8: Annular grid for large M ($M = 1000$)

A.3.5 Cartesian Coordinate Limit

In the limit where M and r_0 both get large and equal, so $R = 1$, the curvature of the annular coordinates is eliminated, leaving a set of approximately Cartesian coordinates. Figures A-6–A-7 show the annular grid for large M, showing the approach to a Cartesian grid. This is useful because the grid is still in a rotating frame, and this approach allows the re-derivation of the annular fluid equations in the pseudo-cartesian system. In this limit, first use

$$Y = e^{y/M} \approx 1 + \frac{y}{M}, \tag{A.63}$$

and then

$$\frac{1}{M} \to 0. \tag{A.64}$$

The scale factors become

$$h_x = h_y = RY \approx \left(1 + \frac{y}{M}\right) \sim 1, \tag{A.65}$$

so the scale factors approach unity, as is the case with the Cartesian coordinate scale factors. Using

$$r = MRY \approx r_0\left(1 + \frac{y}{M}\right) \sim r_0 + y, \tag{A.66.a}$$

$$\cos\left(\frac{1}{M}x\right) \approx 1 - \left(\frac{1}{M}x\right)^2 \sim 1, \tag{A.66.b}$$

$$\sin\left(\frac{1}{M}x\right) \approx \frac{1}{M}x \sim 0, \tag{A.66.c}$$

the coordinate transformation equations, Eq. A.50, become

$$\begin{aligned} \xi &\sim r_0 + y, && \text{(A.67.a)} \\ \eta &\approx -(r_0 + y)\left(\frac{1}{M}x\right) \sim -x. && \text{(A.67.b)} \end{aligned}$$

The direction cosine matrix becomes

$$\gamma_{ij} = \begin{pmatrix} 0 & 1 & 0 \\ -1 & 0 & 0 \\ 0 & 0 & 1 \end{pmatrix}, \tag{A.68}$$

so the unit vectors are the same as the Cartesian unit vectors, except they are rotated,

$$\begin{aligned} \hat{\epsilon}_\xi &= \hat{\boldsymbol{y}}, && \text{(A.69.a)} \\ \hat{\epsilon}_\eta &= -\hat{\boldsymbol{x}}. && \text{(A.69.b)} \end{aligned}$$

The del operator is

$$\boldsymbol{\nabla} = \hat{\boldsymbol{x}}\frac{\partial}{\partial x} + \hat{\boldsymbol{y}}\frac{\partial}{\partial y} + \hat{\boldsymbol{z}}\frac{\partial}{\partial z}, \tag{A.70}$$

so the vector derivatives are simply the Cartesian system expressions.

A.4 Elliptical Coordinates

The ellipse, E, is defined as

$$E \equiv \left\{(x,y) : \frac{x^2}{a^2} + \frac{y^2}{b^2} = 1\right\}. \tag{A.71}$$

Defining the aspect ratio,

$$\lambda \equiv \frac{b}{a}, \tag{A.72}$$

the ellipse is

$$E = \left\{(x,y) : \lambda x^2 + \frac{1}{\lambda}y^2 = ab\right\}. \tag{A.73}$$

With the length scale,

$$s = \sqrt{ab}, \tag{A.74}$$

the focus is

$$c = \sqrt{a^2 - b^2}, \tag{A.75}$$

and

$$\begin{aligned} a &= s\frac{1}{\sqrt{\lambda}}, && \text{(A.76.a)} \\ b &= s\sqrt{\lambda}, && \text{(A.76.b)} \\ c &= s\sqrt{\frac{1-\lambda^2}{\lambda}}. && \text{(A.76.c)} \end{aligned}$$

Elliptical coordinates, (μ, ϕ), are related to cartesian coordinates, (x, y), by

$$\begin{aligned} x &= c \cosh\mu \, \cos\phi, && \text{(A.77.a)} \\ y &= c \sinh\mu \, \sin\phi. && \text{(A.77.b)} \end{aligned}$$

The ellipse is

$$E = \{(\mu, \phi) : \mu = \mu_0\}. \tag{A.78}$$

This gives the relations

$$\begin{aligned} a &= c \cosh\mu_0, && \text{(A.79.a)} \\ b &= c \sinh\mu_0, && \text{(A.79.b)} \end{aligned}$$

and

$$\begin{aligned} \tanh\mu_0 &= \frac{b}{a} = \lambda, && \text{(A.80.a)} \\ \sinh\mu_0 &= \frac{b}{c} = \frac{\lambda}{\sqrt{1-\lambda^2}}, && \text{(A.80.b)} \\ \cosh\mu_0 &= \frac{a}{c} = \frac{1}{\sqrt{1-\lambda^2}}. && \text{(A.80.c)} \end{aligned}$$

The elliptical coordinate grid is plotted in Figs. A-9 and A-10.

The derivatives are

$$\begin{aligned} \frac{\partial x}{\partial \mu} &= \frac{\partial y}{\partial \phi} = c \sinh\mu \, \cos\phi = d_1, && \text{(A.81.a)} \\ -\frac{\partial x}{\partial \phi} &= \frac{\partial y}{\partial \mu} = c \cosh\mu \, \sin\phi = d_2. && \text{(A.81.b)} \end{aligned}$$

The cartesian derivatives for a function f are

$$\begin{aligned} \frac{df}{dx} &= +\frac{\partial(f, y)}{\partial(x, y)}, && \text{(A.82.a)} \\ \frac{df}{dy} &= -\frac{\partial(f, x)}{\partial(x, y)}. && \text{(A.82.b)} \end{aligned}$$

To get the cartesian derivatives of a function in elliptical coordinates, use the Jacobian determinant,

$$\frac{\partial(x, y)}{\partial(\mu, \phi)} \equiv d_1^2 + d_2^2, \tag{A.83}$$

and

$$\begin{aligned} \frac{df}{dx} &= +\frac{\partial(f, y)}{\partial(\mu, \phi)} \Big/ \frac{\partial(x, y)}{\partial(\mu, \phi)} = \frac{f_\mu d_1 - f_\phi d_2}{d_1^2 + d_2^2}, && \text{(A.84.a)} \\ \frac{df}{dy} &= -\frac{\partial(f, x)}{\partial(\mu, \phi)} \Big/ \frac{\partial(x, y)}{\partial(\mu, \phi)} = \frac{f_\mu d_2 + f_\phi d_1}{d_1^2 + d_2^2}. && \text{(A.84.b)} \end{aligned}$$

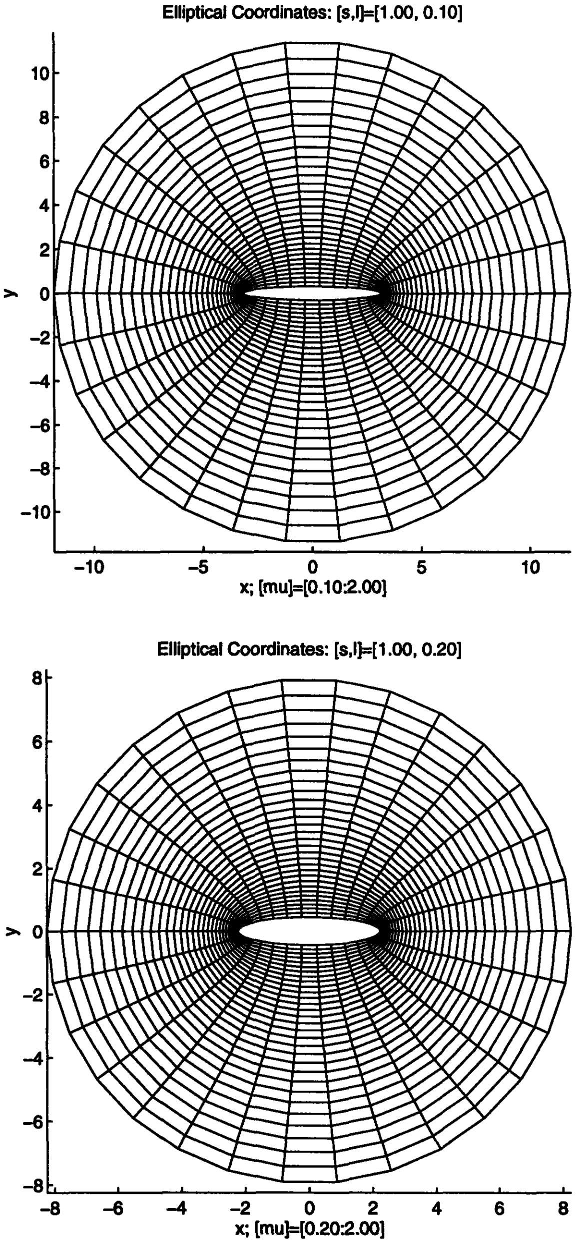

Figure A-9: Elliptical Coordinates, $[s, \lambda] = [1.0, 0.1], [1.0, 0.20]$

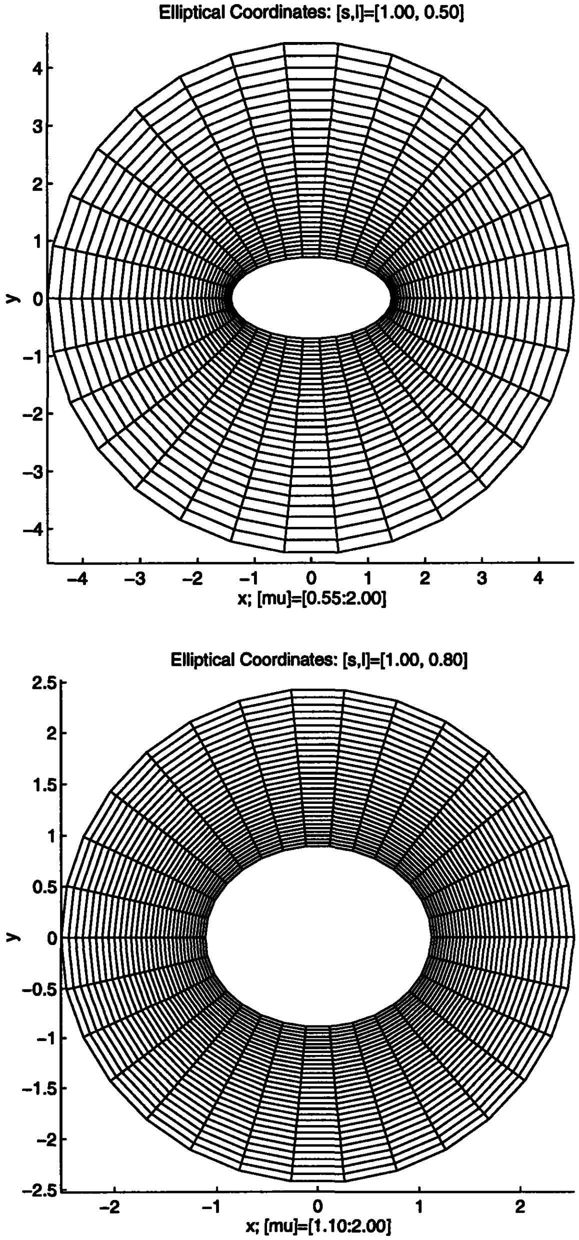

Figure A-10: Elliptical Coordinates, $[s, \lambda] = [1.0, 0.5], [1.0, 0.8]$

A.5 Vector Formulas

With the position vector, $\boldsymbol{r}$, the vector derivatives are

$$\begin{aligned} \boldsymbol{\nabla} \boldsymbol{r} &= \mathbf{I}, & \text{(A.85.a)} \\ \boldsymbol{\nabla} \cdot \boldsymbol{r} &= 3, & \text{(A.85.b)} \\ \boldsymbol{\nabla} \times \boldsymbol{r} &= 0, & \text{(A.85.c)} \\ \nabla^2 \boldsymbol{r} = \boldsymbol{\nabla} \cdot \boldsymbol{\nabla} \boldsymbol{r} &= 0. & \text{(A.85.d)} \end{aligned}$$

Two useful vector identities are

$$\frac{1}{2} \boldsymbol{\nabla} (\boldsymbol{a} \cdot \boldsymbol{a}) = (\boldsymbol{a} \cdot \boldsymbol{\nabla}) \boldsymbol{a} + \boldsymbol{a} \times (\boldsymbol{\nabla} \times \boldsymbol{a}), \tag{A.86}$$

and

$$\boldsymbol{\nabla} \cdot (\boldsymbol{a} \times \boldsymbol{b}) = \boldsymbol{b} \cdot (\boldsymbol{\nabla} \times \boldsymbol{a}) - \boldsymbol{a} \cdot (\boldsymbol{\nabla} \times \boldsymbol{b}). \tag{A.87}$$